Analytic error analysis of orbital configurations for gravity research missions

Master's thesis

Gabriel Valles Valverde

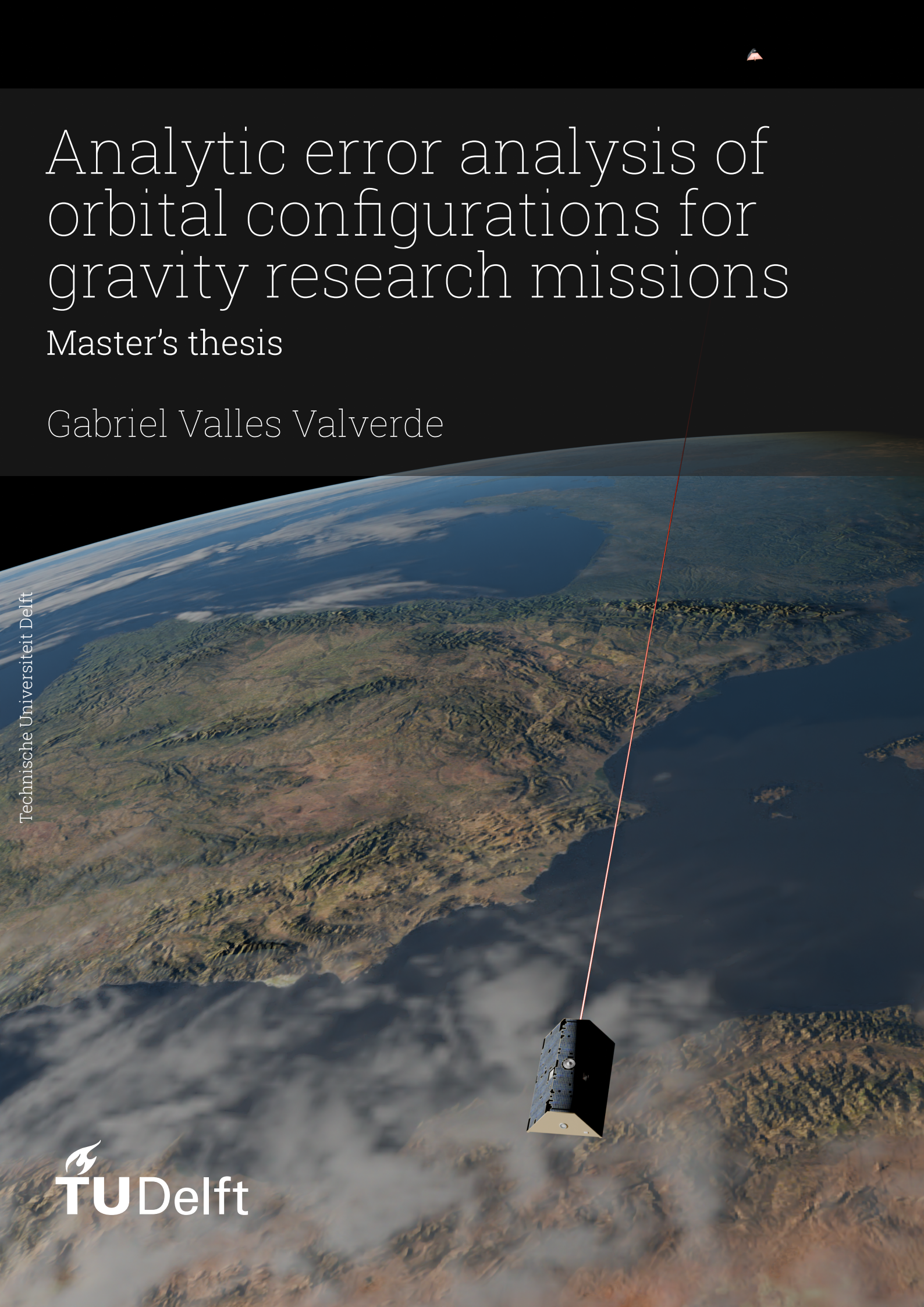

Technische Universiteit Delft

TU Delft

Analytic error analysis of orbital configurations for gravity research missions

Master's thesis

by

Gabriel Valles Valverde

to obtain the degree of Master of Science
at the Delft University of Technology,
to be defended publicly on Tuesday, July 15, 2024, at 09:00 AM.

Student number:	6047289	
Project duration:	December 5, 2024 – July 1, 2025	
Thesis committee:	Dr. ir. E.J.O. Schrama,	TU Delft, supervisor
	Dr. Bart Root,	TU Delft, chair
	Dr. Joao De Teixeira da Encarnação,	TU Delft

Cover: Artist's impression of GRACE-FO laser ranging link. Satellite 3D model from Christopher M. Garcia (NASA 3D Resources).

An electronic version of this thesis is available at http://repository.tudelft.nl/.

TU Delft

Preface

Almost two years ago, I embarked on a new challenge as part of the master's studies in Aerospace Engineering at TU Delft. This journey has been intense, but extremely rewarding. I have been able to deepen my knowledge of the space field and further develop my passion for this exciting discipline. This thesis marks the culmination of my master's studies at TU Delft.

I would like to sincerely thank my supervisor, Dr. Ernst Schrama, for giving me the opportunity to delve into the world of gravity fields. I truly appreciate our insightful discussions and your valuable guidance throughout the thesis. I also want to thank everyone else at the Space Engineering department who has helped me with this project.

Many thanks to my colleagues and friends from the master's program, especially Federico, Varun, and Jasper, for the challenges and good moments we have shared.

To conclude, I am extremely thankful to my family, my parents, and my sister. Your unconditional support has encouraged me to work thoroughly and overcome all the difficulties in my studies.

Gabriel Valles Valverde
Delft, July 2025

Abstract

The GRACE/GRACE-FO mission has provided Earth's monthly gravity field data for more than 20 years. It has been a major success and has enabled significant contributions across multiple domains (e.g. water management, cryosphere monitoring, solid Earth sciences...). Nonetheless, short-periodic effects are undersampled, and the data is noisy at high spatial frequencies, leading to north-south stripes in gravity field functionals. Future gravity research missions aim at improving both spatial and temporal resolution to fulfil increasingly demanding science and societal needs. In this work, an analytical spectral methodology is employed to study gravity field recovery capabilities of different configurations: GRACE-like, Bender configuration and multi-satellite pairs configurations. The analytical model underestimates GRACE operational performance by almost one order of magnitude. Application of NGGM performance to a Bender configuration shows the observability of the atmospheric and ocean non-tidal signal with a resolution of 200 km. Moreover, the theoretical feasibility of daily and 3-hour solutions with 3 and 48 satellite pairs, respectively, is demonstrated, with a resolution of roughly 1000 km, assuming CubeSat performance. In this way, future missions might not only improve spatio-temporal resolution but also mitigate other errors sources.

Gabriel Valles Valverde
Delft, July, 2025

Contents

Acronyms

AMOC	Atlantic Meridional Overturning Circulation
AOD1B	Atmosphere and Ocean Dealiasing Level-1B product
ASD	Amplitude Spectral Density
CHAMP	Challenging Minisatellite Payload
DDK	Decorrelation and Denoising Kernel
DFAOCS	Drag-Free Attitude and Orbit Control System
ECEF	Earth-Centered, Earth-Fixed
ECI	Earth-Centered Inertial
ECMWF	European Centre for Medium-Range Weather Forecasts
EOF	Empirical Orthogonal Function
EWH	Equivalent Water Height
FFT	Fast Fourier Transform
GFZ	German Research Centre for Geosciences
GIA	Glacial Isostatic Adjustment
GOCE	Gravity field and steady-state Ocean Circulation Explorer
GPS	Global Positioning System
GRACE	Gravity Recovery and Climate Experiment
GRACE-FO	GRACE Follow-On
GRM	Gravity Research Mission
ITSG	Institute of Geodesy - TU Graz
KBR	K-Band Ranging
LEO	Low Earth Orbit
LISA	Laser Interferometer Space Antenna
LMA	Levenberg-Marquardt Algorithm
LPT	Linear Perturbation Theory
LRI	Laser Ranging Interferometer
MAGIC	Mass Change and Geosciences International Constellation
MWI	Microwave Ranging Instrument
NASA	National Aeronautics and Space Administration
NGGM	Next Generation Gravity Mission
NWP	Numerical Weather Prediction
OBP	Ocean Bottom Pressure
ONERA	Office National d'Études et de Recherches Aérospatiales
PSD	Power Spectral Density
RMS	Root Mean Square
SH	Spherical Harmonics
SHS	Spherical Harmonics Synthesis
SST	Satellite-To-Satellite Tracking
TWS	Terrestrial Water Storage

Nomenclature

a	Semi-major axis
a_e	Brillouin sphere radius, Earth equatorial radius
A	Design matrix
A	Monodromy matrix
A	Data matrix
A_r	Reduced data matrix
$A_{\ddot{x}}$	Acceleration ASD
A_ρ	Inter-satellite range ASD
A_{km}, B_{km}	Lumped coefficients
B	Constraint design matrix
$\bar{c}$	Constraint vector
C_{lm}, S_{lm}	Stokes coefficients, Spherical Harmonics coefficients
$\bar{C}_{lm}, \bar{S}_{lm}$	Fully-normalized Stokes coefficients
$\tilde{C}_{lm}, \tilde{S}_{lm}$	Compact fully-normalized SH coefficients in orbital elements expansion
e	Eccentricity
F_{lmp}, F_{lmk}	Inclination functions
$\bar{F}_{lmp}, \bar{F}_{lmk}$	Fully-normalized inclination functions
$\bar{F}'_{lmp}, \bar{F}'_{lmk}$	Fully-normalized inclination functions derivatives
$\bar{F}^*_{lmp}, \bar{F}^*_{lmk}$	Fully-normalized cross-track inclination functions
f	Frequency in Hz
Δf	Frequency resolution
f_{km}	Lumped series frequency in Hz
f_s	Sampling frequency
f_u, f_v, f_w	Radial, along-track, cross-track forcing terms
$f_y(l)$	Gravity functional degree common factor
G_{lpq}	Eccentricity functions
H	Equivalent Water Height
I	Identity matrix
I	Inclination
J	Cost function
L	Cut-off degree
l	Degree
m	Order
M	Mean anomaly
M_{IR}	ECEF to ECI rotation matrix
M_{RI}	ECI to ECEF rotation matrix
n	Unperturbed orbital frequency
N	Normal matrix
N_d	RGT number of nodal days
N_r	RGT number of revolutions
N_p	Constellation planes, different ground-tracks sampled
P_{lm}	Associated Legendre Polynomials
$\bar{P}_{lm}$	Fully-normalized associated Legendre Polynomials
P_u, P_v, P_w	Radial, along-track, cross-track forcing term cosine amplitudes

P_{cc}	A-priori parameter covariance
P_{xx}	Parameter covariance
P_{yy}	Observation covariance
Q_u, Q_v, Q_w	Radial, along-track, cross-track forcing term sine amplitudes
r	Orbit radius
$\bar{r}$	Position vector
$r_{1/2}$	Gaussian smoothing radius
R_1, R_2, R_3	Rotation matrices along X, Y, Z axes
R_u, R_v, R_w	Radial, along-track, cross-track constant forcing term
S_ω	Skew-symmetric angular velocity matrix
T	Disturbing potential
T_o	Gravity field solution time window
T_r, T	RGT repeatability period
T_s	Sampling time
T_{IR}	ECEF to ECI full-state rotation matrix
T_{RI}	ECI to ECEF full-state rotation matrix
U	Normal potential
U, V	Left, right singular vector matrix
u, v, w	Radial, along-track, cross-track displacements, local orbital frame
$\dot{u}, \dot{v}, \dot{w}$	Radial, along-track, cross-track velocity
$\ddot{u}, \ddot{v}, \ddot{w}$	Radial, along-track, cross-track accelerations
V	Gravity potential
$\bar{v}$	Velocity vector
W	Weight matrix
$\bar{x}$	Design vector
$\bar{x}$	State vector
$\bar{x}$	Parameter vector
$\hat{x}$	Estimated parameter vector
$\bar{y}$	Observation vector
β_{km}	Lumped series normalized frequencies
γ_{km}	Lumped series integer frequencies
$\delta\bar{x}$	State perturbation
δt	Time perturbation
δ_l	RMS per coefficient per degree
$\bar{\epsilon}, \bar{\epsilon}_y$	Observation residual vector
$\bar{\epsilon}_c$	Constraint residual vector
ϵ_i	Variance contribution of i-th singular value
η	Collinear formation half of angular separation
θ	Co-latitude
θ	Earth rotation angle
$\dot{\theta}$	Earth's rotation angular velocity
λ	LMA damping factor
λ	Longitude
λ_l	Gravity field spatial resolution, half-wavelength
ρ	Inter-satellite range
ρ_0	Nominal inter-satellite range
$\Delta\rho$	Inter-satellite range deviation from nominal
ρ_x, ρ_y	Inter-satellite range line-of-sight frame components
σ_l^2	Degree variance
σ_i	Singular value
σ_{km}	Spectral observation error

σ_y^2	Allan variance
σ_y	Allan deviation
$\sigma_y^2(\phi, \lambda)$	Gravity functional commission error variance
$\hat{\sigma}_y^2$	Gravity functional averaged commission error variance
$\hat{\sigma_y}$	Gravity functional averaged commission errror
τ	Collinear formation half of time separation
ϕ	Latitude
Φ	ECI state transition matrix
Φ^R	ECEF state transition matrix
ψ_{km}	Lumped series phase angle
$\dot{\psi}_{km}$	Lumped series angular frequencies
Ω	Right ascension of ascending node
$\dot{\Omega}$	Inertial nodal precession rate
ω	Argument of periapsis
ω	Forcing frequency
$\bar{\omega}$	Angular velocity vector
ω_o	Argument of latitude
ω_e	Earth-fixed longitude of the ascending node
$\dot{\omega}_o$	Orbital frequency
$\dot{\omega}_e$	Earth-fixed nodal frequency

List of Figures

List of Tables

1 Introduction

Since the beginning of the space era, scientists have strived to improve our knowledge of Earth's gravity field. This not only enables more precise modelling of satellite orbits but can also provide insightful knowledge about mass redistribution processes occurring in our planet.

In the 1960s, long-term integrated effects on satellite orbits were employed to determine the Earth's gravity field from ground observations (Whipple & Lundquist, 1967). Atmospheric errors were, however, a limiting factor, and only coefficients up to approximately order 12 to 16 could be first retrieved (Gaposchkin & Lambeck, 1971). Further efforts combined with gravity surveys on land and altimetry lead to solutions up to degree 36 (Lambeck & Coleman, 1983).

Wolff (1969) suggested the concept of Satellite-To-Satellite Tracking (SST) for the first time to measure Earth's gravity field. Gravity potential irregularities would appear as variations mainly in the along-track velocity. In this way, the adverse effect of the atmosphere is prevented. The concept was proven a decade later with GEOS-3/ATS-6 relative tracking (Hajela, 1978) and Apollo/ATS-6 (Vonbun et al., 1980), consisting of high-low SST concepts. National Aeronautics and Space Administration (NASA) proposed to launch a low-low architecture consisting of two satellites flying in a collinear formation in a polar orbit as part of the Geopotential Research Mission (Keating et al., 1986). The mission was, however, cancelled and later led to the Gravity Recovery and Climate Experiment (GRACE) mission.

The GRACE mission was launched in 2002, and the first gravity field results were obtained a few years later (Tapley et al., 2004). For this purpose, a Microwave Ranging Instrument (MWI) and dual one-way phase measurements were employed (Kim & Tapley, 2002). While the expected mission lifetime was 5 years, the mission provided monthly gravity field data until June 2017 (Mayer-Gürr et al., 2016). The great success led to the launch of GRACE Follow-On (GRACE-FO), which is operational since June 2018 (Landerer et al., 2020). Furthermore, it carried a Laser Ranging Interferometer (LRI) that operated continuously for 50 days, showing significantly less range noise (Abich et al., 2019) and paving the way for ranging systems for future Gravity Research Missions (GRMs).

Alongside, two more GRMs have been launched. The German Challenging Minisatellite Payload (CHAMP) mission flew in a slightly lower orbit than GRACE from 2000 to 2010. It consisted of a high-low architecture based on GPS measurements and three-axis accelerometers to accurately model non-gravitational accelerations (Reigber et al., 2002). The Gravity field and steady-state Ocean Circulation Explorer (GOCE) mission was launched in 2009, and employed an on-board three-axis gradiometer that enabled the retrieval of gravity field data

with unprecedented accuracy thanks to a lower orbit and a drag-free system that compensated non-gravitational accelerations (Battrick et al., 1999; Canuto, 2008).

While GRACE-FO continues to provide time-varying gravity field solutions, data have shown some limitations for certain scientific applications. These are associated with insufficient spatial or time resolution. For example, mass redistributions due to ocean and atmospheric tides occur at higher temporal frequencies. Tidal models, although imperfect, aim at capturing their contribution (Knudsen & Andersen, 2002; Stammer et al., 2014). Pressure redistributions and continental hydrology also contribute to high-frequency mass variations at smaller spatial scales. Atmospheric and ocean circulation contributions can be mitigated through de-aliasing models such as the Atmosphere and Ocean Dealiasing Level-1B product (AOD1B) (Shihora et al., 2022), which employs ground observations.

For this reason, new missions have been proposed in the past aiming to improve the spatial and temporal resolution of gravity field products directly (Bender et al., 2008; Panet et al., 2012). As a result, the NASA/ESA joint mission Mass Change and Geosciences International Constellation (MAGIC)/Next Generation Gravity Mission (NGGM) is currently under development (Haagmans et al., 2020; Massotti et al., 2021). The mission will employ Bender configuration, consisting of two pairs of satellites flying in a collinear formation at a polar orbit (Grace-Continuity) and an inclined orbit with $i = 65 - 75°$ (NGGM), which will be launched in 2028 and the early 2030s, respectively (Bender et al., 2025). Moreover, the ranging system will consist of a laser interferometer capable of providing ranging measurements to nm accuracy (Nicklaus et al., 2020).

The NGGM/MAGIC mission also aims to incorporate a drag-free system. This control system allows a satellite to compensate for any non-gravitational accelerations such that it is in free-fall. The system was successfully implemented in the GOCE mission (Canuto, 2008). Other missions, such as Laser Interferometer Space Antenna (LISA) (Armano et al., 2016) or the Taiji and Taijin missions, have also employed a drag-compensation system successfully (Jiao et al., 2024). Drag-free feasibility analyses have also been conducted for the upcoming NGGM/MAGIC mission (Cesare et al., 2022; Massotti et al., 2020), showing the need for such system, mainly in the along-track component, and especially the need for fine pointing control to avoid instrument performance degradation.

While the Bender configuration will certainly improve the current state of GRACE-FO gravity data products, alternative formations to the collinear configuration have been proposed. Runge et al. (2001) proposed a cartwheel formation first for interferometric purposes. Subsequently, it was reconsidered for gravity research missions to also provide radial sensitivity (e.g. Sneeuw et al., 2008; Wei et al., 2015; Wiese, Nerem, and Lemoine, 2011; Wiese et al., 2008). Alternatively, pendulum configurations have been suggested as a variation of collinear formations with cross-track sensitivity (e.g. Ellmer, 2011; Li et al., 2016; Sharifi et al., 2007). LISA-type formations have also been considered to enable cross-track sensitivity (Sharifi et al., 2007; Sneeuw & Schaub, 2005). Furthermore, Elsaka et al. (2013) suggested a so-called helix formation as well as a slightly out-of-plane third satellite to the collinear formation, so-called GRAPEN. Liu et al. (2024) also analysed the capabilities of a Starlink-like constellation for gravity field recovery. Purkhauser and Pail (2020) analysed triple-pair constellations. Moreover, few studies have combined different types of formations with the Bender configuration concept (Daras et al., 2023). Lastly, it is important to account for the new design and operational problems that alternative formations might pose on the mission and the satellite subsystems, likely more challenging due to inherent formation complexity (e.g. Wiese et al., 2008).

In the past, gravity field error analysis has been performed using a spectral analytical approach that is based on the lumped coefficient theory (Kaula, 1966). This approach relies on the

computation of inclination (Gooding & Wagner, 2008; Kostelecký et al., 1986) and eccentricity functions (Lian-da & Ming-jiang, 2022; Wnuk, 1997). The methodology was proposed to analyse gravity field error from intersatellite range-rate observations (Colombo, 1984). This idea has also been applied to satellite gradiometry (Rummel & Colombo, 1985) and GPS observations (Colombo, 1986; Smith et al., 1989). Additional studies have explored the combined effect of gradiometers and GPS (Schrama, 1990, 1991b). Sneeuw (2000) delved deeper into the collinear formation and described a spectral approach to intersatellite ranging, among other observations. Besides, the analytical methodology has recently been able to describe pendulum formations through the convolution of the intrinsic time-varying behaviour of the formation (Li et al., 2016).

However, with the improvement of computational capabilities, end-to-end simulation-based studies have become much more frequent. Kim and Tapley (2002) performed such simulation-based analysis for the GRACE mission. At the same time, the introduction of the Bender configuration has raised the need for optimization techniques to define an optimal inclination for the second satellite pair. Simulation-based approaches are computationally intense and not well-posed for optimization algorithms, thus typically requiring a reduction of the search space. Multiple studies have combined optimization techniques with a simulation-based approach (e.g. Wiese, Nerem, and Lemoine, 2011; Iran Pour et al., 2019; Ellmer, 2011).

Another important aspect is the definition of the gravity field error. Typically, this has been provided by summation over the order and plotting the error against the degree, so-called degree variances. Alternatively, one could compute the Root Mean Square (RMS) per coefficient per degree (Heiskanen & Moritz, 1967). Other approaches include spherical harmonic synthesis, i.e. gravity field functionals projected into the sphere. In this way, gravity anomalies can be retrieved. Here, north-south stripes can be observed, indicating spatial aliasing (e.g. Visser et al., 2010). Moreover, geoid heights (Schrama & Visser, 2006) or equivalent water heights could be retrieved (Wahr et al., 1998).

1.1. A look into GRACE data

GRACE/GRACE-FO mission provides monthly Earth's gravity field solutions. In this work, publicly available monthly solutions released by the Institute of Geodesy - TU Graz (ITSG) are employed (Kvas et al., 2019; Mayer-Gürr et al., 2018).

Mainly, monthly gravity field variations are attributed to the water mass redistribution in the atmosphere and oceans, as well as water and snow stored in land. Wahr et al. (1998) associated gravity field variability with mass variations within a thin layer at the Earth's surface and the solid Earth deformation in response to these mass anomalies. This allows the definition of Equivalent Water Height (EWH). The computation of EWH directly from GRACE unconstrained data results in north-south striping patterns. Figure 1.1 shows the striping pattern for two monthly solutions: September 2004 and March 2007. They correspond to a resonant case and a non-resonant case, respectively.

In Figure 1.1b, the stripe patterns arise despite the non-resonant orbit of the formation in March 2007. To explain these phenomena, it is paramount to introduce the concept of degree variances. They describe the power of the gravity field at different spatial frequencies. Along with the monthly gravity field solutions, error estimates for the gravity field coefficients are provided. From degree variances, RMS per coefficient per degree can be employed to provide error estimates in the frequency spectrum (Dickey et al., 1997). The latter metric is employed in Figure 1.2 to compare the computed gravity solution and the error estimates for the two months discussed. Both monthly solutions show that the signal is dominated by noise at higher

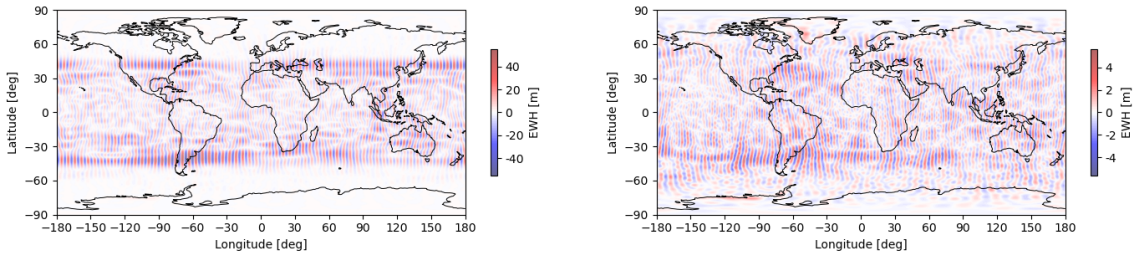

(a) September 2004 **(b)** March 2007

Figure 1.1: EWH retrieved from ITSG-2018 GRACE solutions

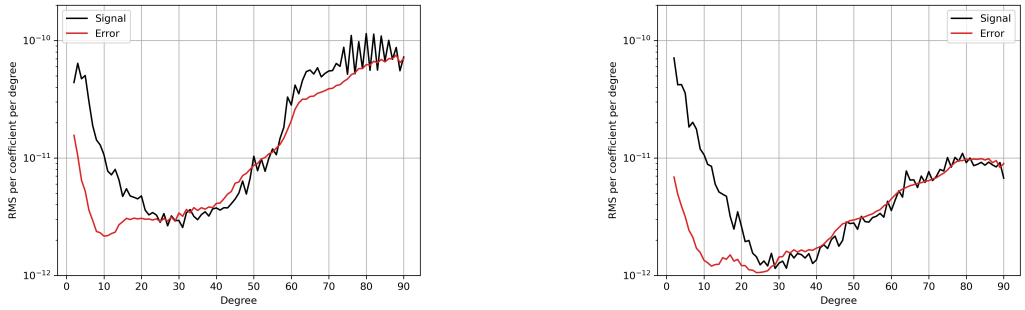

(a) September 2004 **(b)** March 2007

Figure 1.2: RMS per coefficient per degree from ITSG-2018 GRACE: gravity field solution vs. commission error

frequencies. As a result, the characteristic stripes at the relevant frequencies appear (Schrama et al., 2007).

The actual cause of the striping is unclear. Wahr et al. (2006) suggested two categories of errors. Category (i) errors are associated with errors in GRACE monthly solutions, i.e., measurement noise and aliasing. Category (ii) errors appear due to imperfect background models that account for short-periodic gravity field variability. The striping patterns in EWH also arise in gravity anomalies. The problem is typically circumvented by applying spatial smoothing through a Gaussian filter that behaves as a low-pass filter in the spatial domain (Jekeli, 1981; Wahr et al., 1998). In Figure 1.3, application of a half-width radius of 750 km removes the previously observed striping, uncovering the monthly water variation signal. In addition, Wahr et al. (2006) pointed out the correlation between even and odd degree coefficient pairs of the same order and proposed to combine spatial smoothing with decorrelation filters. Alternative filtering techniques include Decorrelation and Denoising Kernel (DDK) filters (Kusche et al., 2009; Kusche, 2007), non-symmetric filters that incorporate full covariance information (Klees et al., 2008), Empirical Orthogonal Functions (EOFs) filtering (Wouters & Schrama, 2007), or mascon approaches (Schrama et al., 2014).

While both resonant and non-resonant orbits showed the striping patterns, comparison of the two solutions depicts a much higher signal degradation for the resonant orbit of September 2004 (see Figure 1.2). Figure 1.1a also demonstrates a much higher noise level, especially in equatorial regions. This is an indication of spatial aliasing.

Apart from the standard deviation of the gravity field parameters, full covariance information can be retrieved by inversion of the released normal matrices. Subsequently, covariance propagation to the sphere results in the expected error estimates for the spherical harmonics

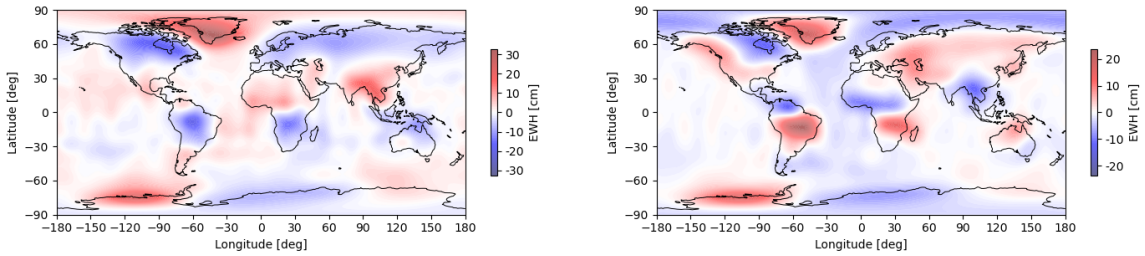

(a) September 2004 **(b)** March 2007

Figure 1.3: EWH with Gaussian spatial smoothing with $r_{1/2}$=750 km computed from ITSG-2018 GRACE solutions

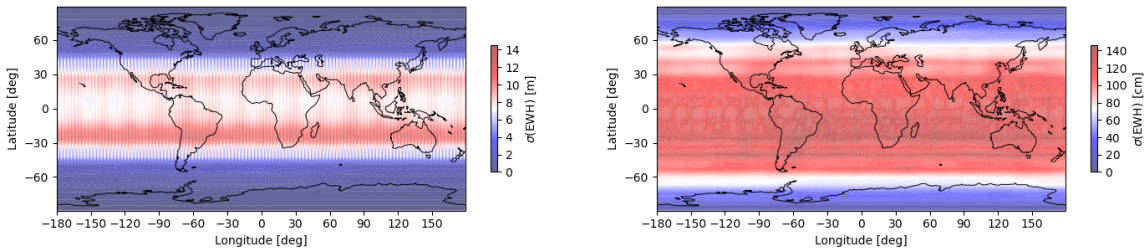

(a) September 2004 **(b)** March 2007

Figure 1.4: Covariance propagation to EWH from ITSG-2018 GRACE normal matrix

synthesis. Figure 1.4 presents EWH error estimates computed for the two monthly solutions at hand.

The EWH error magnitudes on the sphere are consistent with the unsmoothed EWH from Figure 1.1. Furthermore, it can be observed that the resonance gives rise to striping patterns also in the propagated EWH error estimates, while this is not the case when the mission does not fall into a resonance. Moreover, resonances have a more detrimental effect in equatorial regions, whereas the March 2007 solution shows a constant error band that extends to higher latitudes. This is in agreement with the fact that the stripes' magnitude fades away at higher latitudes in the EWH signal (see Figure 1.1a).

1.2. Relevance of measuring the Earth's gravity field

For more than two decades, GRACE/GRACE-FO have provided monthly gravity field data that has made a major impact across many disciplines (Chen et al., 2022; Doorn et al., 2016; Tapley et al., 2019). In hydrology, annual and seasonal monitoring of water availability has been crucial to water resource management. For example, Terrestrial Water Storage (TWS) is applied to flood detection (Reager & Famiglietti, 2009) or drought monitoring (Houborg et al., 2012; Vishwakarma, 2020). Moreover, determination of mass changes in ice sheets and glaciers, as well as sea level rise, supports planning and mitigation strategies against global warming, among other things, especially in coastal regions (WCRP Global Sea Level Budget Group, 2018). Satellite gravimetry has also enabled multiple studies on solid Earth deformation from large earthquakes (e.g., Han et al., 2006). It has also been essential to enhance our knowledge of plate tectonics and mantle dynamics, especially through its capabilities to measure remote areas. Moreover, Glacial Isostatic Adjustment (GIA) models can be improved through gravity field data records. It consists of slow land uplift caused by Earth's delayed viscoelastic response to

the removal of ancient ice sheets loading after melting. Thus, they have led to advancements in rheology as well as to enhanced insights on paleoclimates and past ice ages (Tamisiea et al., 2007). In oceanography, GRACE data enabled global Ocean Bottom Pressure (OBP) observations (Chambers & Willis, 2010). It provides information on ocean circulation, crucial to understanding marine ecosystems and global climate, in particular, weather events such as El Niño (Song & Zlotnicki, 2008). In geodesy, geocenter motion can be estimated and forecast from variations in the degree 1 coefficients, key to defining precise reference systems, among other applications (Heiskanen & Moritz, 1967; Sun et al., 2016; Swenson et al., 2008). Apart from GRACE solutions, ancillary data products can also be employed for a variety of applications. For instance, reconstruction of accelerometer data enables the retrieval of high-resolution thermospheric density, especially near highly sampled regions such as the poles (March et al., 2019).

While satellite gravimetry applications are numerous, there still exist high-frequency mass variations that cannot be appropriately observed due to limited temporal or spatial aliasing. For this reason, it is of high interest to identify the time and spatial scales at which the different geophysical processes occur. Sneeuw et al. (2004) condensed this information into Figure 1.5. Pail et al. (2015) performed an extensive analysis in terms of EWH and defined science requirements for future gravity research missions according to societal needs.

Future GRMs shall improve current spatial and temporal resolution capabilities to unveil new insights about our planet. Better spatial resolution is important to monitor the contribution of

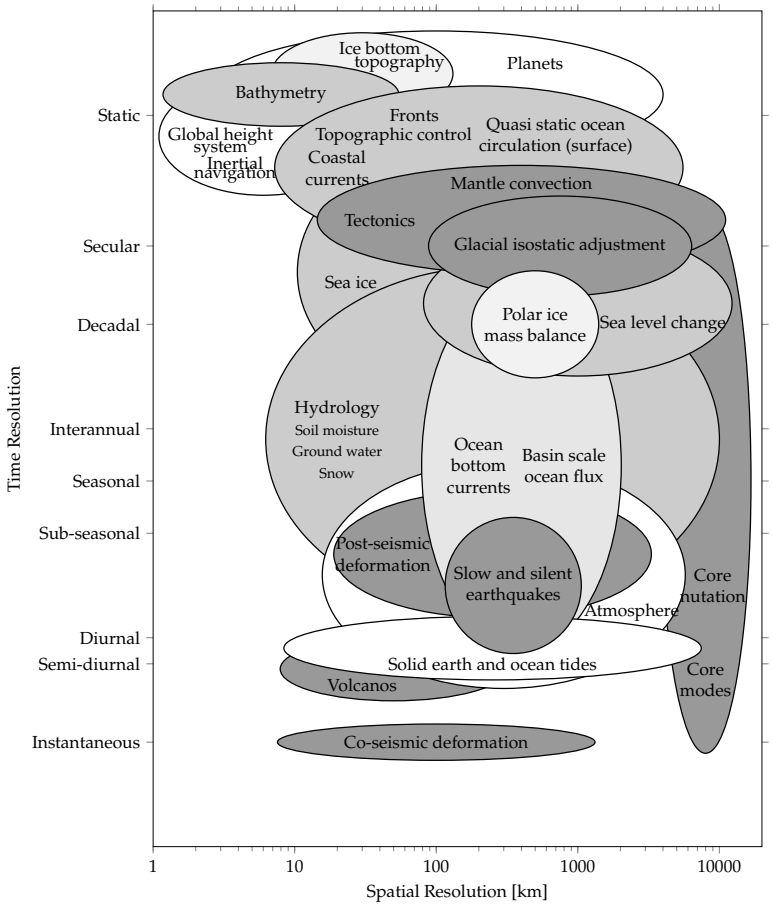

Figure 1.5: Spatial and temporal scales of geophysical processes. Adapted from Sneeuw et al. (2004).

key catchment basins that are smaller or near the resolution limit of current satellite gravimetry capabilities (Pail et al., 2015). This will also contribute to reducing signal leakage from adjacent areas. Increasing the temporal resolution would represent a step towards near-real-time gravimetry. In this way, less or no reliance on de-aliasing models would be required, thus reducing uncertainty in the solutions (Pail et al., 2015). Errors induced by undersampling of high-frequency processes will also be reduced, thereby causing an overall improvement in data quality (Massotti et al., 2023), potentially mitigating observed noise at higher degrees (Wahr et al., 2006). Furthermore, better signal separation would be possible with improved data (Pail et al., 2015).

As satellite gravimetry data has multiple applications, improvements on the spatio-temporal resolution of Earth's gravity field data would similarly be beneficial across several domains. In hydrology, accurate determination of medium and small river basins could bridge the gap towards closing terrestrial water balance (Famiglietti & Rodell, 2013; Sheffield et al., 2009) and open new research possibilities on unexplored topics such as atmospheric water balance (C. Lorenz et al., 2014) and complex feedback behaviours intertwined in the Earth system (Seneviratne et al., 2006). Concerning the cryosphere, permafrost thawing, snow melt, and mountain glaciers typically occur at spatial scales below current spatial resolution capabilities (Luthcke et al., 2013; Pail et al., 2015). Hence, the determination of its contribution is nowadays challenging. Besides this, GIA needs better spatial resolution to separate its remnant effect on the temporal gravity field from mass variations associated with present-day processes (e.g., Ivins et al., 2013). Moreover, improvements in temporal resolution could eventually lead to near real-time monitoring of natural disasters, which would also allow better forecasting (Pail et al., 2015). In oceanography, coastal regions show different sea level signals than the open ocean due to smaller spatial scales and the interaction with continental hydrology (e.g., Chambers and Willis, 2010). In this way, better spatial resolution would improve tidal models, circumventing current altimetry limitations, especially near the coast (Killett et al., 2011; Pail et al., 2015). Moreover, some main drivers of ocean circulation also occur at smaller spatial scales (Saynisch et al., 2014). The Atlantic Meridional Overturning Circulation (AMOC) variability, for example, is crucial to climate regulation in north-western Europe (Bingham & Hughes, 2008, 2009). Regarding plate tectonics, an improved spatial resolution would allow observation of earthquakes with magnitudes greater than seven (Han et al., 2013). For example, this could be significantly beneficial in the Mediterranean region, densely populated and characterized by this type of seismic activity (Fullea et al., 2015). Furthermore, solid Earth sciences research aims at creating a 4D dynamic Earth model that employs, among others, refined gravity field constraints to predict near-surface motion, deformation, and derive insights into the interior of our planet (see e.g., the "4D Dynamic Earth Project", 2025).

1.3. Research questions

Despite the significant contributions of GRACE/GRACE-FO temporal gravity field data, it presents spatial and temporal resolution limitations that do not meet current scientific and societal needs. Therefore, new GRMs that improve present GRACE-FO capabilities must be defined. For this purpose, plenty of simulation-based studies have analysed commission errors in gravity field retrieval for different satellite formations as well as Bender-like constellations. As has been discussed previously, more elaborate constellations require greater optimization efforts to maximize mission performance. However, only a few of these studies have applied optimization techniques to the proposed configurations, mainly due to the intense computational burden. Additionally, analytical approaches have been progressively abandoned due to their limitations and the complexity compared to simulation-based approaches, which can be

relatively quickly set up thanks to multiple available astrodynamics software. The application of such analytical techniques to alternative formations has been identified as the main research gap in literature. Moreover, this would enable refined optimization of orbital configuration parameters.

As a result, the main research question and different subquestions have been formulated.

> Can Bender configuration or other multi-satellite constellations better mitigate temporal and spatial aliasing in a gravity research mission?

1. How can the analytical approach be applied to multi-satellite constellations? What are the limitations of this methodology?
2. How can equatorial stripe errors be defined?
3. What are the optimal parameters for a Bender configuration? How does it perform in terms of spatial aliasing errors?
4. What are the optimal parameters of a multi-satellite constellation for a high temporal resolution GRM? How does it perform in terms of spatial aliasing errors?
5. How do instrument errors impact the selected optimal configurations?

1.4. Thesis overview

In this work, an analytical approach is employed to study alternative orbital configurations that circumvent the observed spatial aliasing in equatorial regions as well as to enable gravity field solutions at higher temporal frequencies. In chapter 2, the mathematical foundations of the spectral observation model are developed for GPS and intersatellite ranging for a collinear formation. In this way, analytical expressions for the lumped coefficients are formulated in terms of the Spherical Harmonics (SH) coefficients. Chapter 3 presents the resulting linear system. Subsequently, the gravity field error through the least squares methodology is presented, relating errors in the lumped coefficients to errors in the SH coefficients. Moreover, error models for the spectral observations and error sources are discussed. In chapter 4, a simulation framework is presented to validate the analytical observation spectra through Fourier analysis of a perfectly periodic orbit. The gravity field error analysis results are examined in chapter 5. Three different configurations are studied: a single satellite collinear pair, a Bender configuration, and a constellation of satellite pairs. Conclusions of the work and future recommendations are outlined in chapter 6.

2

Analytical observation model

This chapter presents the derivation of the analytical expressions for the different observations considered in this work. To begin with, the concept of gravity potential is introduced. Since the gravity field is conservative, it can be expressed as the gradient of a scalar potential field.

$$\vec{g} = -\nabla V \tag{2.1}$$

Gravity potentials of a certain body satisfy the Laplace equation outside the body at hand.

$$\nabla^2 V = 0 \tag{2.2}$$

As a result, the gravity potential is generally expressed in terms of spherical harmonics.

$$V = \frac{\mu}{r} \sum_{l=0}^{\infty} \sum_{m=0}^{l} \left(\frac{a_e}{r}\right)^l P_{lm}(\sin\phi) \left(C_{lm} \cos m\lambda + S_{lm} \sin m\lambda\right) \tag{2.3}$$

By definition, $C_{00} = 1$ is the central term of the potential, and $C_{10} = C_{11} = S_{11} = 0$ by appropriate definition of the reference system. The expression can be rewritten as:

$$V = U + T = \frac{\mu}{r} + T \tag{2.4}$$

with T the disturbing potential.

$$T = \frac{\mu}{r} \sum_{l=2}^{L} \sum_{m=0}^{l} \left(\frac{a_e}{r}\right)^l \bar{P}_{lm}(\sin\phi) \left(\bar{C}_{lm} \cos m\lambda + \bar{S}_{lm} \sin m\lambda\right) \tag{2.5}$$

Typically, the infinite summation over the degree l is truncated to a cut-off degree L. The evaluation of this expression requires the computation of the associated Legendre polynomials P_{lm}. Recursive formulations and the normalization employed are described in appendix A.

The subject of gravity field modelling consists of the estimation of the spherical harmonics coefficients of the disturbing potential, so-called Stokes coefficients. For this purpose, this chapter relates them to different observations through analytical expressions.

2.1. The lumped series

To begin with, it is necessary to first introduce the concept of a lumped series. They consist of the fundamental expression for any spectral observation.

$$f(t) = \sum_{k=-L}^{L} \sum_{m=0}^{L} A'_{km} \cos \psi_{km} + B'_{km} \sin \psi_{km} \tag{2.6}$$

Their name arises from the fact that coefficients A_{km}, B_{km} consist of a summation over the degree. The phase terms ψ_{km} can be represented as an initial phase angle and a frequency term:

$$\psi_{km} = \psi^0_{km} + \dot{\psi}_{km} t \tag{2.7}$$

As such, the lumped expression resembles a Fourier expansion over specific frequency terms, so-called orbital frequencies. Thus, the observation analytical model is a spectral model. Instead of considering observations in the time domain, the methodology focuses on developing analytical formulations for the frequency-domain observations, the lumped coefficients. In chapter 3, error models for the lumped coefficients are derived from the instrument error spectra.

2.1.1. The initial phase angle

For the sake of simplicity, the observation expressions hereafter formulated consider no initial phase angle, i.e. $\psi^0_{km} = 0$. It can be shown that any lumped expression with a non-zero initial phase angle can be rewritten as a new lumped series with no initial phase angle:

$$f(t) = \sum_{k=-L}^{L} \sum_{m=0}^{L} A_{km} \cos \dot{\psi}_{km} t + B_{km} \sin \dot{\psi}_{km} t \tag{2.8}$$

where the coefficients can be related with a simple rotation matrix:

$$\begin{bmatrix} A_{km} \\ B_{km} \end{bmatrix} = \begin{bmatrix} \cos \psi^0_{km} & \sin \psi^0_{km} \\ -\sin \psi^0_{km} & \cos \psi^0_{km} \end{bmatrix} \begin{bmatrix} A'_{km} \\ B'_{km} \end{bmatrix} \tag{2.9}$$

2.2. Line potential

In this section, the concept of line potential is introduced. It is assumed that the potential along the perturbed orbit can be represented as the potential along a nominal orbit. In this way, it is possible to reformulate every term V_{lm} of the potential in terms of the mean orbital elements (Kaula, 1966).

$$V_{lm} = \frac{\mu}{r} \left(\frac{a_e}{r} \right)^l \sum_{p=0}^{l} F_{lmp}(I) \sum_{q=-\infty}^{q=\infty} G_{lpq}(e) S_{lmpq}(\omega, M, \Omega, \theta) \tag{2.10}$$

where

$$\begin{aligned} S_{lmpq}(\omega, M, \Omega, \theta) = &\begin{bmatrix} C_{lm} \\ -S_{lm} \end{bmatrix}_{l-m:\text{odd}}^{l-m:\text{even}} \cos \left[(l-2p)\omega + (l-2p+q)M + m(\Omega - \theta) \right] \\ &\begin{bmatrix} S_{lm} \\ C_{lm} \end{bmatrix}_{l-m:\text{odd}}^{l-m:\text{even}} \sin \left[(l-2p)\omega + (l-2p+q)M + m(\Omega - \theta) \right] \end{aligned} \tag{2.11}$$

and $F_{lmp}(I)$ and $G_{lpq}(e)$ are functions of the inclination and eccentricity, respectively.

Typically, eccentricities are small, and the summation over the q index can be truncated to $q \pm 2$. For this work, a circular reference orbit is assumed. Therefore, terms with $q \neq 0$ are zero, whereas $G_{lp0}(e) = 1$. Hence, only the computation of the inclination functions is required. The simple approach based on the Fast Fourier Transform (FFT) proposed by Wagner (1983) has been applied. Similarly, it is convenient to employ the normalized inclination functions. Appendix B delves deeper into their computation. Additionally, the circular reference orbit assumption enables the introduction of the argument of latitude ω_o. Moreover, the Earth-fixed longitude of the ascending node ω_e is defined (see also Figure 2.1).

$$\omega_o = M + \omega = \omega_o^0 + \dot{\omega}_o t \tag{2.12}$$

$$\omega_e = \Omega - \theta = \omega_e^0 + \dot{\omega}_e t \tag{2.13}$$

The rate of the longitude of the ascending node is negative, i.e. $\omega_e < 0$, since $\dot{\theta} > 0$ and $|\dot{\Omega}| << |\dot{\theta}|$. The orbital frequency is positive by definition, i.e., $\dot{\omega}_o > 0$.

Changing the index of the summation to $k = l - 2p$ leads to a simplified expression of Eq. (2.10).

$$V_{lm} = \frac{\mu}{r}\left(\frac{a_e}{r}\right)^l \sum_{\substack{k=-l \\ l-k=2p}}^{l} \bar{F}_{lmk}(I)\left\{\tilde{C}_{lm}\cos\left(k\omega_o + m\omega_e\right) + \tilde{S}_{lm}\sin\left(k\omega_o + m\omega_e\right)\right\} \tag{2.14}$$

where

$$\tilde{C}_{lm} = \begin{bmatrix} \bar{C}_{lm} \\ -\bar{S}_{lm} \end{bmatrix}_{l-m=\text{odd}}^{l-m=\text{even}} \qquad \tilde{S}_{lm} = \begin{bmatrix} \bar{S}_{lm} \\ \bar{C}_{lm} \end{bmatrix}_{l-m=\text{odd}}^{l-m=\text{even}}$$

Note that the sum over k is restricted to those terms where l, k have the same parity. Subsequently, it follows that the potential takes the form of a lumped series:

$$V = \sum_{k=-L}^{L}\sum_{m=0}^{L} A_{km}\cos\psi_{km} + B_{km}\sin\psi_{km} \tag{2.15}$$

with

$$\begin{bmatrix} A_{km} \\ B_{km} \end{bmatrix} = \sum_{l=l_{min},2}^{L} \frac{\mu}{r}\left(\frac{a_e}{r}\right)^l \bar{F}_{lmk}(I)\begin{bmatrix} \tilde{C}_{lm} \\ \tilde{S}_{lm} \end{bmatrix} \tag{2.16}$$

$$\psi_{km} = k\omega_0 + m\omega_e \tag{2.17}$$

The summation for the lumped coefficients A_{km}, B_{km} runs from $l_{min} = \max(|k|, m, 2) + \delta$ where $\delta = 0$ when $k - \max(|k|, m, 2)$: even and $\delta = 1$ when $k - \max(|k|, m, 2)$: odd.

2.3. Potential derivatives along the orbit

To introduce the potential contribution to the orbit dynamics perturbations, it is needed to compute the potential gradient formulation. It is convenient to make use of a local orbital frame for this purpose.

From Eq. (2.15), the position along the orbit is determined by r, ω_0, ω_e, I. This defines a position in the inertial space $\vec{x}_s$ as follows:

$$\vec{x}_s = R_3(-\omega_e)R_1(-I)R_3(-\omega_0)\begin{pmatrix} r \\ 0 \\ 0 \end{pmatrix} \tag{2.18}$$

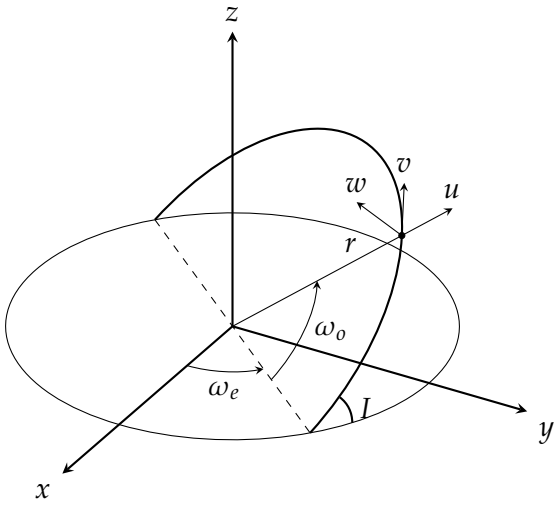

Figure 2.1: Orbital variables and local orbital frame

Alternatively, a perturbation $\Delta\vec{x}_s$ can be determined in a local orbital frame as (Balmino et al., 1996):

$$\vec{x}_s + \Delta\vec{x}_s = R_3(-\omega_e)R_1(-I)R_3(-\omega_0)\begin{pmatrix} r+u \\ v \\ w \end{pmatrix} \tag{2.19}$$

To determine how a change in the local orbital frame variable set $\vec{x}_i = \{u, v, w\}$ is related to the orbital variables r, ω_0, ω_e, I. Since there are four orbital variables, one can select 3 different subsets: $\vec{x}_a = \{r, \omega_0, \omega_e\}, \vec{x}_b = \{r, \omega_0, I\}, \vec{x}_c = \{r, \omega_e, I\}$. Applying the chain rule, therefore, results in the following expressions for the three subsets (Balmino et al., 1996; Koop, 1993).

$$\begin{bmatrix} dr \\ d\omega_o \\ d\omega_e \end{bmatrix} = \begin{bmatrix} 1 & 0 & 0 \\ 0 & \frac{1}{r} & \frac{\cos I}{r \sin I \cos \omega_o} \\ 0 & 0 & \frac{-1}{r \sin I \cos \omega_o} \end{bmatrix} \begin{bmatrix} du \\ dv \\ dw \end{bmatrix} \tag{2.20}$$

$$\begin{bmatrix} dr \\ d\omega_o \\ dI \end{bmatrix} = \begin{bmatrix} 1 & 0 & 0 \\ 0 & \frac{1}{r} & 0 \\ 0 & 0 & \frac{1}{r \sin \omega_o} \end{bmatrix} \begin{bmatrix} du \\ dv \\ dw \end{bmatrix} \tag{2.21}$$

$$\begin{bmatrix} dr \\ d\omega_e \\ dI \end{bmatrix} = \begin{bmatrix} 1 & 0 & 0 \\ 0 & \frac{1}{r \cos I} & 0 \\ 0 & \frac{\sin I \cos \omega_o}{r \cos I \sin \omega_o} & \frac{1}{r \sin \omega_o} \end{bmatrix} \begin{bmatrix} du \\ dv \\ dw \end{bmatrix} \tag{2.22}$$

From the above expressions, it follows directly that:

$$\frac{\partial V}{\partial u} = \frac{\partial V}{\partial r} \tag{2.23}$$

Taking the partial derivative of Eq. (2.15) results in:

$$\begin{aligned} \frac{\partial V}{\partial u} &= \sum_{k=-L}^{L} \sum_{m=0}^{L} A_{km}^{u} \cos\psi_{km} + B_{km}^{u} \sin\psi_{km} \\ \begin{bmatrix} A_{km}^{u} \\ B_{km}^{u} \end{bmatrix} &= \sum_{l=l_{min},2} -(l+1)\frac{\mu}{r^2}\left(\frac{a_e}{r}\right)^{l} F_{lmk}(I) \begin{bmatrix} \tilde{C}_{lm} \\ \tilde{S}_{lm} \end{bmatrix} \end{aligned} \tag{2.24}$$

Similarly, the acceleration in the along-track component can be computed from Eq. (2.20):

$$\frac{\partial V}{\partial v} = \frac{1}{r}\frac{\partial V}{\partial \omega_o} \tag{2.25}$$

Analogously, partial differentiation of equation Eq. (2.15) leads to:

$$\begin{aligned} \frac{\partial V}{\partial v} &= \sum_{k=-L}^{L} \sum_{m=0}^{L} A_{km}^{v} \cos\psi_{km} + B_{km}^{v} \sin\psi_{km} \\ \begin{bmatrix} A_{km}^{v} \\ B_{km}^{v} \end{bmatrix} &= \sum_{l=l_{min},2} \frac{\mu}{r^2}\left(\frac{a_e}{r}\right)^{l} F_{lmk}(I) \cdot k \begin{bmatrix} \tilde{S}_{lm} \\ -\tilde{C}_{lm} \end{bmatrix} \end{aligned} \tag{2.26}$$

From Eqs. (2.20) and (2.22), the following expressions for the cross-track derivative are obtained.

$$\frac{\partial V}{\partial w} = \frac{1}{r\sin\omega_o}\frac{\partial V}{\partial I} \tag{2.27}$$

$$\frac{\partial V}{\partial w} = \frac{1}{r\sin I\cos\omega_o}\left(\frac{\partial V}{\partial \omega_o}\cos I - \frac{\partial V}{\partial \omega_e}\right) \tag{2.28}$$

However, both expressions contain ω_o singularities. Multiplication by $\sin^2\omega_o$ and $\cos^2\omega_o$ respectively yields a singular-free formulation of the cross-track derivative (Schrama, 1989).

$$\frac{\partial V}{\partial w} = \frac{1}{r}\left\{\sin\omega_o\frac{\partial V}{\partial I} + \frac{\cos\omega_o}{\sin I}\left(\frac{\partial V}{\partial \omega_o}\cos I - \frac{\partial V}{\partial \omega_e}\right)\right\} \tag{2.29}$$

After some algebraic manipulation, the cross-track derivative reads as:

$$\begin{bmatrix} A_{km}^{w} \\ B_{km}^{w} \end{bmatrix} = \sum_{l=l_{min}^{*},2}^{L} \frac{\mu}{r^2}\left(\frac{a_e}{r}\right)^{l} F_{lmk}^{*}(I) \begin{bmatrix} \tilde{S}_{lm} \\ -\tilde{C}_{lm} \end{bmatrix} \tag{2.30}$$

where $F_{lmk}^{*}(I)$ represents the cross-track inclination functions (Balmino et al., 1996). Appendix B.3 derives them and develops the cross-track potential derivative formulation.

2.4. Hill equations

Once the observations for the gravity components have been computed, they can be introduced to the dynamics to derive the position observations. For this purpose, the Hill equations are employed. They consist of a linearized relative dynamics model that has the following form for arbitrary forcing terms f_u, f_v, f_w, corresponding to the radial, along-track, and cross-track accelerations, respectively (Hill, 1878) :

$$\begin{cases} \ddot{u} - 2n\dot{v} - 3n^2 u &= f_u \\ \ddot{v} + 2n\dot{u} &= f_v \\ \ddot{w} + n^2 w &= f_w \end{cases} \tag{2.31}$$

2.4.1. Homogeneous solution

The homogeneous part of the solution is obtained when $(f_u, f_v, f_w) = \vec{0}$. It represents the system response to an initial state perturbation (e.g., Schrama, 1989).

$$\begin{aligned} u(t) &= \left(-3u_0 - \frac{2}{n}\dot{v}_0\right)\cos nt + \frac{\dot{u}_0}{n}\sin nt + \left(u_0 + \frac{2}{n}\dot{v}_0\right) \\ v(t) &= \frac{2\dot{u}_0}{n}\cos nt + \left(6u_0 + \frac{4\dot{v}_0}{n}\right)\sin nt + (-6v_0 + 3\dot{v}_0)\,t + \left(v_0 - \frac{2\dot{u}_0}{n}\right) \\ w(t) &= w_0 \cos nt + \frac{\dot{w}_0}{n}\sin nt \end{aligned} \tag{2.32}$$

2.4.2. Non-resonant solution

In section 2.3, potential derivatives were derived in the local orbital frame. It was possible to define them as a lumped series. Therefore, it is interesting to compute the system response to periodic forcing terms. For an arbitrary periodic force, the system from Eq. (2.31) reads as:

$$\begin{cases} \ddot{u} - 2n\dot{v} - 3n^2 u &= P_u \cos \omega t + Q_u \sin \omega t \\ \ddot{v} + 2n\dot{u} &= P_v \cos \omega t + Q_v \sin \omega t \\ \ddot{w} + n^2 w &= P_w \cos \omega t + Q_w \sin \omega t \end{cases} \tag{2.33}$$

An analytical solution exists (e.g., Schrama, 1989).

$$\begin{aligned} u(t) &= \frac{-2nQ_v + \omega P_u}{\omega(n^2 - \omega^2)}\cos \omega t + \frac{2nP_v + \omega Q_u}{\omega(n^2 - \omega^2)}\sin \omega t \\ v(t) &= \frac{(3n^2 + \omega^2)P_v + 2n\omega Q_u}{\omega^2(n^2 - \omega^2)}\cos \omega t + \frac{(3n^2 + \omega^2)Q_v - 2n\omega P_u}{\omega^2(n^2 - \omega^2)}\sin \omega t \\ w(t) &= \frac{P_w}{n^2 - \omega^2}\cos \omega t + \frac{Q_w}{n^2 - \omega^2}\sin \omega t \end{aligned} \tag{2.34}$$

2.4.3. Resonant solution

The solutions presented above are undefined for constant forcing terms as well as those that match the orbital period, i.e., $\omega = 0, \pm n$. Such forcing terms need special treatment since they give rise to the so-called resonant solutions. The Hill equations system takes the following form for resonant forcing terms.

$$\begin{cases} \ddot{u} - 2n\dot{v} - 3n^2 u &= P_u \cos nt + Q_u \sin nt + R_u \\ \ddot{v} + 2n\dot{u} &= P_v \cos nt + Q_v \sin nt + R_v \\ \ddot{w} + n^2 w &= P_w \cos nt + Q_w \sin nt + R_w \end{cases} \tag{2.35}$$

Resonant solutions exist in the following form:

$$\begin{aligned} u(t) &= (a_u^0 + a_u^1 t)\cos nt + (b_u^0 + b_u^1 t)\sin nt + (c_u^0 + c_u^1 t) \\ v(t) &= (a_v^0 + a_v^1 t)\cos nt + (b_v^0 + b_v^1 t)\sin nt + (c_v^0 + c_v^1 t + c_v^2 t^2) \\ w(t) &= (a_w^0 + a_w^1 t)\cos nt + (b_w^0 + b_w^1 t)\sin nt + c_w^0 \end{aligned} \tag{2.36}$$

where the explicit form of the coefficients can be found in Schrama (1989, pp. 57-58).

2.5. GPS observations

Introducing the lumped expressions of the gradient of the potential for the non-resonant solutions, the periodic displacements caused by the non-resonant terms of the perturbing potential are obtained (Balmino et al., 1996; Colombo, 1984; Schrama, 1989). Note that the resonant term observations are not to be considered for the error analysis.

$$u(t) = \sum_{m=0}^{L} \sum_{k=-L}^{L} A_{km}^{\Delta u} \cos(\dot{\psi}_{km} t) + B_{km}^{\Delta u} \sin(\dot{\psi}_{km} t) \tag{2.37}$$

$$\begin{bmatrix} A_{km}^{\Delta u} \\ B_{km}^{\Delta u} \end{bmatrix} = \sum_{l=l_{min},2} \frac{-(l+1)\dot{\psi}_{km} + 2nk}{\dot{\psi}_{km}(n^2 - \dot{\psi}_{km}^2)} \frac{\mu}{r^2} \left(\frac{a_e}{r}\right)^l F_{lmk}(I) \begin{bmatrix} \tilde{C}_{lm} \\ \tilde{S}_{lm} \end{bmatrix} \tag{2.38}$$

$$v(t) = \sum_{m=0}^{L} \sum_{k=-L}^{L} A_{km}^{\Delta v} \cos(\dot{\psi}_{km} t) + B_{km}^{\Delta v} \sin(\dot{\psi}_{km} t) \tag{2.39}$$

$$\begin{bmatrix} A_{km}^{\Delta v} \\ B_{km}^{\Delta v} \end{bmatrix} = \sum_{l=l_{min},2} \frac{-(l+1)2n\dot{\psi}_{km} + k(3n^2 + \dot{\psi}_{km}^2)}{\dot{\psi}_{km}^2(n^2 - \dot{\psi}_{km}^2)} \frac{\mu}{r^2} \left(\frac{a_e}{r}\right)^l F_{lmk}(I) \begin{bmatrix} \tilde{S}_{lm} \\ -\tilde{C}_{lm} \end{bmatrix} \tag{2.40}$$

$$w(t) = \sum_{m=0}^{L} \sum_{k=-L}^{L} A_{km}^{\Delta w} \cos(\dot{\psi}_{km}) t + B_{km}^{\Delta w} \sin(\dot{\psi}_{km} t) \tag{2.41}$$

$$\begin{bmatrix} A_{km}^{\Delta w} \\ B_{km}^{\Delta w} \end{bmatrix} = \sum_{l^*_{min},2}^{L} \frac{1}{n^2 - \dot{\psi}_{km}^2} \frac{\mu}{r^2} \left(\frac{a_e}{r}\right)^l F^*_{lmk}(I) \begin{bmatrix} \tilde{S}_{lm} \\ -\tilde{C}_{lm} \end{bmatrix} \tag{2.42}$$

2.6. Collinear configuration

In this section, the intersatellite range lumped expressions are derived for a collinear configuration following Sneeuw (2000). The collinear configuration corresponds to the formation used in the GRACE mission. Two satellites are flying in the same orbital plane while tracking the intersatellite range. Figure 2.2 outlines this configuration.

The deviation from the nominal range can be approximated as the projection along the nominal line-of-sight.

$$\rho(t) = \sqrt{(\rho_0 + \Delta\rho_x)^2 + \Delta\rho_y^2} \approx \rho_0 + \Delta\rho_x \implies \Delta\rho(t) \approx \Delta\rho_x \tag{2.43}$$

This can be expressed in terms of the respective local orbital coordinates.

$$\begin{aligned} \Delta\rho(t) =& (\Delta v_A - \Delta v_B)\cos\eta + (\Delta u_A + \Delta u_B)\sin\eta = \\ =& (\Delta v(t+\tau) - \Delta v(t-\tau))\cos\eta + (\Delta u(t+\tau) + \Delta u(t-\tau))\sin\eta \end{aligned} \tag{2.44}$$

with $\tau = \eta/n$. Let's now compute every term based on the lumped expressions. First, the radial component is derived.

$$\begin{aligned} &\Delta u(t+\tau) + \Delta u(t-\tau) = \\ &\quad = \sum_{m=0}^{L} \sum_{k=-L}^{L} A_{km}^{\Delta u} \left[\cos\dot{\psi}_{km}(t+\tau) + \cos\dot{\psi}_{km}(t-\tau)\right] + B_{km}^{\Delta u} \left[\sin\dot{\psi}_{km}(t+\tau) + \sin\dot{\psi}_{km}(t-\tau)\right] \end{aligned} \tag{2.45}$$

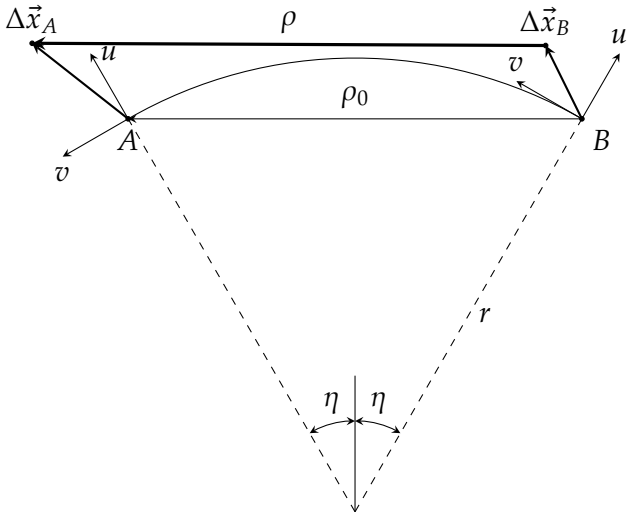

Figure 2.2: Collinear configuration

Application of the trigonometric identities:

$$\begin{aligned}\cos(a+b)+\cos(a-b) &= 2\cos a\cos b\\ \sin(a+b)+\sin(a-b) &= 2\sin a\cos b\end{aligned} \tag{2.46}$$

yields the following result for the radial difference:

$$\Delta u(t+\tau)+\Delta u(t-\tau) = 2\sum_{m=0}^{L}\sum_{k=-L}^{L}\left[A_{km}^{\Delta u}\cos(\dot{\psi}_{km}t)+B_{km}^{\Delta u}\sin(\dot{\psi}_{km}t)\right]\cos(\dot{\psi}_{km}\tau) \tag{2.47}$$

Similarly, the along-track contribution is:

$$\begin{aligned}&\Delta v(t+\tau)-\Delta v(t-\tau) =\\ &\quad=\sum_{m=0}^{L}\sum_{k=-L}^{L}A_{km}^{\Delta v}\left[\cos\dot{\psi}_{km}(t+\tau)-\cos\dot{\psi}_{km}(t-\tau)\right]+B_{km}^{\Delta v}\left[\sin\dot{\psi}_{km}(t+\tau)-\sin\dot{\psi}_{km}(t-\tau)\right]\end{aligned} \tag{2.48}$$

In this case, the following trigonometric identities are employed:

$$\begin{aligned}\cos(a+b)-\cos(a-b) &= -2\sin a\sin b\\ \sin(a+b)-\sin(a-b) &= 2\cos a\sin b\end{aligned} \tag{2.49}$$

$$\Delta v(t+\tau)-\Delta v(t-\tau) = 2\sum_{m=0}^{L}\sum_{k=-L}^{L}\left[-A_{km}^{\Delta v}\sin(\dot{\psi}_{km}t)+B_{km}^{\Delta v}\cos(\dot{\psi}_{km}t)\right]\sin(\dot{\psi}_{km}\tau) \tag{2.50}$$

Lastly, the range observation is developed as a lumped Fourier series.

$$\Delta p(t) = \sum_{m=0}^{L}\sum_{k=-L}^{L}A_{km}^{\Delta\rho}\cos(\dot{\psi}_{km}t)+B_{km}^{\Delta\rho}\sin(\dot{\psi}_{km}t) \tag{2.51}$$

$$\begin{bmatrix}A_{km}^{\Delta\rho}\\ B_{km}^{\Delta\rho}\end{bmatrix} = 2\begin{bmatrix}A_{km}^{\Delta u} & B_{km}^{\Delta v}\\ B_{km}^{\Delta u} & -A_{km}^{\Delta v}\end{bmatrix}\begin{bmatrix}\cos(\dot{\psi}_{km}\tau)\sin\eta\\ \sin(\dot{\psi}_{km}\tau)\cos\eta\end{bmatrix} \tag{2.52}$$

Substitution provides the final expression for the Fourier coefficients of the range.

$$\begin{bmatrix} A_{km}^{\Delta\rho} \\ B_{km}^{\Delta\rho} \end{bmatrix} = 2 \sum_{l=l_{min},2}^{L} \frac{\mu}{r^2} \left(\frac{a_e}{r}\right)^l F_{lmk} \alpha_{lmk} \begin{bmatrix} \tilde{C}_{lm} \\ \tilde{S}_{lm} \end{bmatrix}$$

$$\alpha_{lmk} = \frac{\left[-(l+1)\dot{\psi}_{km} + 2nk\right] \dot{\psi}_{km} \cos\left(\dot{\psi}_{km}\tau\right) \sin\eta + \left[2(l+1)n\dot{\psi}_{km} - k(3n^2 + \dot{\psi}_{km}^2)\right] \sin\left(\dot{\psi}_{km}\tau\right) \cos\eta}{\dot{\psi}_{km}^2 (n^2 - \dot{\psi}_{km}^2)} \tag{2.53}$$

It is convenient to express α_{lmk} in terms of the normalized frequencies $\beta_{km} = \frac{\dot{\psi}}{n}$ and the angular separation $\eta = n\tau$.

$$\alpha_{lmk} = \frac{\left[-(l+1)\beta_{km} + 2k\right] \beta_{km} \cos\left(\beta_{km}\eta\right) \sin\eta + \left[2(l+1)\beta_{km} - k(3 + \beta_{km}^2)\right] \sin\left(\beta_{km}\eta\right) \cos\eta}{n^2 \beta_{km}^2 (1 - \beta_{km}^2)} \tag{2.54}$$

This consists of the lumped coefficient observation for the GRACE observation equations.

2.6.1. Acceleration transfer functions

Apart from the intersatellite range observations in terms of the spherical harmonics coefficients, it is also interesting to define the transfer function from the acceleration of every satellite to the intersatellite range. As already discussed, only along-track and radial contributions are relevant for the first-order approximation. For this purpose, let's first write the transfer functions from the along-track and radial acceleration observations to the respective displacements, as described by the Hill non-resonant solutions in Eq. (2.34).

$$\begin{bmatrix} A_{km}^{\Delta u} \\ B_{km}^{\Delta u} \end{bmatrix} = \frac{1}{\dot{\psi}_{km}(n^2 - \dot{\psi}_{km})} \begin{bmatrix} A_{km}^{u} & -B_{km}^{v} \\ B_{km}^{u} & A_{km}^{v} \end{bmatrix} \begin{bmatrix} \dot{\psi}_{km} \\ 2n \end{bmatrix} \tag{2.55}$$

$$\begin{bmatrix} A_{km}^{\Delta v} \\ B_{km}^{\Delta v} \end{bmatrix} = \frac{1}{\dot{\psi}_{km}^2(n^2 - \dot{\psi}_{km})} \begin{bmatrix} B_{km}^{u} & A_{km}^{v} \\ -A_{km}^{u} & B_{km}^{v} \end{bmatrix} \begin{bmatrix} 2n\dot{\psi}_{km} \\ 3n^2 + \dot{\psi}_{km}^2 \end{bmatrix} \tag{2.56}$$

Next, the transfer function from the radial and along-track acceleration of the leading satellite is developed.

$$\Delta\rho(t) = \Delta v_A \cos\eta + \Delta u_A \sin\eta = \Delta v(t+\tau)\cos\eta + \Delta u(t+\tau)\sin\eta \tag{2.57}$$

$$\Delta u(t+\tau) = \sum_{m=0}^{L} \sum_{k=-L}^{L} A_{km}^{\Delta u} \cos\dot{\psi}_{km}(t+\tau) + B_{km}^{\Delta u} \sin\dot{\psi}_{km}(t+\tau) \tag{2.58}$$

$$\Delta v(t+\tau) = \sum_{m=0}^{L} \sum_{k=-L}^{L} A_{km}^{\Delta v} \cos\dot{\psi}_{km}(t+\tau) + B_{km}^{\Delta v} \sin\dot{\psi}_{km}(t+\tau) \tag{2.59}$$

This can be reformulated without a phase shift, defining $\Delta\psi = \dot{\psi}_{km}\tau$ and applying the initial phase angle rotation. Algebraic manipulation leads to:

$$\Delta\rho(t) = \sum_{m=0}^{L} \sum_{m=-L}^{L} A_{km}^{\Delta\rho} \cos\dot{\psi}_{km}t + B_{km}^{\Delta\rho} \sin\dot{\psi}_{km}t \tag{2.60}$$

$$\begin{bmatrix} A_{km}^{\Delta\rho} \\ B_{km}^{\Delta\rho} \end{bmatrix}_{u_A,v_A} = \begin{bmatrix} \cos\dot{\psi}_{km}\tau & \sin\dot{\psi}_{km}\tau \\ -\sin\dot{\psi}_{km}\tau & \cos\dot{\psi}_{km}\tau \end{bmatrix} \begin{bmatrix} A_{km}^{\Delta u} & A_{km}^{\Delta v} \\ B_{km}^{\Delta u} & B_{km}^{\Delta v} \end{bmatrix} \begin{bmatrix} \sin\eta \\ \cos\eta \end{bmatrix} \tag{2.61}$$

Accounting for only the radial lumped coefficients contribution to the displacement, i.e. A_{km}^{u}, B_{km}^{u}, the transfer function from the leading satellite radial acceleration to the collinear range is derived. The lower sign corresponds to the trailing satellite formulation. Note that there exist two differences in the trailing satellite formulation as compared to the leading satellite. First, the sign for the along-track contribution changes in Eq. (2.44). Moreover, the initial phase angle is the opposite.

$$\begin{bmatrix} A_{km}^{\Delta\rho} \\ B_{km}^{\Delta\rho} \end{bmatrix}_{u} = \frac{1}{\dot{\psi}_{km}(n^2-\dot{\psi}_{km}^2)} \begin{bmatrix} \cos\dot{\psi}_{km}\tau & \pm\sin\dot{\psi}_{km}\tau \\ \mp\sin\dot{\psi}_{km}\tau & \cos\dot{\psi}_{km}\tau \end{bmatrix} \begin{bmatrix} \dot{\psi}_{km}\sin\eta & 2n\cos\eta \\ -2n\cos\eta & \dot{\psi}_{km}\sin\eta \end{bmatrix} \begin{bmatrix} A_{km}^{u} \\ B_{km}^{u} \end{bmatrix} \tag{2.62}$$

Similarly, for the along-track acceleration:

$$\begin{bmatrix} A_{km}^{\Delta\rho} \\ B_{km}^{\Delta\rho} \end{bmatrix}_{v} = \frac{\pm 1}{\dot{\psi}_{km}(n^2-\dot{\psi}_{km}^2)} \begin{bmatrix} \cos\dot{\psi}_{km}\tau & \pm\sin\dot{\psi}_{km}\tau \\ \mp\sin\dot{\psi}_{km}\tau & \cos\dot{\psi}_{km}\tau \end{bmatrix} \begin{bmatrix} (3n^2+\dot{\psi}_{km}^2)\cos\eta & -\dot{\psi}_{km}^2\sin\eta \\ \dot{\psi}_{km}^2\sin\eta & (3n^2+\dot{\psi}_{km}^2)\cos\eta \end{bmatrix} \begin{bmatrix} A_{km}^{v} \\ B_{km}^{v} \end{bmatrix} \tag{2.63}$$

3

Least squares gravity field error analysis

In the previous chapter, linear observation models have been developed for the lumped coefficients as a function of the spherical harmonics coefficients. The linear system then reads as:

$$\bar{y} = A\bar{x} + \bar{\epsilon} \tag{3.1}$$

with $\bar{y}$ the observation vector, $\bar{x}$ the parameter vector, A the design matrix and $\bar{\epsilon}$ the vector of residuals.

Given a set of observations, the objective is to fit the parameters such that the following cost function is minimized.

$$J = \bar{\epsilon}^T \bar{\epsilon} \tag{3.2}$$

This consists of the unweighted least squares method. However, if the observations have different noise levels, it is reasonable to give more importance to those observations with less noise. For this purpose, the observation covariance matrix is introduced into the cost function as:

$$J = \bar{\epsilon}^T P_{yy}^{-1} \bar{\epsilon} \tag{3.3}$$

where matrix $W = P_{yy}^{-1}$ is called the weight matrix. Minimization of this cost function yields the weighted least squares method. The solution becomes:

$$\hat{x} = \left(A^T P_{yy}^{-1} A\right)^{-1} A^T P_{yy}^{-1} \bar{y} \tag{3.4}$$

where matrix $N = A^T P_{yy}^{-1} A$ is the normal matrix.

3.1. Least squares error analysis

The least squares solution provides an estimation for the parameter vector from a set of observations. Furthermore, it is possible to determine the error of the estimated parameter vector. This is the main objective of the analytical model. The parameter covariance is computed by inversion of the normal matrix.

$$P_{xx} = (A^T P_{yy}^{-1} A)^{-1} \tag{3.5}$$

In this way, given an observation covariance for the lumped coefficients A_{km}, B_{km}, the predicted error for the SH coefficients can be computed from the parameter covariance matrix. Section 3.6 delves into the definition of the observation covariance from different ranging instruments. Moreover, the influence of other error sources is discussed in 3.7.

3.2. Blocking the linear system

From the final observation expressions, it follows that coefficients $\tilde{C}_{lm}, \tilde{S}_{lm}$ can be solved independently for a given order m (Colombo, 1984). If the global indexing of the parameters in the design matrix gathers coefficients of the same order together and uncorrelated observations are assumed, i.e., P_{yy} diagonal, the resulting normal matrix is a block-diagonal matrix (see Figure 3.1).

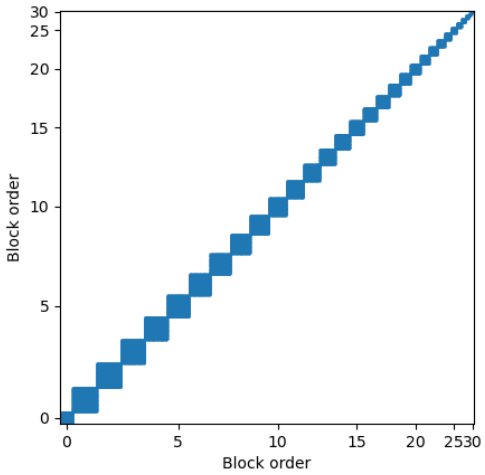

Figure 3.1: Block diagonal normal matrix

Time complexity of the full system is $O(x^3)$ with $x = (2L + 1) \cdot (L + 1)$ the size of the normal matrix, i.e., $O(L^6)$ in terms of the cut-off degree. The time complexity of the block-diagonal system is $\sum_{m=0}^{L} O(x_m^3)$ with $x_m = (2 - \delta_{0m}) \cdot (L + 1 - m)$ the number of parameters per block, with δ_{0m} the Kronecker delta. As a result, the block-diagonal system time complexity is $O(L^4)$, which consists of a significant improvement.

3.3. The repeating ground track constraint

As stated by Sneeuw (2000), if the orbit is not in a repeating ground track, the full torus formed by (ω_o, ω_e) is covered in an infinite time. However, if the ground track is repeating, this does not occur. This condition is paramount for the validity of the model, since the lumped expressions assume the periodicity of the orbit in the Earth-fixed frame. While one might think that the repeating ground track condition is implicitly defined in the orbit radius, it is necessary to also match some non-resonant frequencies when building the design matrix. A repeating ground track is defined by two parameters: the number of revolutions N_r and the nodal days N_d. A constraint can be introduced by defining integer frequencies, which can be conceived as cycles per repeating ground track repeatability period:

$$\gamma_{km} = N_r \beta_{km} = N_r (k + m \frac{\dot{w}_e}{\dot{w}_o}) = k N_r - m N_d \tag{3.6}$$

The negative sign arises due to the fact that $\dot{\omega}_e < 0$ (see section 2.2) and that N_d is defined positive.

Schrama (1990) points out that there exists frequency overlap when:

$$\dot{\psi}_{k_1 m_1} = -\dot{\psi}_{k_2 m_2} \tag{3.7}$$

In this work, this is called antisymmetric overlap. Employing integer frequencies introducing the repeating ground track condition, it follows that:

$$k_1 N_r - m_1 N_d = -k_2 N_r + m_2 N_d \implies \frac{k_2 + k_1}{m_2 + m_1} = \frac{N_d}{N_r} \tag{3.8}$$

Given that $N_r \gg N_d$, the condition on the denominator is more restrictive, and there is overlap if the following holds:

$$m_2 + m_1 = N_r \tag{3.9}$$

For an arbitrary cut-off degree L, the maximum value of the left-hand side is $m_2 + m_1 = 2L$, and the condition for overlapping can be written as $L = N_r/2$ (Schrama, 1990). This is known as the Colombo-Nyquist rule for satellite gravimetry and defines a maximum resolvable spherical harmonics degree for a satellite in a near-polar circular orbit (Colombo, 1984).

However, Visser et al. (2012) pointed out that the Colombo-Nyquist rule only indicates the longitude homogeneity of the quality of the recovered gravity field. In fact, the maximum resolvable degree is $L = kN_r + 1$, with k the number of observations (Visser et al., 2012).

This follows from the condition that there is a degenerate overlap.

$$\dot{\psi}_{k_1 m_1} = \dot{\psi}_{k_2 m_2} \tag{3.10}$$

Analogously, this leads to:

$$k_1 N_r - m_1 N_d = k_2 N_r - m_2 N_d \implies \frac{k_2 - k_1}{m_2 - m_1} = \frac{N_d}{N_r} \tag{3.11}$$

In this case, the maximum value of the denominator is $m_2 - m_1 = L$, and the same result as Visser et al. (2012) is obtained: $L = N_r$.

The exact reason why the antisymmetric overlap condition does not imply the ill-posedness of the linear system, while the degenerate overlap condition does, needs further investigation. A plausible explanation is the fact that the new set of lumped coefficients is not linearly independent of each other when there exists degenerate overlap:

$$\begin{bmatrix} A_{k_1 m_1'} \\ B_{k_1 m_1'} \end{bmatrix} = \begin{bmatrix} A_{k_1 m_1} \\ B_{k_1 m_1} \end{bmatrix} + \begin{bmatrix} A_{k_2 m_2} \\ B_{k_2 m_2} \end{bmatrix} \tag{3.12}$$

In contrast, the antisymmetric overlap results in the following combined lumped coefficients:

$$\begin{bmatrix} A_{k_1 m_1'} \\ B_{k_1 m_1'} \end{bmatrix} = \begin{bmatrix} A_{k_1 m_1} \\ B_{k_1 m_1} \end{bmatrix} + \begin{bmatrix} A_{k_2 m_2} \\ -B_{k_2 m_2} \end{bmatrix} \tag{3.13}$$

where the negative sign stems from $\sin \psi_{k_1 m_1} = -\sin -\dot{\psi}_{k_2 m_2}$ and breaks the linear dependency between both expressions.

One important consequence of the frequency overlap is that the normal matrix is no longer block-diagonal because there exists a correlation between certain order blocks, those that can be expressed with the same m_0. They can be represented as an interleaved arithmetic sequence:

$$m = (-1)^n \cdot m_0 + N_r \left\lceil \frac{n}{2} \right\rceil \tag{3.14}$$

where $m_0 = 0, 1, \ldots, N_r/2$ represent the different blocks formed and $n = 0, 1, 2, \ldots$ as long as $m \leq L$. As a result, the block-diagonal normal matrix becomes a kite matrix (Visser et al., 2012). However, the system can still be solved in a block-wise approach for every base order m_0.

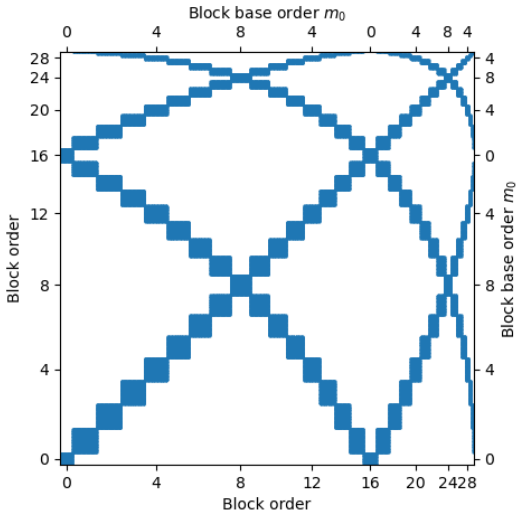

Figure 3.2: Block-kite normal matrix with N_r/N_d=16/1 repeating ground track constraint

3.4. Constrained solution

As a consequence of the repeating ground track, coefficients of different orders show certain correlation. For cut-off degrees L larger than the number of revolutions of the repeating ground track, the system becomes ill-posed, i.e. $L > N_r$.

This can be circumvented constraining the least squares problem. A typical approach is to add a-priori information about the parameters as a constraint equation. The constrained system of equations then becomes:

$$\begin{bmatrix} \bar{y} \\ \bar{c} \end{bmatrix} = \begin{bmatrix} A \\ B \end{bmatrix} \bar{x} + \begin{bmatrix} \bar{\epsilon}_y \\ \bar{\epsilon}_c \end{bmatrix} \tag{3.15}$$

The constrained least squares method accounts for the constraints in the cost function accordingly:

$$J = \bar{\epsilon}_y^T P_{yy}^{-1} \bar{\epsilon} + \bar{\epsilon}_c^T P_{cc}^{-1} \bar{\epsilon}_c \tag{3.16}$$

Minimization of the cost function yields the solution to the constrained normal equations.

$$\hat{x} = \left(A_T P_{yy}^{-1} A + B_T P_{cc}^{-1} B \right)^{-1} \left(A_T P_{yy}^{-1} \bar{y} + B_T P_{cc}^{-1} \bar{c} \right) \tag{3.17}$$

The parameter covariance is also influenced by the constraint covariance.

$$P_{xx} = (A^T P_{yy}^{-1} A + B^T P_{cc}^{-1} B)^{-1} \tag{3.18}$$

For the estimation of the Stokes coefficients, only covariance information is considered. This assumes that $B = I$ and $\bar{c} = 0$ while P_{cc} provides some a-priori information of the parameters. The selection of the parameter a-priori information is not trivial. Ideally, unconstrained solutions are desirable. However, introducing constraints is not necessarily detrimental, but the nature of the constraints and their consequences must always be accounted for. Two alternative approaches have been considered in this work.

3.4.1. Kaula's constraint

The first and simplest approach consists of introducing Kaula's constraint (Kaula, 1966). It defines an empirical degree power law for the variance of the spherical harmonics coefficients from autocovariance analysis of gravimetry (Kaula, 1959; Kaula, 1963).

$$\sigma\left\{\bar{C}_{lm}, \bar{S}_{lm}\right\} \approx \frac{10^{-5}}{l^2} \tag{3.19}$$

Note that the coefficients with the same degree are therefore assumed to have the same variance. This follows from the isotropic assumption of invariant variance under rotation around the Earth's axis (Kaula, 1963).

Eq. (3.19) applies to Earth's gravity field. Alternative empirical rules exist for other planetary bodies. Generally, Kaula's rule of thumb describes that the gravity field power decreases for shorter wavelengths. While this can be generally accepted, several studies have shown that, for higher degrees, topography takes over, and the degree variance spectrum can deviate from Kaula's rule (e.g. Broquet and Wieczorek, 2019).

3.4.2. The AOD1B data product

For temporal gravity field modelling, it is more reasonable to include a-priori information based on the expected variability of the temporal gravity field within the data accumulation time window of the solution. Tidal variations are well-known and can be determined with sufficient accuracy (e.g. Sulzbach et al., 2022). However, the behaviour of the non-tidal component is difficult to model. For this reason, the AOD1B is employed as a constraint to the normal equations (Shihora et al., 2022). It makes use of data from the operational Numerical Weather Prediction (NWP) model of the European Centre for Medium-Range Weather Forecasts (ECMWF) along with ocean bottom pressure derived from simulation with the ocean general circulation model MPIOM (Jungclaus et al., 2013). AOD1B provides the gravity field anomalies due to the mass redistributions predicted from those numerical models. In this way, AOD1B is taken as a correction to GRACE observation data (L1B) to mitigate temporal aliasing into the monthly solutions (e.g., Mayer-Gürr et al., 2018).

The limitations of the AOD1B product must be considered. Firstly, it only provides a-priori knowledge. Besides this, part of the non-tidal signal is unmodelled, e.g., the contribution of continental hydrology. However, AOD1B explicitly provides estimations of the atmosphere contribution, thus allowing for better separation of continental mass anomalies.

The German Research Centre for Geosciences (GFZ) provides forecasts for the AOD1B product that might be used for real-time gravity field modelling. However, since this work aims to estimate gravity field error and whether the gravity signal can be well captured or not, another approach is employed. AOD1B data every 3h since 1975 is available. The idea here presented consists of analysing the data variability to define an a-priori parameter covariance. For this purpose, an EOF analysis has been conducted to remove noise and compress the dataset. This technique was first devised by Pearson (1901) and has become popular for studying weather

patterns after the work of E. N. Lorenz (1956). Although the EOF method is not based on any physical properties, it can unveil insights into the dataset by identifying the dominant modes.

AOD1B directly provides Stokes coefficients data. While the EOF is typically employed to analyse spatial and temporal patterns in a dataset, studies have demonstrated that it can be applied in the SH domain (Wouters & Schrama, 2007). The AOD1B data can be converted into an $m \times n$ data matrix such that every column is associated with different times and every row is associated to a certain spherical harmonics coefficient, or alternatively, a certain spatial location.

$$A = \begin{bmatrix} x_1(t_1) & x_1(t_2) & \cdots & x_1(t_n) \\ x_2(t_1) & x_2(t_2) & \cdots & x_2(t_n) \\ \vdots & \vdots & \ddots & \vdots \\ x_m(t_1) & x_m(t_2) & \cdots & x_m(t_n) \end{bmatrix} \tag{3.20}$$

Typically, the data matrix is first detrended, i.e., the mean over time of the spatial behaviour is removed. Similarly, normalization might be applied. This is especially effective when working in the SH domain. The EOF analysis then allows to identify the spatial patterns that contribute the most to the unit variance of the data matrix. For this purpose, a singular value decomposition is applied.

$$A = U\Lambda V^T \tag{3.21}$$

where U and V are orthogonal matrices whose columns are left and right singular vectors of A, respectively, and Λ is a non-square diagonal matrix with non-negative singular values $\sigma_i = \lambda_i^2$ in descending order. Matrix U has size $m \times m$ and contains the spatial patterns as the left singular vectors u_i, while matrix V has size $n \times n$ and contains the time patterns in the right singular vectors v_j. Hence, the following holds:

$$Av_i = \sigma_i u_i \tag{3.22}$$

$$A^T u_i = \sigma_i v_i \tag{3.23}$$

The variance contribution of every mode can be computed as follows:

$$\epsilon = \frac{\sigma_i^2}{\sum_i \sigma_i^2} \tag{3.24}$$

Typically, the first singular values contribute to the majority of the variance. In this way, the data matrix can be compressed while smoothing out data noise. A reduced data matrix that only accounts for the first k modes can be written as follows:

$$A_r = U \begin{bmatrix} \sigma_1 & 0 & \cdots & 0 & 0 & \cdots & \\ 0 & \sigma_2 & \cdots & 0 & 0 & \cdots & 0 \\ \vdots & \vdots & \ddots & \vdots & \vdots & & \vdots \\ 0 & 0 & \cdots & \sigma_k & 0 & \cdots & 0 \\ 0 & 0 & \cdots & 0 & 0 & \cdots & 0 \\ \vdots & \vdots & & \vdots & \vdots & \ddots & \vdots \\ 0 & 0 & \cdots & 0 & 0 & \cdots & 0 \end{bmatrix} V^T \tag{3.25}$$

A reduced data matrix also relaxes covariance computation:

$$\frac{1}{n-1}AA^T = \frac{1}{n-1}U\Lambda V^T(U\Lambda V^T)^T = \frac{1}{n-1}U\Lambda V V^T \Lambda U^T = \frac{1}{n-1}U\Lambda^2 U^T \tag{3.26}$$

Analogous development for the time covariance $A^T A$ demonstrates that both covariances share eigenvectors. Typically, variance analysis shows that a few eigenvectors dominate covariance directions.

A spatial standard deviation map of the i-th mode can then be computed by projecting the data matrix into the associated temporal mode v_i or, alternatively, in the following way.

$$\frac{1}{\sqrt{n-1}}\sigma_i u_i \tag{3.27}$$

The principal component time series associated with the i-th eigenvector can be computed by applying Eq. (3.23). This indicates how similar the i-th spatial mode is to the dataset at any instant of time.

Next, the EOF analysis of the AOD1B data is presented. First, the cumulative variance contribution to AOD1B data from the first 1000 modes is depicted in the figure below.

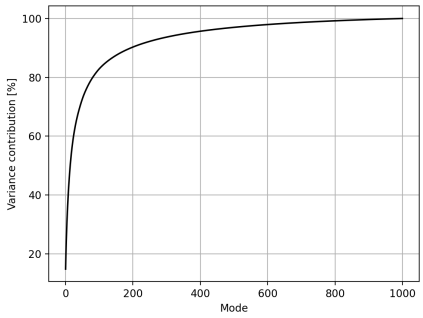

Figure 3.3: AOD1B EOF variance analysis of the first 1000 modes

The first 200 modes contain around 90% of the variance of the SH coefficients. They have been selected to define the reduced data matrix. Certain physical phenomena can be inferred from analysis of the first modes. For this purpose, the SH coefficients patterns are projected into EWH.

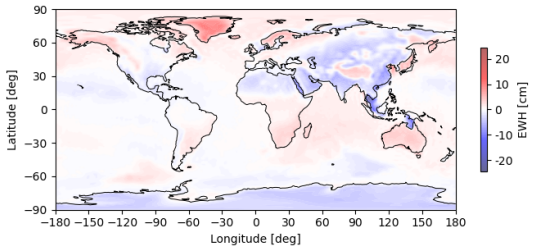

(a) 1st mode: spatial pattern EWH synthesis

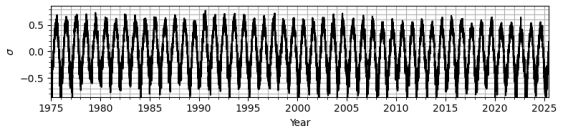

(b) 1st mode: time series

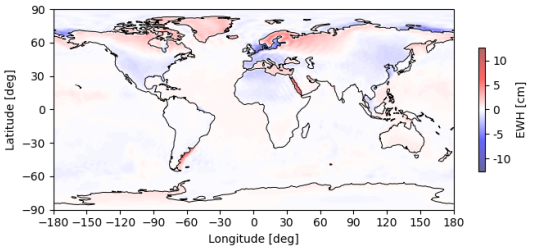

(c) 2nd mode: spatial pattern EWH synthesis

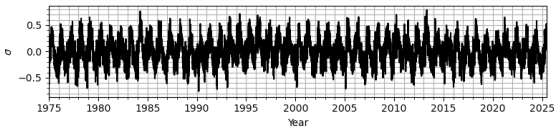

(d) 2nd mode: time series

Figure 3.4: AOD1B contributions of the dominant modes

For example, the first mode reveals large contributions to the gravity field variance in Greenland. Sea level variations in the Gulf of Thailand (Wouters & Chambers, 2010) and the Gulf of

Carpentaria (Tregoning et al., 2008) are also comparatively significant. These phenomena are dominated by an annual periodic component, as analysis of the associated temporal eigenvector revealed. The second mode also shows an annual pattern along with much more variability at lower timescales. Among the spatial patterns, sea level variability in the Mar del Plata, Red Sea or North Sea, among others, stand out along with the contribution of the Scandinavian Peninsula.

The reduced data matrix has been employed to compute the a-priori standard deviations of the spherical harmonics coefficients for different integration times. The figure below illustrates the standard deviation for every SH coefficient for an integration time of 3 hours.

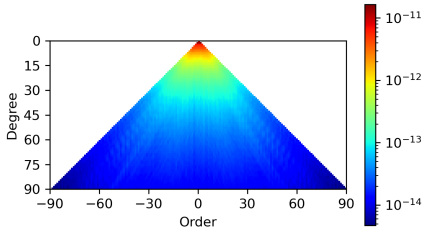

Figure 3.5: Spherical harmonics coefficients a-priori standard deviation from AOD1B data

As the figure shows, a-priori standard deviations do vary for coefficients of the same degree, indicating that the isotropy assumption is no longer implicit in the a-priori information definition. Furthermore, the magnitude of the standard deviations is significantly lower than that of Kaula's rule. This results in a more stringent constraint when considering AOD1B variability to solve the parameter covariance. In Figure 3.6, an overview of the amplitude in the spatial spectrum is compared through RMS per coefficient per degree for a static gravity field, Kaula's power rule, and AOD1B variability for different integration times.

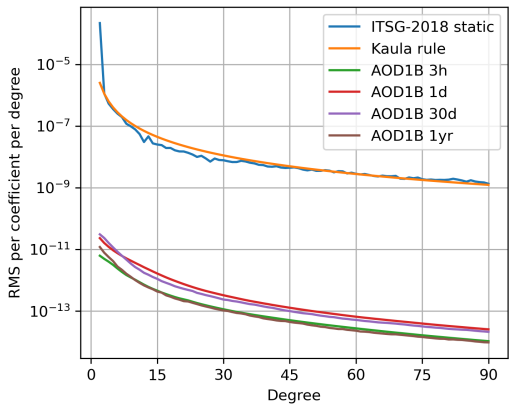

Figure 3.6: RMS per coefficient per degree comparison

A remarkable result is observed in the figure above. Lower integration times, such as 3 hours or 1 day, result in higher variability of the mean gravity field. Synthesis into EWH indicates that this variability mainly stems from non-tidal behaviours near coastal areas (see Figure 3.7). Note, for example, Mar del Plata, North Sea, Bering Sea, or Hudson Bay. The origin of these phenomena requires further investigation. Some studies have pointed out the limitations of tidal models over the continental shelf (e.g. Chambers and Willis, 2010), and others have

emphasized that inaccuracies of ocean tide models alias into gravity field solutions (e.g. Visser et al., 2010).

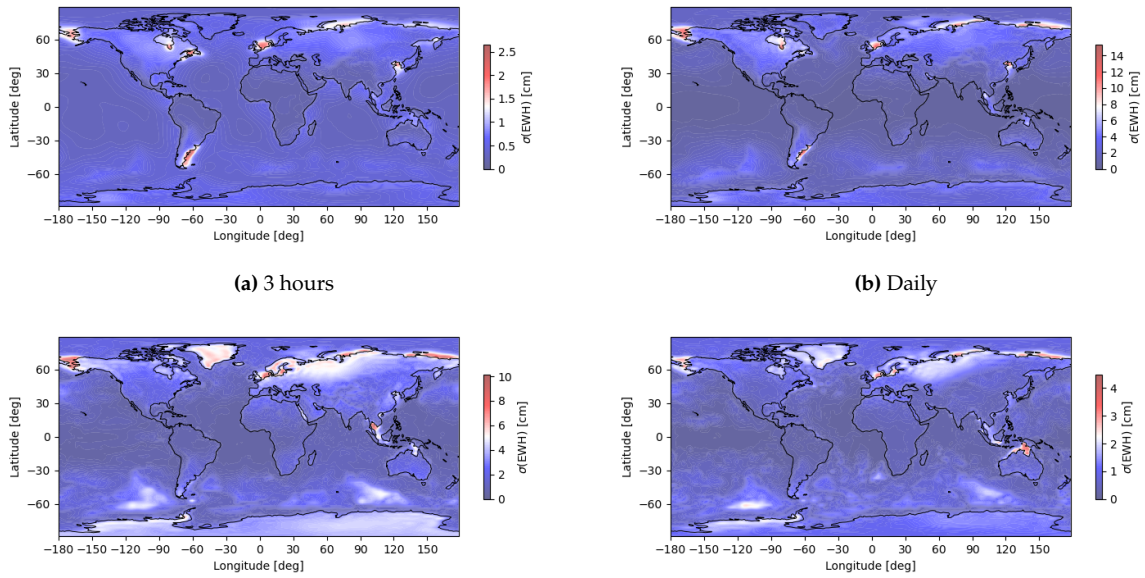

(a) 3 hours

(b) Daily

(c) Monthly

(d) Annual

Figure 3.7: AOD1B variability standard deviation for different timescales

3.5. Combination of multiple observations

At the beginning of the chapter, the observation equation was introduced for a single set of lumped coefficients. However, it might be interesting to combine multiple observations. This is as simple as redefining a combined design matrix, vertically stacking the individual design matrices of each observation type. For instance, the 3D GPS position observation equations could be written as follows:

$$\begin{bmatrix} \Delta\bar{u} \\ \Delta\bar{v} \\ \Delta\bar{w} \end{bmatrix} = \begin{bmatrix} A_{\Delta u} \\ A_{\Delta v} \\ A_{\Delta w} \end{bmatrix} \bar{x} + \begin{bmatrix} \bar{\epsilon}_{\Delta u} \\ \bar{\epsilon}_{\Delta v} \\ \bar{\epsilon}_{\Delta w} \end{bmatrix} \tag{3.28}$$

For the error analysis, the parameter covariance propagation can be accomplished through the definition of a combined observation covariance, assuming no correlation between the observations:

$$P_{yy} = \begin{bmatrix} P_{uu} & 0 & 0 \\ 0 & P_{vv} & 0 \\ 0 & 0 & P_{ww} \end{bmatrix} \tag{3.29}$$

Another application of the combination of observations is modelling constellations. An interesting example is the Bender configuration, which consists of two collinear formations, like GRACE, where the second satellite pair is placed at a lower inclination I_2 to mitigate equatorial errors (Bender et al., 2008). In this way, the combined observation equations read as:

$$\begin{bmatrix} \Delta\rho_1 \\ \Delta\rho_2 \end{bmatrix} = \begin{bmatrix} A_{\Delta\rho_1} \\ A_{\Delta\rho_2} \end{bmatrix} \bar{x} + \begin{bmatrix} \epsilon_{\Delta\rho_1} \\ \epsilon_{\Delta\rho_2} \end{bmatrix} \tag{3.30}$$

Similarly, assuming that the range observations from the two satellite pairs are uncorrelated, the combined observation covariance is formed through diagonal stacking:

$$P_{yy} = \begin{bmatrix} P_{\rho_1\rho_1} & 0 \\ 0 & P_{\rho_2\rho_2} \end{bmatrix} \tag{3.31}$$

An arbitrary number of n observations can be combined as follows:

$$\begin{bmatrix} \bar{y}_0 \\ \bar{y}_1 \\ \vdots \\ \bar{y}_n \end{bmatrix} = \begin{bmatrix} A_0 \\ A_1 \\ \vdots \\ A_n \end{bmatrix} \bar{x} + \begin{bmatrix} \bar{\epsilon}_0 \\ \bar{\epsilon}_1 \\ \vdots \\ \bar{\epsilon}_n \end{bmatrix} \tag{3.32}$$

and the combined covariance, assuming uncorrelated observations, takes the form below.

$$P_{yy} = \begin{bmatrix} P_{y_0y_0} & 0 & \cdots & 0 \\ 0 & P_{y_1y_1} & \cdots & 0 \\ \vdots & \vdots & \ddots & \vdots \\ 0 & 0 & \cdots & P_{y_ny_n} \end{bmatrix} \tag{3.33}$$

To conclude, note that since the a-priori parameter information does not affect the observation covariance in any sense, it can be similarly employed in the constrained normal equations with the full observation covariance.

3.6. Power spectral density

Quantification of the error spectrum of intersatellite range observations is paramount to defining the observation covariance. For a microwave ranging system, the error is commonly dominated by the phase error $\phi(t)$ of the oscillator.

$$A(t) = A_0 \sin\left(2\pi f_0 t + \phi(t)\right) \tag{3.34}$$

Note that frequency and amplitude also show a certain error, although typically not as meaningful as the phase. As a result of the phase offset error, the instantaneous frequency deviates from the nominal. This is typically expressed in relative frequency error:

$$y(t) = \frac{1}{2\pi f_0} \frac{\partial \phi(t)}{\partial t} \tag{3.35}$$

A method to assess the stability of atomic oscillators is the Allan variance, which consists of the time-infinite average of the sample variance of two adjacent averages of $y(t)$, also called two-sample variance (Allan, 1966; Barnes et al., 1971).

$$\bar{y}_k = \frac{1}{\tau} \int_{t_k}^{t_k+\tau} y(t)\, dt \approx \frac{\phi(t_k + \tau) - \phi(t_k)}{2\pi f_0 \tau} \tag{3.36}$$

$$\sigma_y^2(\tau) = \frac{1}{2} \langle (\bar{y}_{k+1} - \bar{y}_k)^2 \rangle \tag{3.37}$$

Three different regimes can be observed in the frequency stability behaviour of an atomic oscillator (see Figure 3.8). The behaviour of each regime can be described by power laws $\sigma_y(\tau) = K\tau^\alpha$. Part I typically consists of white phase ($\alpha = -1$) or frequency ($\alpha = -3/2$) noise.

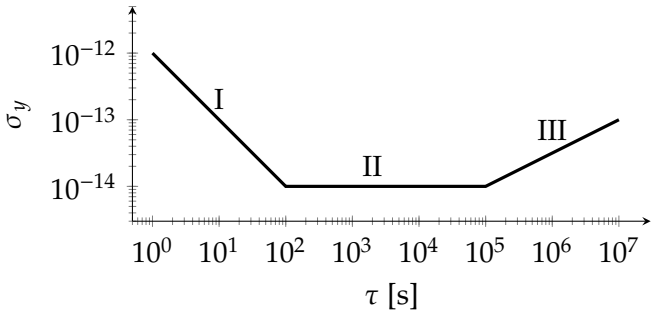

Figure 3.8: Typical frequency stability behaviour of an atomic oscillator (Hellwig, 1975).

Part II is called the Flicker floor and is characterized by a constant Allan deviation, i.e. $\alpha = 0$. For larger timescales, oscillators show a drift behaviour due to ageing described by $\alpha = 1$, although reliable determination is complex given the long timescales (Hellwig, 1975). For this work, only parts I and II of the spectrum are relevant since clock drift occurs at much longer timescales than the integration time of a gravity field solution.

Tests allow the definition of Allan variances, which can be related to Power Spectral Density (PSD) for the oscillators (Barnes et al., 1971). Subsequently, the oscillator noise can be transferred into noise PSD for the intersatellite range measurements. PSD indicates the power in an infinitesimal spectral band df. The square root of the PSD, the Amplitude Spectral Density (ASD), describes the amplitude of the noise for the infinitesimal spectral band. In this work, it is of interest to define the noise variance σ^2_{km} associated with the different orbital frequencies $\dot{\psi}_{km}$. While the orbital spectral lines are discrete, the error spectrum is continuous. For a given orbital frequency, all the neighbouring frequencies that fall within the frequency resolution limit Δf contribute to the associated power noise (Sneeuw, 2000). Integration over the frequency band results in the observation variance.

$$\sigma^2_{km} = \int_{f_{km}-\Delta f/2}^{f_{km}+\Delta f/2} S(f)\, df \approx S(f_{km})\Delta f \tag{3.38}$$

where $f_{km} = \dot{\psi}_{km}/2\pi$ is the frequency in Hz associated with a given angular frequency $\dot{\psi}_{km}$.

Kim (2000) derived the transfer function for the GRACE dual one-way ranging instrument. By means of a simulation-based approach, PSD for both range and range-rate measurements were computed. The analysis also accounted for other observation error sources, namely multipath effects, system noise and accelerometer errors. Accelerometer errors are discussed in section 3.7.1, as they are not pure errors associated with the ranging instrument. Along this work, other instrument error sources are assumed to be incorporated in the intersatellite ranging noise PSD.

For the sake of simplicity, GRACE/GRACE-FO ranging system noise will be modelled according to the mission requirements error spectrum as provided in Kornfeld et al. (2019). ASD formulations for the MWI and the LRI are defined.

$$A_\rho^{\mathrm{MWI}}(f) = 2.62 \cdot \sqrt{1 + \left(\frac{0.003}{f}\right)^2}\, \frac{\mu\mathrm{m}}{\sqrt{\mathrm{Hz}}} \tag{3.39}$$

$$A_\rho^{\mathrm{LRI}}(f) = 80 \cdot \sqrt{1 + \left(\frac{0.003}{f}\right)^2}\sqrt{1 + \left(\frac{0.01}{f}\right)^2}\, \frac{\mathrm{nm}}{\sqrt{\mathrm{Hz}}} \tag{3.40}$$

with f the frequency in Hz.

Future GRMs will, however, carry better or alternative ranging systems. NGGM/MAGIC mission will incorporate a LRI, technology demonstrated successfully in GRACE-FO with significant noise reduction at higher frequencies compared to microwave ranging (Abich et al., 2019). Technological advancements are expected to provide intersatellite ranging capabilities surpassing NGGM mission requirements. Nicklaus et al. (2020) define an ASD goal as follows.

$$A_{\rho}^{\mathrm{NGGM}}(f) = 10 \cdot \sqrt{1 + \left(\frac{0.001}{f}\right)^2} \, \frac{\mathrm{nm}}{\sqrt{\mathrm{Hz}}} \tag{3.41}$$

Figure 3.9 depicts the different ASD for the ranging system employed throughout this work. Note that GRACE-FO LRI outperforms the MWI at higher frequencies. Also, the expected improvement in NGGM is significant throughout the whole spectrum.

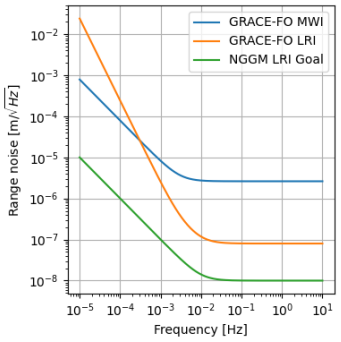

Figure 3.9: Noise amplitude spectral density for different ranging system instruments

3.7. The influence of orbital perturbations

The dynamic model employed to derive the analytical observation model only incorporated the perturbing potential into the acceleration terms. However, in reality, satellite dynamics are also driven by other perturbations. Atmospheric drag, solar radiation pressure, Earth radiation pressure, third-body perturbations, relativistic effects, or electromagnetic forces can deviate satellite motion from pure motion under Earth's gravity field. Some of these effects are negligible for gravity field modelling, while others shall be accurately modelled to remove their contribution to the intersatellite range spectrum. The contribution of third-body perturbations is well-known, whereas effects such as radiation pressure or aerodynamic forces are subject to high uncertainties.

3.7.1. Accelerometers

To circumvent the uncertainty in non-gravitational perturbations, GRACE/GRACE-FO carried three-axis SuperSTAR accelerometers whose test mass is placed in the centre of mass of each satellite (Touboul et al., 1999). Accelerometers measure the difference in acceleration between the casing and a proof mass. In this way, they do not detect gravitational accelerations because they are body forces. However, they do measure surface forces. In this way, non-gravitational perturbations can be removed within the accuracy capabilities of the accelerometers. These errors in the acceleration propagate into the intersatellite range observations.

Accelerometer noise ASD can be incorporated into the analytical observation model according

to the Hill equations' transfer functions and subsequent propagation of the transfer functions from displacements to intersatellite range. Cross-track accelerations do not contribute to first-order collinear intersatellite range observations. Therefore, only covariance information regarding radial and along-track accelerations is needed. Subsection 2.6.1 relates the lumped coefficients of the accelerations of the leading and trailing satellite to the range observation. For example, the contribution to the intersatellite range observation error of the leading satellite accelerometer error in the radial direction is defined below.

$$P_{yy}^{u_A} = H_{\Delta\rho,u_A} P_{u_A u_A} H_{\Delta\rho,u_A}^T \tag{3.42}$$

In this work, the GRACE-FO SuperSTAR-FO accelerometer ASD will be assumed to fulfil the mission requirements as presented by Christophe et al. (2015).

$$A_{\ddot{x}}^{\text{SuperSTAR-FO}}(f) = 10 \cdot \sqrt{1 + \left(\frac{f}{0.5}\right)^4 + \left(\frac{0.005}{f}\right)} \frac{\text{nm}}{\text{s}^2/\sqrt{\text{Hz}}} \tag{3.43}$$

Additionally, the new generation of accelerometers developed for future GRMs by Office National d'Études et de Recherches Aérospatiales (ONERA) will be employed throughout this work. Data has been adapted from Dalin et al. (2020), distributed under the Creative Commons Attribution 4.0 International License (CC BY 4.0). NGGM will make use of the MicroSTAR accelerometer (Christophe et al., 2018; Maquaire et al., 2025). Alternatively, the smaller, lighter, and more affordable CubSTAR accelerometer is potentially a suitable candidate for future constellation-based GRMs (Boulanger et al., 2025). According to the noise performance figures provided in Dalin et al. (2020), the following empirical ASD have been derived.

$$A_{\ddot{x}}^{\text{CubSTAR}} = 0.01 \cdot \sqrt{\left(\frac{0.1}{f}\right) + 1 + \left(\frac{f}{0.15}\right)^4} \frac{\text{nm}}{\text{s}^2/\sqrt{\text{Hz}}} \tag{3.44}$$

$$A_{\ddot{x}}^{\text{MicroSTAR}} = 0.02 \cdot \sqrt{\left(\frac{0.002}{f}\right) + 1 + \left(\frac{f}{0.1}\right)^4} \frac{\text{nm}}{\text{s}^2/\sqrt{\text{Hz}}} \tag{3.45}$$

Figure 3.10 compares the ASD of the three accelerometers considered.

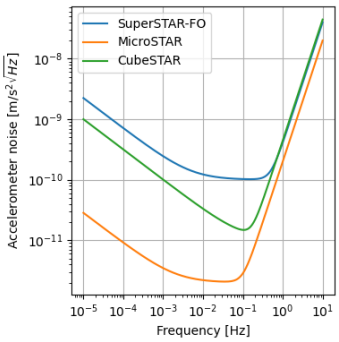

Figure 3.10: Noise amplitude spectral density for ONERA accelerometers. Data adapted from Dalin et al. (2020).

The total intersatellite range error, combining the contribution of the ranging instrument and the accelerometers, is described below for the three mission scenarios considered along this work.

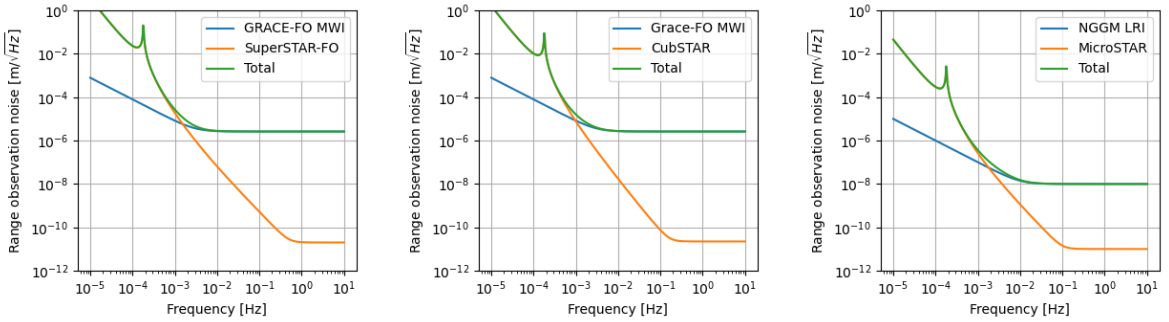

(a) GRACE-FO **(b)** CubeSat constellation **(c)** NGGM

Figure 3.11: Intersatellite range observation noise ASD: range instrument and accelerometer

While removing non-gravitational perturbations using accelerometer data has proven to be successful for GRACE/GRACE-FO, it has also shown some limitations. The main disadvantage lies in the accelerometers' saturation threshold. The dynamic range shall enable measurements of the full range of gravitational perturbations, which, in turn, compromises its resolution (Dionisio et al., 2018; Nguyen & Conklin, 2015). Moreover, accelerometer bias can negatively impact the attained solutions and requires careful calibration (Teixeira da Encarnação et al., 2020). Other post-processing efforts are needed, e.g., outlier detection (Darbeheshti et al., 2024). It would be ideal to be able to directly retrieve gravity field solutions from intersatellite range data. This specifically requires thorough consideration for future GRMs that intend to provide near-real-time gravity field solutions.

3.7.2. The drag-free satellite

A solution to improve the accelerometer resolution for future GRMs is the drag-free satellite concept. The idea is to employ a test mass that is not subjected to surface forces, such that it moves in continuous free fall under the influence of solely gravitational perturbations. In practice, this is not fully true, and residual accelerations remain. These accelerations can be measured and considered accordingly. The advantage lies in the fact that the residual accelerations are comparatively much smaller than the non-gravitational disturbances. Hence, the resolution of the accelerometers can be improved while maintaining the dynamic range within the saturation threshold. For example, this is the case for the MicroSTAR accelerometer, which has a significantly better resolution at the cost of a lower saturation threshold. Another positive aspect of the Drag-Free Attitude and Orbit Control System (DFAOCS) is that it allows flying at lower altitudes without compromising continuous intersatellite range measurements. The orbit altitude puts additional constraints on the propulsion system, such as a large thruster dynamic range (Smirnova et al., 2019), and compromises the mission lifetime (Wiese, Visser, & Nerem, 2011). Cesare et al. (2022) demonstrated that fine-pointing attitude control and full drag-free control are required to meet NGGM mission requirements and exploit the full spectral capabilities of the accelerometers. In this work, this performance will be assumed.

3.8. Frequency spectrum observability

Some mission scenarios might compromise the observability of the frequency spectrum. Certain orbital frequencies might not be observable, and they must be removed from the observation vector to properly estimate the gravity field error. Alternatively, repeated observation of the full spectrum leads to an enhanced determination of the lumped coefficients. The former

phenomena arise due to limited sampling rate, while the latter is associated with the gravity field solution time window.

3.8.1. Sampling time

The sampling time T_s of the observations defines an upper limit for the observable frequencies, according to the Nyquist-Shannon sampling theorem.

$$f_{max} = 2f_s = \frac{2}{T_s} \tag{3.46}$$

For a gravity field with a cut-off degree L, the maximum orbital frequency in LEO, assuming $\dot{\omega}_o \gg \dot{\omega}_e$, is approximated as:

$$\dot{\psi}_{km} \approx L\dot{\omega}_o \tag{3.47}$$

Typical values for the orbital frequency $\dot{\omega}_o$ in LEO are around 12-16 revolutions per day, i.e., in the order of 1 mHz. Therefore, considering typical cut-off degree values $L \sim 100$, maximum orbital frequencies can reach orders of 0.1 Hz. To achieve a Nyquist frequency of the same order of magnitude, instrument sampling rates in the order of a few seconds shall be enough to observe all the high orbital frequencies.

3.8.2. Gravity field solution time window

If the measurements' accumulation time T_o to generate a gravity field solution exceeds the repeatability period of the orbit T_r, the same ground track would be sampled multiple times. As a result, the frequency resolution would be improved. Eq. (3.38) indicates that the lumped coefficients' observation error can be assumed proportional to the frequency resolution. Therefore, given an observation time $T_o = nT_r$, the observation error variance is reduced by a factor n.

$$P_{yy,T_o} = \frac{1}{n} P_{yy,T_r} \quad \forall n > 0 \in \mathbb{N} \tag{3.48}$$

Given the linearity of the system, the unconstrained solution for the parameter covariance also displays this scaling factor.

$$P_{xx,T_o} = \left(A^T \left(\frac{1}{n} P_{yy,T_r} \right)^{-1} A \right)^{-1} = \frac{1}{n} \left(A^T P_{yy,T_r}^{-1} A \right)^{-1} = \frac{1}{n} P_{xx,T_r} \tag{3.49}$$

Optimally, the gravity field solution time window shall match the repeatability period of the selected orbit. However, the intrinsic orbital properties of the Low Earth Orbit (LEO) regime constrain this time window to a lower bound of roughly 1 day. An approach to circumvent this problem is to place multiple satellites in the same ground track such that the full ground track is covered in a shorter amount of time. In this work, this approach would be considered analogous to a single satellite mapping the full ground track. This is necessary because the analytical observation model imposes a periodicity condition in the observations that does not hold from the perspective of a single satellite. Orbiting over only part of the ground track compromises the frequency resolution and results in an overlap of the neighbouring frequencies.

$$\Delta f = \frac{1}{T_r} = f_0 \implies \Delta\gamma = 1 \tag{3.50}$$

This is essentially 1 cycle per repeating ground track. If the period of observation is limited to a fraction $1/\alpha$ of the repeating period, the frequency resolution degrades accordingly to α

cycles per repeating orbit:

$$\Delta f = \frac{1}{T} \implies \Delta\gamma = \alpha \tag{3.51}$$

As previously observed, all the orbital frequencies are integer frequencies when normalized by the number of revolutions. Therefore, an integer frequency resolution of 1 cycle per repeatability period is always required.

3.9. Commission and omission errors

The spherical harmonics representation of the gravity field is a model that has been formulated to model the real gravity field from the Stokes coefficients. To perfectly reproduce a gravity field, infinite SH coefficients would be required. Instead, the SH series expansion is typically truncated to a cut-off degree. As a result, there exists an error because those terms above the maximum degree are omitted, so-called omission error (Ince et al., 2019; Jekeli, 1979). Coefficients of a certain degree have an associated half-wavelength which defines the spatial resolution of the model:

$$\lambda_l = \frac{\pi a_e}{l} \tag{3.52}$$

Omission error arises due to the limited spatial resolution of the SH model.

The accuracy of a gravity field SH representation is also affected by the noise in the determined coefficients. This is the commission error, and it is typically the major error source (Ince et al., 2019). As discussed in chapter 1, estimated errors of higher degree coefficients are similar in magnitude to the actual estimated value of the coefficient, which indicates that commission error dominates the signal.

While the omission error reduces with increasing maximum degree due to fewer omitted terms, the commission error shows the opposite behaviour. Solution of the parameter covariance as described in section 3.1 provides an estimate of the commission error, but it does not account for the omission errors. For this purpose, Figure 3.12 shows a degree variance analysis of the AOD1B signal that is considered as a function of the cut-off degree.

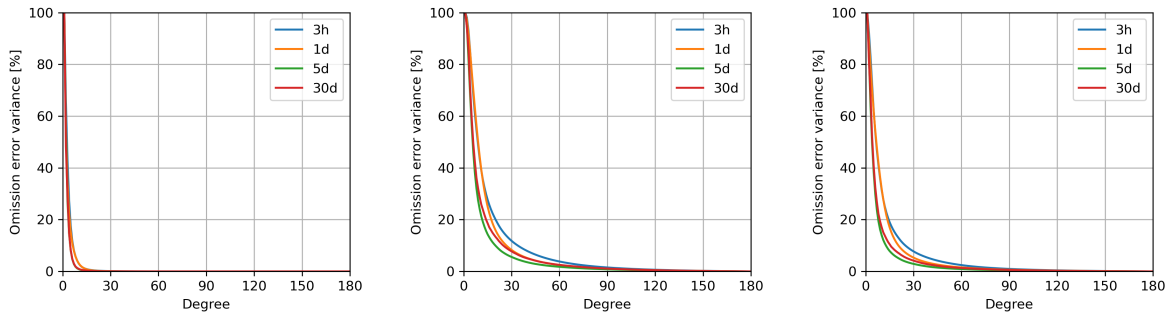

(a) Geoid heights **(b)** Gravity anomalies **(c)** EWH

Figure 3.12: AOD1B omission noise variance analysis

For geoid height variances, the power is concentrated in the lower degrees, with more than 90% of the variance described up to degree 10. However, both gravity anomalies and EWH show higher signal power at higher degrees. This is associated with degree common factors $(l-1)$ and $(2l+1)/(1+k'_l)$ respectively (see appendix C). As a result, higher cut-off degrees are required to accurately model these gravity field functionals. This also explains that the striping patterns observed in GRACE solutions (see section 1.1) arise for these two functionals, while they do not for geoid heights.

4

Numerical verification

In this chapter, the implementation of the analytical observation models presented in chapter 2 is verified and its validity to represent the observation spectrum is assessed by means of numerical simulations. For this purpose, the static gravity field model GOCO05c (Pail et al., 2016) is employed to fill the parameter vector $\bar{x}$. Based on the different design matrices, analytical spectral observations can be generated following the linear system presented in Eq. (3.1). Alongside, a numerical simulation is set up to generate the same spectral observations by means of integration of the equations of motion. Subsequently, Fourier analysis of the numerical range observations enables validation of the analytical observation model.

4.1. Numerical simulation setup

The numerical simulation will model the orbital dynamics under the influence of a spherical harmonics potential. For this purpose, an Encke propagator has been selected. Moreover, a Runge-Kutta-8 method is chosen for the integration of the equations of motion.

$$\frac{\partial \bar{x}}{\partial t} = f(\bar{x}, t) \tag{4.1}$$

The solutions of the equations of motion also consider the influence of the resonant terms. However, they are disregarded by the analytical model. As indicated by Colombo (1984), they result in a bow-tie pattern (see e.g., Fig. 4.4, Schrama, 1989). The bow-tie pattern consists of a long periodic modulation of resonant forcing and can be modelled through the resonant solution of the Hill equations (Schrama, 1989). Visser (2005) presented a spectral comparison based on Linear Perturbation Theory (LPT) formulated in orbital elements for intersatellite range-rate measurements between an analytical model and a numerical simulation, where the resonant terms are purposefully removed from the numerical simulation.

In this work, an alternative approach is presented, leveraging the periodicity of the lumped coefficient series. If a periodic perturbed orbit could be computed, secular variations arising due to resonant terms would be implicitly removed. In this way, the periodicity of the numerical observations is guaranteed, therefore avoiding spectral leakage of the resonant patterns along the frequency spectrum. This, however, does not guarantee a perfect match between the numerical and the analytical spectra. For instance, the existence of high-order perturbations is well-known (Brouwer, 1959), and their contribution to the frequency spectrum is not considered in the analytical observations. The line potential assumption as well as the linear dynamic model must not be disregarded.

4.2. Periodic orbits in full potentials

The computation of a perturbed repeating orbit in the Earth-fixed frame is not a trivial problem. It requires proper selection of an initial state such that the periodicity condition holds for a state in the Earth-Centered, Earth-Fixed (ECEF) frame.

$$\bar{x}(t+T) = \bar{x}(t) \tag{4.2}$$

with T the repeating ground track period.

To achieve this condition, a differential correction algorithm following the approach of Russell and Lara (2007) is employed. In this work, subtle modifications have been introduced. First, the propagation of the variational equations has been conducted in an Earth-Centered Inertial (ECI) frame to obtain a state transition matrix $\Phi(T, 0)$.

$$\frac{\partial}{\partial t}\Phi(t, t_0) = \frac{\partial f(t, \bar{x})}{\partial \bar{x}(t)}\Phi(t, t_0) \tag{4.3}$$

This requires rotation of the state transition matrix as follows:

$$\Phi^R(t, t_0) = T_{IR}(t)\Phi^I(t, t_0)T_{IR}(t_0) \tag{4.4}$$

where $T_{IR}(t)$, $T_{RI}(t)$ are rotation matrices for the full-state from and to the rotating frame, respectively, which read as follows:

$$T_{IR}(t) = \begin{bmatrix} M_{IR}(t) & 0_{3x3} \\ S_\omega & M_{IR}(t) \end{bmatrix} \tag{4.5}$$

$$T_{RI}(t) = \begin{bmatrix} M_{RI}(t) & 0_{3x3} \\ -S_\omega M_{RI}(t) & M_{RI}(t) \end{bmatrix} \tag{4.6}$$

with $M_{RI}^T(t) = M_{IR}(t) = R_3(\theta(t))$ a passive rotation matrix around the Earth rotation axis and $S_\omega = [\vec{\omega}]_\times$ a skew-symmetric angular velocity matrix describing Earth rotation:

$$S_\omega = \begin{bmatrix} 0 & -\omega_z & 0 \\ \omega_z & 0 & 0 \\ 0 & 0 & 0 \end{bmatrix} \tag{4.7}$$

with $\omega_z = \dot{\theta}$ the angular velocity of Earth rotation.

Therefore, a perturbation in the initial state vector in the rotating frame maps to an arbitrary state as:

$$\delta\bar{x}(t) = \Phi(t, t_0)\delta\bar{x}(t_0) \tag{4.8}$$

Russell and Lara (2007) define the constraint that $\Delta z(T) = 0$. To allow validation of any initial state as given by ω_o, ω_e, this can be generalized to $\Delta z(T) = z_0$. This is accomplished in the propagation by means of a root finder that terminates the simulation exactly when N_r revolutions are completed, and the constraint is achieved. This results in a variation in the propagation time T, which shall be taken into account as another variable. A first-order expansion in t yields.

$$\delta\bar{x}(t+\delta t) = \delta\bar{x}(t) + \frac{\partial\bar{x}(t)}{\partial t}\delta t \tag{4.9}$$

Substitution of Eq. (4.8) results in the final state perturbation accounting for the propagation time perturbation.

$$\delta\bar{x}(t+\delta t) = \Phi(t, t_0)\delta\bar{x}(t_0) + \frac{\partial\bar{x}(t)}{\partial t}\delta t \tag{4.10}$$

This expression allows to apply the constraint that $\Delta z(T) = \Delta z(0) = 0$. From here onwards, the z component is removed from the state vector: $\bar{x} = \left[x, y, \dot{x}, \dot{y}, \dot{z}\right]$.

$$\delta z(T + \delta T) = \frac{\partial z(T)}{\partial \bar{x}(0)} \delta \bar{x}(0) + \dot{\bar{z}}(T)\delta T = 0 \implies \delta T = -\frac{1}{\dot{\bar{z}}(T)} \frac{\partial z(t)}{\partial \bar{x}(0)} \delta \bar{x}(0) \tag{4.11}$$

Replacing the constraint in the time perturbation into Eq. (4.10) leads to:

$$\Delta \bar{x}(T + \delta T) = \Big(\frac{\partial \bar{x}(T)}{\partial \bar{x}(0)} - \frac{1}{\dot{\bar{z}}(T)} \frac{\partial \bar{x}(T)}{\partial T} \frac{\partial z(T)}{\partial \bar{x}(0)} \Big) \Delta \bar{x}(0) = J(T) \Delta \bar{x}(0) \tag{4.12}$$

This defines the Jacobian matrix $J(T)$ for the differential corrector. Solving the following system yields the initial state change to correct for a mismatch in the periodicity condition.

$$\Delta \bar{x}(T + \delta T) - \Delta \bar{x}(0) = J(T) \Delta \bar{x}(0) \implies \Delta \bar{x}(T + \delta T) = (J(T) - I) \Delta \bar{x}(0) = A \Delta \bar{x}(0) \tag{4.13}$$

Matrix A is known in Floquet theory as the monodromy matrix, and it defines a Lyapunov map for the periodic orbit. Eigenanalysis can provide insights into the stability properties of the periodic orbit (e.g., Verhulst, 1996).

In some cases, it has been observed that the differential correction might get stuck near the periodic solution without meeting the requirements criteria. The Levenberg-Marquardt Algorithm (LMA) can be applied. It combines gradient descent and Gauss-Newton method by means of a damping factor λ to balance robustness far from minima and faster convergence near the minima (e.g., Press et al., 2007).

The initial state update through the LMA can be computed as:

$$\Delta \bar{x}(0) = (A^T A + \lambda I) A^T \Delta \bar{x}(T) \tag{4.14}$$

where the damping factor λ is adaptively selected with the following logic: it is reduced by a factor κ_- if the error decreases, else it is increased by a factor κ_+. A suitable initial value for the damping factor is $\lambda_0 = 10^{-9}$, whereas the adaptive factors $\kappa_- = 1.2$ and $\kappa_+ = 10$ provide convergence within 10 to 20 iterations for an arbitrary ground track.

4.2.1. Definition of the initial guess

The differential correction algorithm requires an initial guess to start the algorithm. A valid approach consists of computing the mean elements for the repeating orbit by means of Kaula's linear perturbation theory. However, neglecting the second-order perturbation due to Earth's oblateness sometimes leads to a poor initial guess. Although it might suffice for most cases. To mitigate this effect, 2nd order Brouwer theory can be applied to account for J_2^2 effects (Brouwer, 1959).

Employing the secular rates, a root finder can determine the mean semi-major axis for a given ground track with certain inclination i and eccentricity e such that:

$$f(a) = \frac{N_r}{N_d} + \frac{\dot{\omega}_o(a, e, i)}{\dot{\omega}_e(a, e, i)} = 0 \tag{4.15}$$

Next, the mean elements shall be converted to osculating elements. For this purpose, Eckstein-Ustinov theory has been applied following Spiridonova et al. (2014).

4.3. The periodic reference orbit

In Colombo (1984), the concept of the periodic reference orbit was introduced as a mean precessing ellipse. Nonetheless, in this work, the periodic reference orbit is obtained by computing the mean precessing circular orbit from the numerical simulation, that is averaging the orbital elements accordingly. This guarantees a perfect reference orbit for validation purposes.

The mean secular rates and the mean radius can be computed by averaging the numerical solution in time:

$$\begin{aligned}\hat{\dot{\omega}}_o &= \frac{1}{T_r}\int_0^{T_r} \dot{\omega}_o(t)\,dt \\ \hat{\dot{\Omega}} &= \frac{1}{T_r}\int_0^{T_r} \dot{\Omega}(t)\,dt \\ \hat{r} &= \frac{1}{T_r}\int_0^{T_r} r(t)\,dt \\ \hat{I} &= \frac{1}{T_r}\int_0^{T_r} I(t)\,dt\end{aligned} \tag{4.16}$$

Similarly, the initial values for the ascending node and argument of latitude can be defined by averaging the difference with respect to the osculating elements:

$$\begin{aligned}\omega_o^0 &= \frac{1}{T_r}\int_0^{T_r} \left(\hat{\dot{\omega}}_o t - \omega_o(t)\right)\,dt \\ \Omega_0 &= \frac{1}{T_r}\int_0^{T_r} \left(\hat{\dot{\Omega}} t - \Omega(t)\right)\,dt\end{aligned} \tag{4.17}$$

To conclude, the reference orbit can be determined as:

$$\bar{r}(t) = R_3(-\Omega_0 - \hat{\dot{\Omega}}t)R_1(-\hat{I})R_3(-\omega_o^0 - \hat{\dot{\omega}}_o t)\begin{pmatrix}\hat{r}\\0\\0\end{pmatrix} \tag{4.18}$$

4.4. Observation frequency spectrum comparison

In this section, the spectrum of the different observations is compared between the analytical and the numerical results by means of relative errors. In this analysis, a N_r/N_d=16/1 repeating orbit has been considered. To keep the spectrum large enough such that the cross-terms of the kite-matrix become relevant, i.e., $L > N_r/2$, a cut-off degree $L = 30$ has been selected. Moreover, to verify the influence of the initial state, an arbitrary non-zero initial state has been employed ($\omega_o^0 \approx -138°; \omega_e^0 \approx 32°$). A repeating ground track has been computed for an inclination of $I \approx 30°$. The value of the mean elements is approximate since they are slightly modified by the differential corrector. Numerical continuation could be employed to attain exact mean elements. This is not necessary for validation purposes. Also, note that a whole family of repeating ground tracks exists for such initial conditions (Lara, 2003). The repeating orbit period and initial state in the ECI frame are given below.

$$T_r = 84315.79958359114971\text{s}$$

$$\bar{r}_0 = \begin{bmatrix}-2117720.019494371366\\-5803860.074538999993\\-2191272.512207766282\end{bmatrix}\text{m}$$

$$\bar{v}_0 = \begin{bmatrix} +7114.620101870129280 \\ -1541.263803270827711 \\ -2801.407428554033319 \end{bmatrix} \text{m/s}$$

The computed orbit achieves errors in the periodicity condition of 10^{-9} m and 10^{-9} m/s when employing extended double precision. Numerical errors associated with element conversions have been detected when reconstructing the periodic orbit to compute the spectrum, causing periodicity errors of 10^{-4} m.

Furthermore, both Fourier cosine and sine spectra are studied, i.e., the A_{km} and B_{km} spectra, respectively, since the similar order of magnitude between coefficients could result in apparently correct magnitudes, whereas the phasing might be incorrect.

To begin with, the relative error of the gravity potential spectrum computed along the reference orbit is presented below. There is a nearly perfect match between numerical and analytical frequency spectra. Given the modular implementation of the block-kite model for the different observables, this already confirms the correct implementation of the linear system structure. Additionally, the sudden increase in the magnitude of the relative error spectra at higher frequencies can be attributed to numerical errors taking over. This is also associated with omission error in the lumped series that causes a drop in the magnitude of the lumped coefficients.

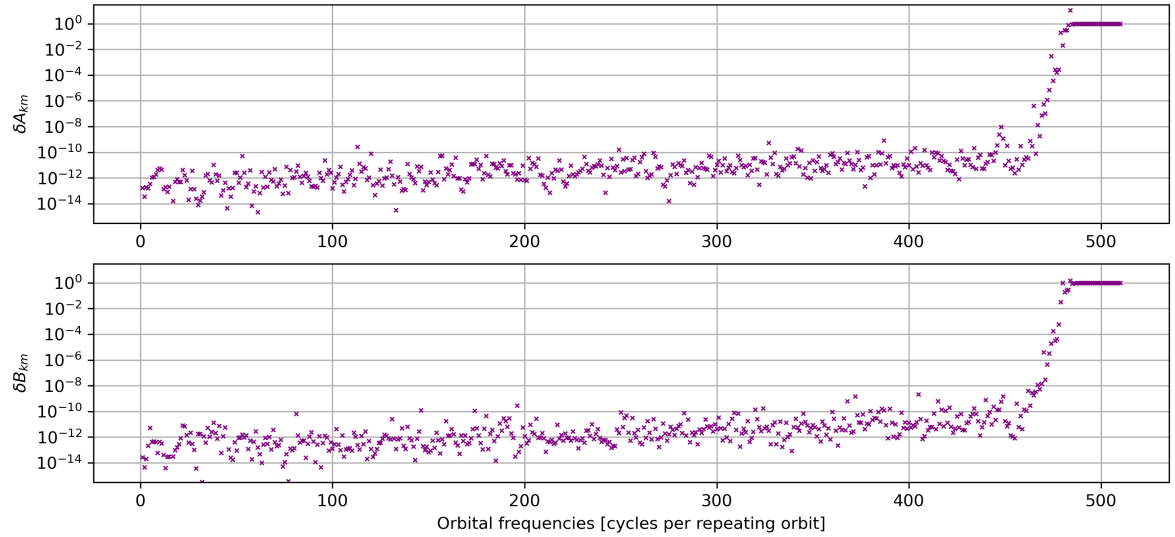

Figure 4.1: Numerical vs. analytical relative differences in gravity potential observation spectrum along the reference orbit

Next, the numerical potential is computed along the perturbed orbit to assess the line potential assumption. Figure 4.2 compares the numerical results to the analytical spectral observations.

While the majority of the spectrum shows good agreement, within 10%, high differences at a few orbital frequencies can be observed. This indicates the limitations of the line potential assumption. However, the behaviour of the spectrum is well captured overall.

Next, the GPS observation spectrum is computed for the three position components using the analytical observation model. The implied periodicity in the radial, along-track, and cross-track displacements is depicted in Figure 4.3, and the numerical and analytical observation spectra are compared in Figures 4.4 to 4.6.

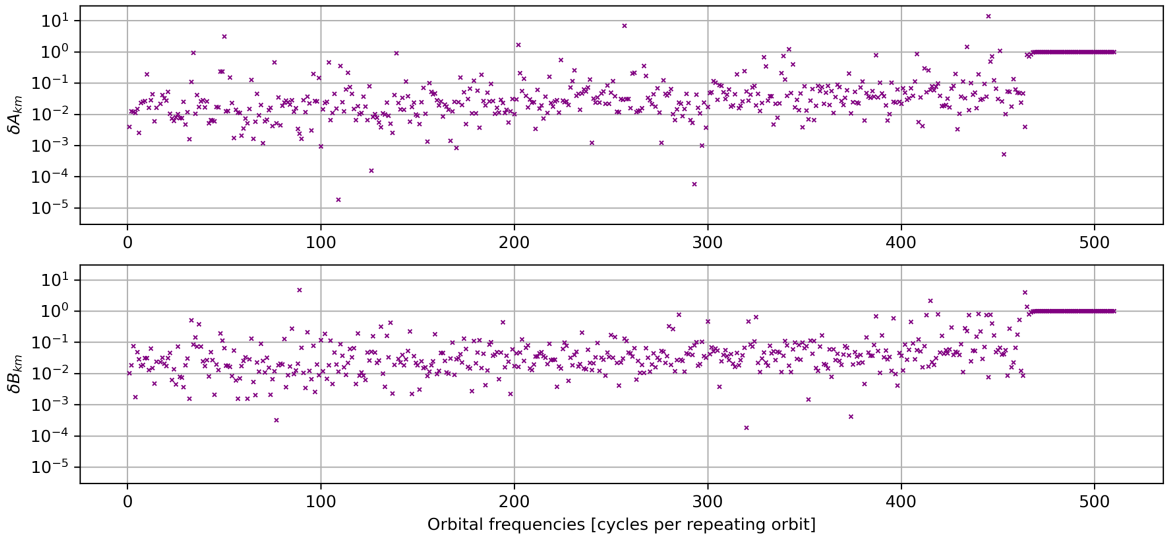

Figure 4.2: Numerical vs. analytical relative differences in gravity potential observation spectrum along the perturbed orbit

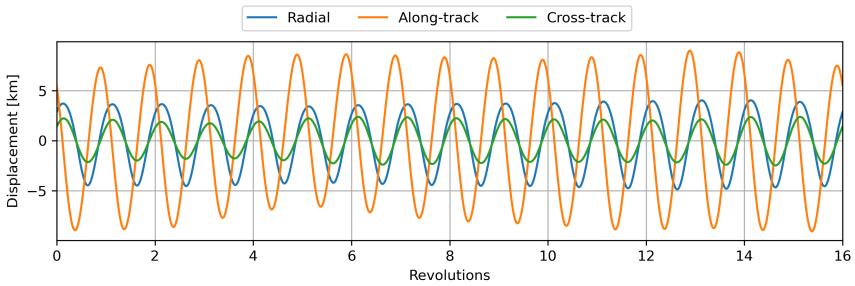

Figure 4.3: Time-series of numerical GPS observations

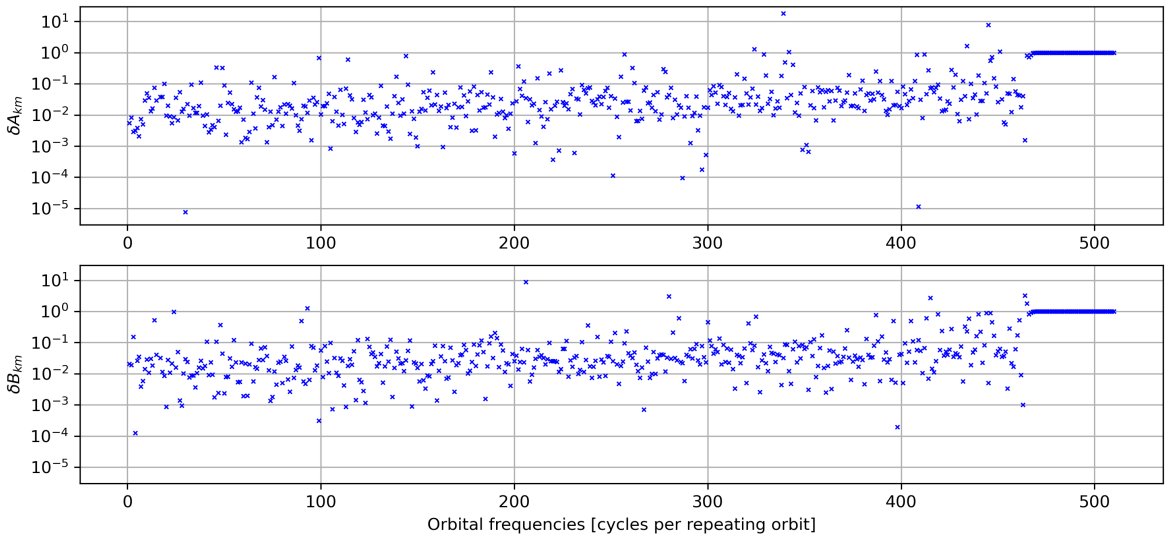

Figure 4.4: Numerical vs. analytical relative differences in radial observation spectrum

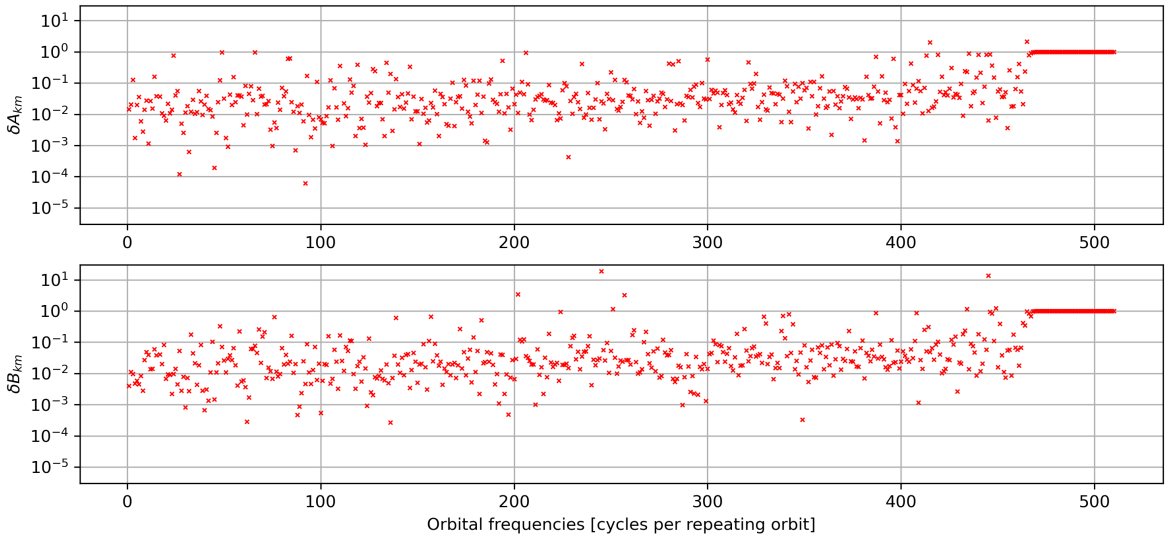

Figure 4.5: Numerical vs. analytical relative differences in along-track observation spectrum

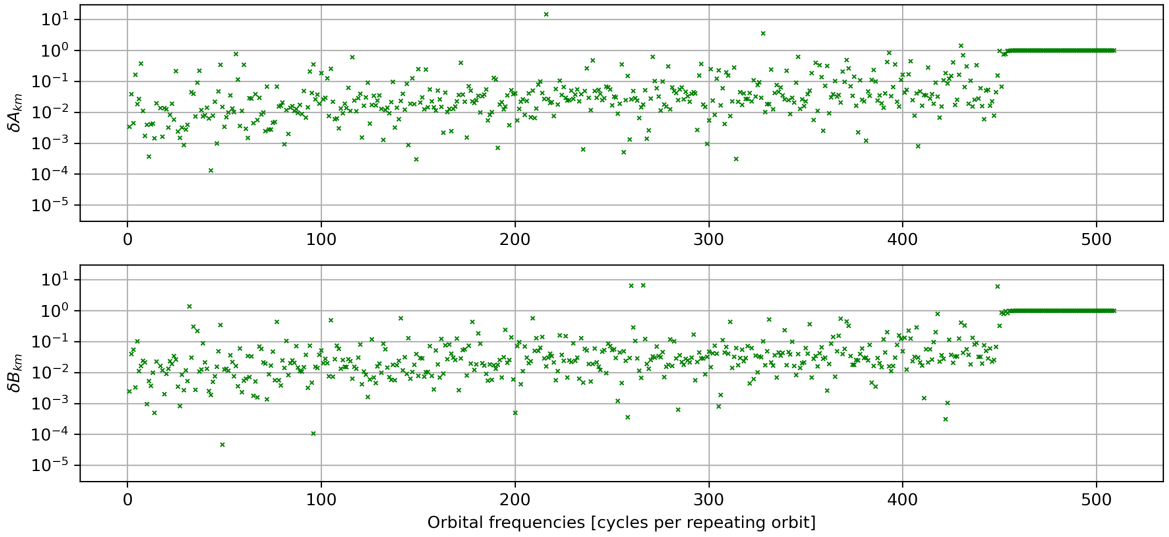

Figure 4.6: Numerical vs. analytical relative differences in cross-track observation spectrum

The analytical Global Positioning System (GPS) observations generally align with the numerical results. Similarly, discrepancies at higher frequencies are observed due to numerical errors. Compared to the potential observation along the perturbed orbit, the position spectra have degraded slightly. While the attenuation factor might damp higher degree effects for the potential, this could be compensated by the degree factors that appear in the transfer functions for the GPS observations. Thus, previously undetected errors might be amplified. The nature of these deviations could also be caused by the intrinsic linearization of the Hill equations as well as by numerical error sources during post-processing. The results, although not identical, suffice for verification purposes.

Lastly, the spectrum for the intersatellite range observation for a collinear formation is presented in Figure 4.7. Again, the numerical and analytical spectra show slightly less agreement since

errors have propagated from the radial and along-track observations. However, the analytical model is capable of capturing the majority of the spectrum behaviour to a sufficient accuracy.

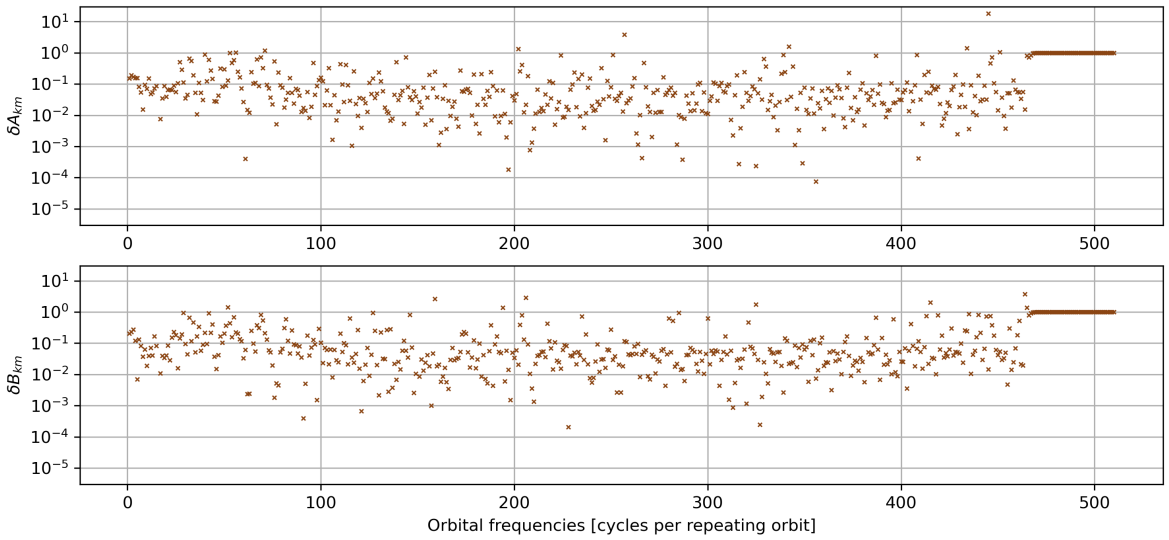

Figure 4.7: Collinear configuration: numerical vs. analytical relative differences in intersatellite range observation spectrum

To conclude, it must be taken into account that the main purpose of the analytical model is to propagate the error spectrum from the observations to the parameters. It is not intended to model orbits accurately. Instead, the analytical model shall solely be able to describe the magnitudes of the lumped coefficients' spectrum to a sufficient accuracy such that the error propagation is reliable. Further validation of the error propagation requires end-to-end simulation of a gravity research mission and is out of the scope of this project.

5

Analysis of results

In this chapter, the analytical observation model described in chapter 2 is employed to simulate the gravity recovery capabilities of different collinear configurations. For this purpose, the least squares error analysis approach presented in chapter 3 is employed. Firstly, a GRACE-like configuration consisting of a single satellite pair flying in a nearly polar orbit is analysed. In second place, the effect of adding an extra pair in an orbit with a lower inclination is assessed. This is the Bender configuration. An example of the mission design process, along with the optimization of the second-pair inclination, is discussed. Lastly, adding additional planes presents a possibility to bridge the gap towards near-real-time gravity field determination. For this purpose, constellations of multiple satellite pairs are simulated. The observation errors employed for every configuration are summarized in Figure 3.11 (see sections 3.6 and 3.7).

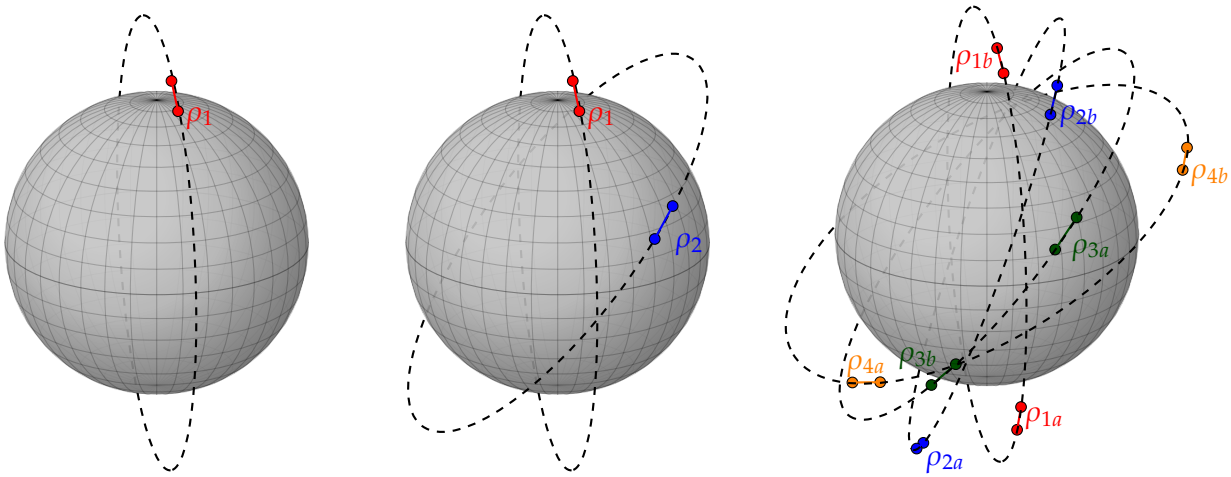

(a) GRACE **(b)** Bender configuration **(c)** Constellation example

Figure 5.1: Overview of orbital configurations

5.1. Single satellite pair

In this section, the error analysis results for a single pair of satellites flying in a collinear formation are discussed. To begin with, a sensitivity analysis is undertaken to verify the expected behaviour of the model. Next, a spherical harmonics error analysis is conducted to

reproduce certain patterns observed in GRACE gravity field solutions.

5.1.1. Sensitivity analysis

To begin with, a sensitivity analysis studies the influence of the three relevant parameters of a collinear configuration: inclination, semi-major axis (i.e. based on the repeating ground track choice) and nominal satellite separation. For this purpose, every parameter is varied within a reasonable range with respect to a reference configuration in a One-At-a-Time approach. For the sake of simplicity, the RMS per coefficient per degree is assessed.

$$\delta_l = \sqrt{\sum_{m=0}^{l} \frac{\sigma^2(\bar{C}_{lm}) + \sigma^2(\bar{S}_{lm})}{2l+1}} \tag{5.1}$$

The reference values for the sensitivity analysis are given in the table below:

Table 5.1: Sensitivity analysis reference collinear configuration

Parameter	Reference value
Inclination	88°
Repeating orbit	295/19
Nominal separation	400 km

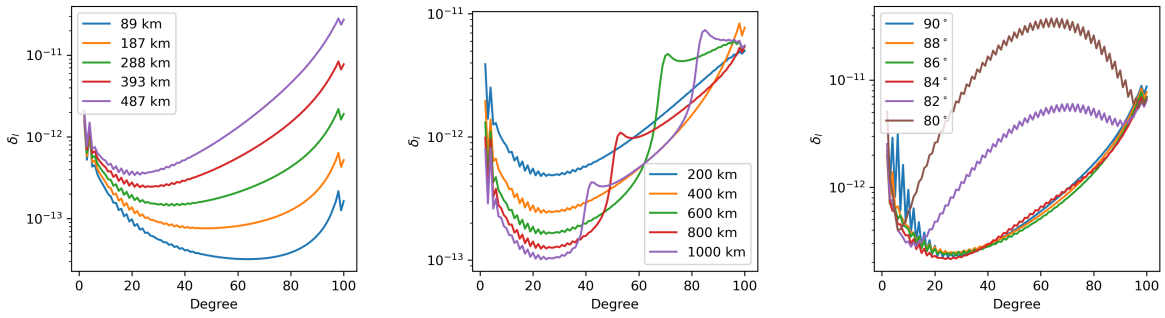

(a) Semimajor axis sensitivity **(b)** Baseline sensitivity **(c)** Inclination sensitivity

Figure 5.2: Collinear configuration sensitivity analysis

First, the sensitivity to the semi-major axis is studied. For this purpose, the number of revolutions is varied accordingly while maintaining the same number of nodal days. This aims at avoiding undesired effects due to the repeating ground track constraint. According to Figure 5.2a, the effect of the attenuation factor is evident. The lower the altitude, the lower the gravity field error. Aligned with the attenuation factor, the error difference generally becomes more pronounced for higher degrees.

Next, different nominal separations are analysed. Figure 5.2b shows a wiggling pattern whose frequency increases for larger intersatellite distances. This is the so-called common attenuation mode, as described in Wolff (1969). Sneeuw (2000) provides an analytical expression for the degree at which the common mode attenuation occurs.

$$l_i \approx \frac{2\pi i a_e}{\rho_0} \tag{5.2}$$

with $i = 0, 1, 2, \ldots$ referring to the i-th common mode attenuation. As shown in the figure, the first common mode attenuation occurs at the predicted mode by the expression presented above. Note also that the zeroth common mode attenuation is always present.

To conclude, Figure 5.2c depicts the sensitivity to the inclination. As expected, lower inclinations suffer from limited global coverage, thus resulting in an ill-posed problem that cannot be resolved. Such cases require constraining the normal equations to provide acceptable solutions. Furthermore, it is remarkable that the perfectly polar orbit is not optimal. Near-polar orbits such as $I = 88°$ show better degree variance performance. This can be associated with an inefficient distribution of measurements in the polar region for true polar orbits.

5.1.2. GRACE simulation

In this section, a GRACE-like configuration is simulated. More precisely, the resonant and non-resonant cases discussed in section 1.1 are simulated through the analytical model. The objective is to be able to reproduce the operational results in the GRACE monthly solutions.

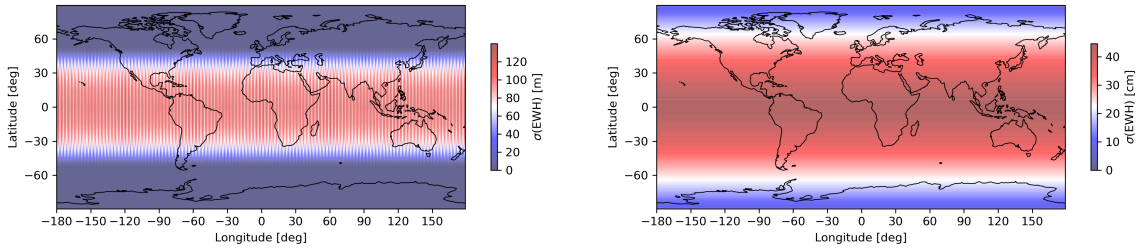

(a) September 2004 **(b)** March 2007

Figure 5.3: Analytical GRACE simulation: EWH commission error

The results from Figure 5.3 show the same pattern observed in the projected operational commission error as in the operational data (see Figure 1.1). The reason for the north-south error stripes for the resonant error is the correlation between different orders imposed with the repeating ground track constraint through the block-kite matrix. As Visser et al. (2012) point out for geoid heights, no longitude dependency appears if no cross-correlation between orders is introduced. A block-kite matrix is a generalization of the block-diagonal matrix when there is no correlation between order blocks. This occurs if the following condition holds $L < N_r/2$, i.e. only the bottom-left block-diagonal submatrix of the kite-matrix is considered.

To further analyse the results, the SH coefficients' spatial power noise spectrum is compared to the operational commission error in the figure below.

With respect to the non-resonant case, in light of Figure 5.4b, it provides a slightly optimistic estimation of the commission errors compared to the operational results. The noise power trend is, however, well captured. One possible explanation for the offset could be related to the residual background model errors. Despite this, the estimated EWH commission error is in a similar order of magnitude to that retrieved from ITSG-2018 data.

Regarding the resonant case, as shown in Figure 5.4a, the analytical model overestimates the commission error power. However, it is noticeable that the trend throughout the spectrum is also well described. A difference between the operational and analytical scenario lies in the fact that, in reality, the mission will never fly along the perfectly repeating orbit but can deviate during the time window of the gravity field solution. Indeed, the analytical model relies on the a-priori covariance to solve for the parameter covariance. Kaula's constraint has been

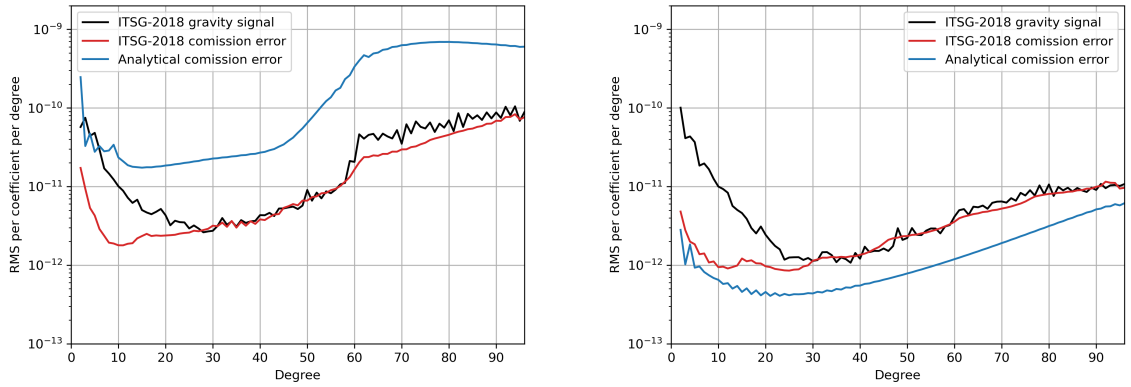

(a) September 2004 **(b)** March 2007

Figure 5.4: Analytical GRACE simulation: RMS per coefficient per degree. Comparison with ITSG-2018 solution.

employed since it represents the least stringent constraint, considering that the operational data consists of formal errors. At the same time, this can contribute to an overall growth of the power noise estimated by the analytical model. In contrast, the operational case does not require constraining the equations, since the system loses the ill-posedness as the satellite pair moves away from the resonance. It could be argued that the operational result is a weighted combination of the solutions of the different repeating ground tracks the satellites have followed throughout the solution time window. In this way, the solutions associated to other non-resonant repeating orbits act as constraints to the purely resonant solution, which dominates the error spectrum.

5.2. Bender configuration

In this section, the Bender configuration is studied to mitigate the spatial aliasing problem that causes equatorial comission error stripes due to insufficient ground track density. This configuration adds a satellite pair to the GRACE-like collinear formation with a lower inclination, thus improving the density of measurements near equatorial regions.

5.2.1. Sensitivity analysis

Analogously to the collinear formation, a sensitivity analysis of the Bender configuration is conducted to assess the effect of the constellation parameters. The reference values for the sensitivity analysis are given in the table below:

Table 5.2: Sensitivity analysis reference Bender configuration

Parameter	Reference value
Inclination 1	90°
Inclination 2	63°
Repeating orbit	295/19
Nominal separation	400 km

Similarly, the RMS per coefficient per degree sensitivity is studied. Results are presented in Figure 5.5.

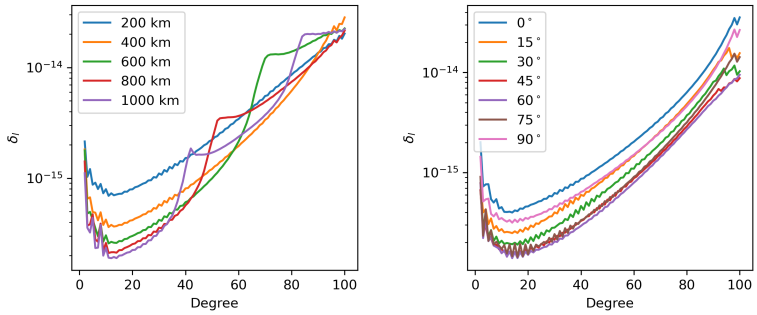

(a) Baseline sensitivity **(b)** Second pair inclination sensitivity

Figure 5.5: Bender configuration sensitivity analysis

As occured for the single satellite pair, the common mode attenuation appears at the expected degrees for higher baselines. Moreover, the error spectrum performs better for an intermediate range of inclinations $I \approx 60°$.

Lastly, the longitude difference between ground tracks is studied through two different policies: ground tracks overlap at the equator or ground tracks are interleaved at the equator (Wiese, Nerem, & Lemoine, 2011). Moreover, there exists a distinction between odd and even repeating ground tracks. The ascending and descending ground tracks from odd repeating ground tracks overlap with themselves at the equator. For a given orbit and policy, the equatorial ground track separation can be computed as follows:

$$\Delta\lambda_0 = \frac{\pi(i+1)(j+1)}{2N_r} \tag{5.3}$$

where i indicates the repeating ground track parity ($i = \text{mod}\,(N_r \cdot N_d, 2)$) and j takes an even or odd integer to define the even and odd policies, respectively. In this way, even means that there is interleaving at the equator, while odd can be associated with overlapping at the equator.

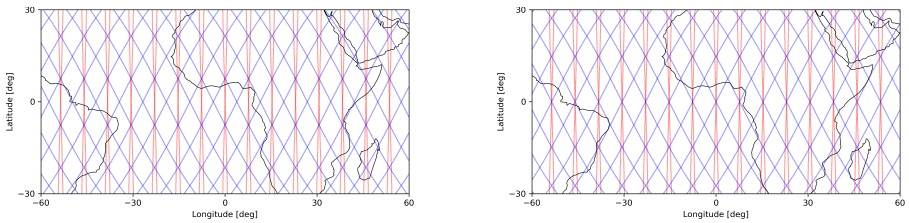

(a) Even policy **(b)** Odd policy

Figure 5.6: Ground-track longitude separation policy: odd repeating ground track

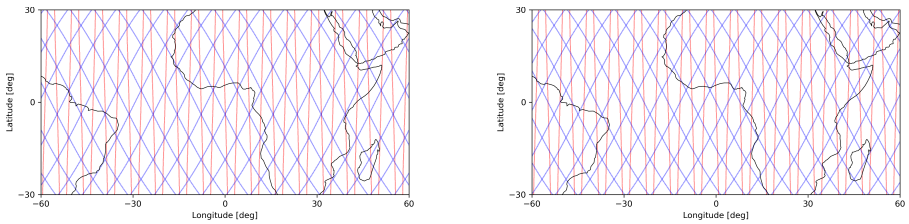

(a) Even policy **(b)** Odd policy

Figure 5.7: Ground-track longitude separation policy: even repeating ground track

In practice, the different longitude separation policies have little impact on the gravity field solutions. This can be observed in Figure 5.8, which shows the relative difference in RMS per coefficient per degree between the odd and even policies. The interleaving policy is taken as a reference value. Two different ground tracks are studied. The 15/1 repeating orbit is chosen because it is the most sparse ground track in LEO. Note that even for this case, the differences in spatial power noise remain within 10%. Moreover, the denser the ground track, the less impact the longitude separation policy has.

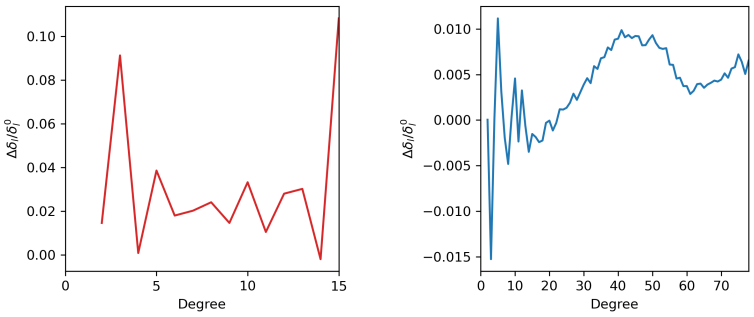

(a) N_r/N_d=15/1 ground track **(b)** N_r/N_d =78/5 ground track

Figure 5.8: Relative RMS per coefficient per degree difference: odd vs. even policy comparison.

In Figure 5.9, Spherical Harmonics Synthesis (SHS) into gravity anomaly errors confirms that the origin of the differences is the correlation between commission error and the ground track.

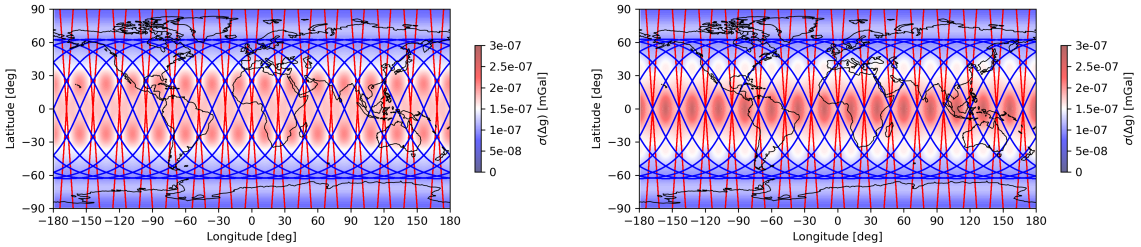

(a) Even policy **(b)** Odd policy

Figure 5.9: N_r/N_d=15/1 repeating ground track longitude policy comparison: gravity anomaly commission error.

In light of the obtained results, an interleaving policy will always be considered to separate the ground tracks of different planes.

5.2.2. Condition number analysis

Introducing an additional satellite pair shall not only improve the gravity field error, but it also mitigates the ill-posedness of the normal equations. This is depicted in Figure 5.10, where the condition number as a function of the cut-off degree is shown for a repeating ground track of 15/1 and 31/2, respectively. The condition number is the ratio between the largest and smallest singular values of a matrix. The larger the condition number, the more input errors are amplified in the output. When it approaches computer precision limits, the matrix cannot be reliably inverted, and the problem is ill-posed.

While unconstrained solutions for single-pair collinear configurations were unfeasible for $L > N_r$, this no longer holds for Bender configurations. Moreover, it might be expected that constraining the Bender observation equations might be needed for $L > 2N_r$ because of two

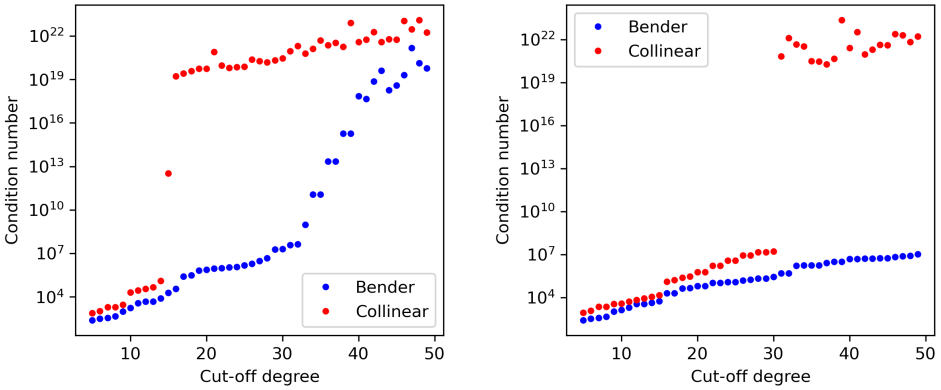

(a) N_r/N_d=15/1 repeating ground track **(b)** N_r/N_d=31/2 repeating ground track

Figure 5.10: Condition number analysis

times more observations. Nonetheless, the effect of the different inclinations relaxes this expectation (see specifically Figure 5.10a), thus facilitating unconstrained solutions even with lower spatial resolution.

5.2.3. Mission case scenario: optimal inclination

In this section, the inclination for the second satellite pair is optimized. To select the remaining parameters that define a Bender configuration, a mission case scenario is considered based on example mission requirements listed below.

Table 5.3: Mission requirements for an example GRM

ID	Requirement
MISS-01	The mission shall operate for 10 years
MISS-02	The satellites' mass propellant ratio shall not exceed 0.18
MISS-03	Gravity field solutions shall be provided every 5 days
MISS-04	Gravity field solutions up to degree 100 shall be computed

Requirements MISS-01 and MISS-02 define an orbit altitude lower limit. Several simulation studies have shown how mission lifetime relates to orbit altitude for a given mass-propellant ratio available for the drag-free system (Marchetti et al., 2008; Rock et al., 2006). They were gathered in Wiese, Nerem, and Lemoine (2011), where an exponential trend was identified (see Figure 5.11). As such, and taking some safety margin, an orbit requirement is introduced: the orbit altitude shall be greater than 300 km (ORB-01).

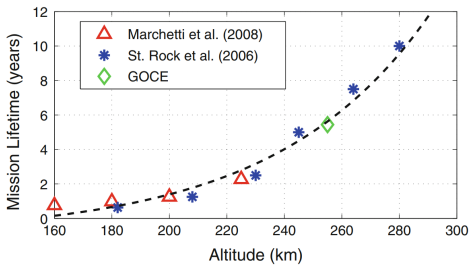

Figure 5.11: Mission lifetime vs. altitude: initial mass propellant fraction of 0.18 (Wiese, Nerem, & Lemoine, 2011)

Next, the combination of requirements MISS-03 and ORB-01 allows to define an optimal repeating ground track from the set of available periodic orbits in LEO. Requirement MISS-03 defines the repeating orbit period, that is, essentially the nodal days, considering that in LEO the following holds: $\dot{\Omega} \ll \dot{\theta}$. Besides this, to simplify operations, both satellite pairs are assumed to fly in the same repeating orbit. Studying different inclinations such that the semi-major axis is representative of the whole search space, referring to Figure 5.12, a ground track condition of 78/5 has been selected.

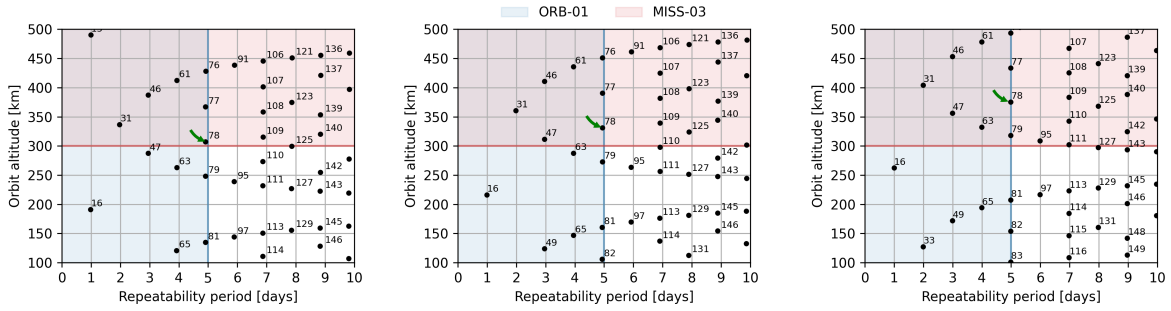

(a) Inclination = 10° **(b)** Inclination = 50° **(c)** Inclination = 90°

Figure 5.12: Repeating ground track selection

To conclude, an upper limit to the nominal intersatellite distance for both pairs can be computed from requirement MISS-04 such that the first-common mode attenuation is avoided. In this way, the nominal separation shall fulfil that $\rho_0 < 400km$. Further analysis of the search space is required to define an optimal baseline.

At this point, it is necessary to find an optimal value for the inclination of the second pair and the baseline between the satellites. For this purpose, a cost function is defined as the average of an arbitrary gravity field functional error (see appendix C) over the Earth's surface. This can be expressed as:

$$\hat{\sigma}_y^2 = \frac{1}{4\pi} \int_{\Omega} \sigma_y^2(\phi, \lambda)\, d\Omega \tag{5.4}$$

Substitution of the general expression for the gravity functionals partials w.r.t. the parameters, developing covariance propagation into summations and reformulating the integral in polar coordinates leads to (e.g. Haagmans and van Gelderen, 1991):

$$\begin{aligned} \hat{\sigma}_y^2 = \frac{1}{4\pi} \int_{-\frac{\pi}{2}}^{\frac{\pi}{2}} \int_0^{2\pi} \sum_{l=2}^{L} \sum_{m=0}^{l} \sum_{l'=2}^{L} \sum_{m'=0}^{l'} & f_y(l) f_y(l') \times \bar{P}_{lm}(\sin\phi) \bar{P}_{l'm'}(\sin\phi) \times \\ & \Big(\sigma(\bar{C}_{lm}, \bar{C}_{l'm'}) \cos m\lambda \cos m'\lambda + \\ & \sigma(\bar{S}_{lm}, \bar{S}_{l'm'}) \sin m\lambda \sin m'\lambda \\ & 2\sigma(\bar{C}_{lm}, \bar{S}_{l'm'}) \cos m\lambda \sin m'\lambda \Big) \sin\phi \, d\lambda \, d\phi \end{aligned} \tag{5.5}$$

Application of the orthogonal properties of spherical harmonics leaves that the integral is non-zero solely for $l = l', m = m', a = a'$. Moreover, given the normalization employed, it is 1 elsewhere (see appendix A). Therefore, it follows that:

$$\hat{\sigma}_y = \sqrt{\sum_{l=2}^{L} \sum_{m=0}^{l} f_y^2(l) \left(\sigma^2(\bar{C}_{lm}) + \sigma^2(\bar{S}_{lm}) \right)} \tag{5.6}$$

This expression does not require the computationally expensive covariance propagation, while it captures the functional behaviour over the Earth's surface, thus facilitating the optimization performance.

As a result, the full search space can be quickly explored, as Figure 5.13 presents. Hence, no elaborate optimization techniques are required, and the global minima can be selected directly. In this work, EWH has been used as the gravity functional. Figure 5.13a shows cost function sensitivity to the inclination at the optimal baseline, while Figure 5.13b describes the sensitivity to the nominal intersatellite distance at the optimal inclination.

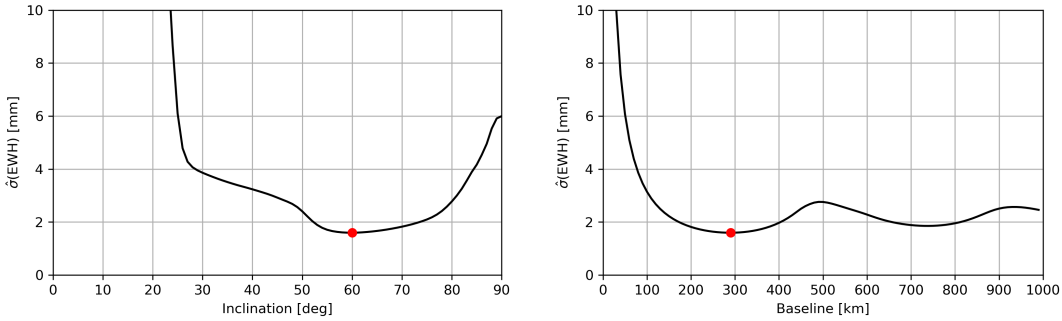

(a) Optimal inclination

(b) Optimal nominal intersatellite distance

Figure 5.13: Bender mission case scenario: optimal parameters

The optimal inclination has been defined to $I = 60°$. This value is similar to the chosen value for the NGGM that NASA is planning to launch (Bender et al., 2025). The optimal nominal separation is $\rho_0 = 290$km, while the NGGM mission is aiming at a slightly smaller baseline. Nonetheless, the optimal region both for the baseline and the inclination is rather flat, which allows comparatively similar performance for alternative nearby values that might favour other mission aspects.

To conclude, Figure 5.14 shows the commission error map for EWHs. There is a subtle longitudinal anisotropy associated with the combined ground track footprint. Moreover, there are certain latitudes that suffer from larger errors. As expected due to ground track density, latitudes exactly above the inclination of the second pair, as well as equatorial areas, are the most affected ones. It must be highlighted that the optimal inclination achieves to balance

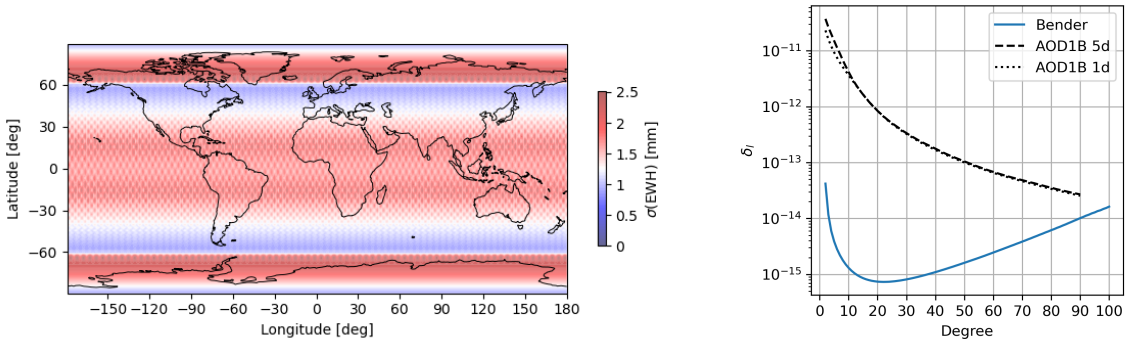

(a) EWH commission error

(b) RMS per coefficient per degree: commission error vs. AOD1B signal

Figure 5.14: Mission case scenario optimal Bender configuration

commission errors at these two areas. A lower inclination of the second pair would give rise to higher commission errors above latitudes not covered by the second pair. On the contrary, an excessively high inclination of the second pair would result in commission errors dominating in equatorial regions.

The obtained results, with commission errors in the order of millimetres for EWH, are similar to Li et al. (2016), who also analyse Bender configurations considering NGGM performance by means of an analytical approach. Some simulation-based studies also yield similar mission capabilities from instrument errors (Cesare et al., 2022; Daras et al., 2023). However, full noise simulations indicate that actual performance is degraded (Bender et al., 2025; Daras et al., 2023), for example, due to aliasing of tidal and non-tidal effects (Daras et al., 2023).

5.3. Multi-satellite constellations

In section 3.8.2, the intrinsic lower bound for time-varying gravity field solutions was discussed. This is implicitly restricted by the LEO repeating ground track characteristics (see Figure 5.12) that do not achieve nodal days below 24 hours. In this chapter, multi-satellite constellations are studied with the aim of mitigating the time aliasing problem, but also to solve the spatial aliasing problem of orbits with short repeatability periods. The time resolution can be solved by placing several satellites in the same repeating ground track such that measurements over the full ground track are retrieved in times below the repeatability period. For example, for a ground track with a repeating period of 1 day, if gravity field solutions every 3 hours were intended, 8 satellites would be required. To circumvent the sparsity of these ground tracks, more orbital planes can be added, similarly to the Bender configuration. Analogously, they require proper selection of optimal inclinations.

While launching that many satellites might seem far-fetched due to elevated mission costs, the technological advancements towards miniaturization could eventually allow the feasibility of this mission concept. For instance, if each satellite cost was reduced by a factor of 10 to 100 times, the idea could be financially viable. Pfaffenzeller and Pail (2023) claim that, in the future, a miniaturized version of the K-Band Ranging (KBR) instrument of GRACE-FO could be available. Moreover, ONERA is currently developing an accelerometer, CubSTAR, aimed at being employed in CubeSats, and that surpasses current GRACE-FO capabilities. The performance of GRACE-FO MWI and the CubSTAR accelerometer will be assumed for a constellation-based GRM. The gravity field recovery capabilities of an arbitrary constellation of CubeSat collinear pairs will be assessed.

Ideally, missions with daily or sub-daily gravity field solutions should make use of repeating orbits with nodal periods of 1 day. In this way, more satellites could be placed in alternative planes to exploit the benefits of using a variety of inclinations. The 16/1 repeating orbit could be a suitable orbit, which implies an orbit altitude between 180-260 km. For a CubeSat-based mission that is assumed not to fly drag-free, this is considered excessively low. As a result, the 15/1 repeating orbit, although at higher orbital altitudes, around 500 km, consists of a more plausible selection, and it has been chosen for the simulations presented in this section. Alternatively, the 31/2 repeating orbit could be a trade-off solution that would, however, require placing two times more satellites in the same plane to achieve similar temporal resolutions.

First, the baseline separation will be assumed constant for any configuration. Arbitrarily and aligned with GRACE-FO, a nominal intersatellite distance of ρ_0 = 220km is defined.

The optimization of the inclinations of the multiple planes becomes a multivariate optimization

problem:

$$\begin{aligned} &\text{Minimize:} && f(\bar{x}) \\ &\text{Subject to:} && 0^\circ < x_{N-1} < x_{N-2} < \cdots < x_0 < 90^\circ \\ & && \bar{x} \in \mathbb{R}^N \end{aligned}$$

with $\bar{x} = I_1, I_2, \cdots, I_{N_p-1}$ the decision variables. They are the inclinations of every plane except for one plane that is fixed to provide global coverage, i.e. $I_0 = 90°$. Therefore, the search space has dimension $N = N_p - 1$, with N_p the number of orbital planes. The inequality conditions are aimed at reducing the search space, avoiding nearly symmetric solutions. The cost function is chosen to be the averaged EWH, analogously to the Bender optimal solution. A cut-off degree is selected following condition number analysis, such that the system is guaranteed to be well-posed.

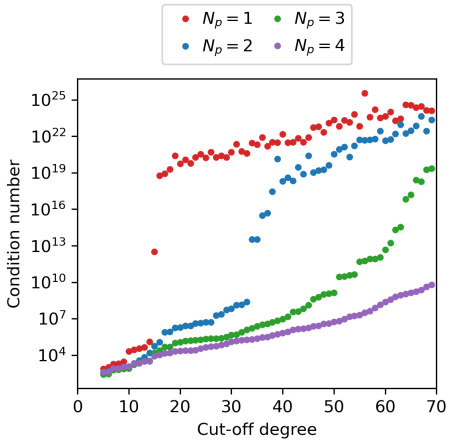

Figure 5.15: Constellation condition number analysis

As previously discussed for the Bender configuration, additional planes add observations to the system that allow for solving gravity fields of higher degree. In principle, a single pair system results in ill-posedness for $L > N_r$. Adding a satellite pair delays the ill-conditioned behaviour to roughly $L > 2N_r$. However, the effect of a different inclination relaxes this criterion. According to Figure 5.15, this can be extrapolated to constellations. As a general rule, a system will be well-conditioned for $L < N_r N_p$. In this way, several optimizations will be simulated for an increasing number of planes such that more resolution is intended, i.e., higher cut-off degree.

Exploration of the whole search space becomes exponentially expensive with the number of decision variables. Considering that the evaluation of the cost function can take up to 2 seconds for higher cut-off degrees, efficient optimization techniques are required. Unfortunately, analysis of the design space of the Bender configuration optimization already showed the non-convex behaviour of the cost function. Therefore, global optimization algorithms such as evolutionary algorithms represent a reasonable optimizer choice (e.g. Glover and Sörensen, 2015). These population-based algorithms are inspired by natural evolution. They contain a population of individuals (solutions) that are evolved by means of genetic operations such as mutation or crossover. At the end of every generation, the fittest individuals in terms of the cost function are selected, and their genetic material will be employed for the next generation. The aim of this section is not to provide the best solution but rather to assess the capabilities of a nearly optimal solution and study its properties. Moreover, the Bender configuration already showed a rather flat region near the optimal solution, which still maintained similar

performance. In summary, exhaustive optimization has not been intended. The optimizer has been selected conveniently as the self-adaptive Differential Evolution algorithm (Brest et al., 2006; Elsayed et al., 2011) with default settings from ESA's optimization library PyGMO (Biscani & Izzo, 2020). Differential Evolution algorithms iteratively improve solutions using differences between population members. The algorithm is self-adaptive because mutation and crossover parameters are adapted on-the-fly to balance exploration and exploitation. Moreover, a stopping criterion has been defined as 10 iterations without improving the cost function by more than 0.1%.

While smaller design spaces allows for the finding of an optimal solution within 2 to 3 iterations, more orbital planes imply slower convergence. Figure 5.16 shows the population evolution for a 6-plane constellation and illustrates the slower convergence behaviour.

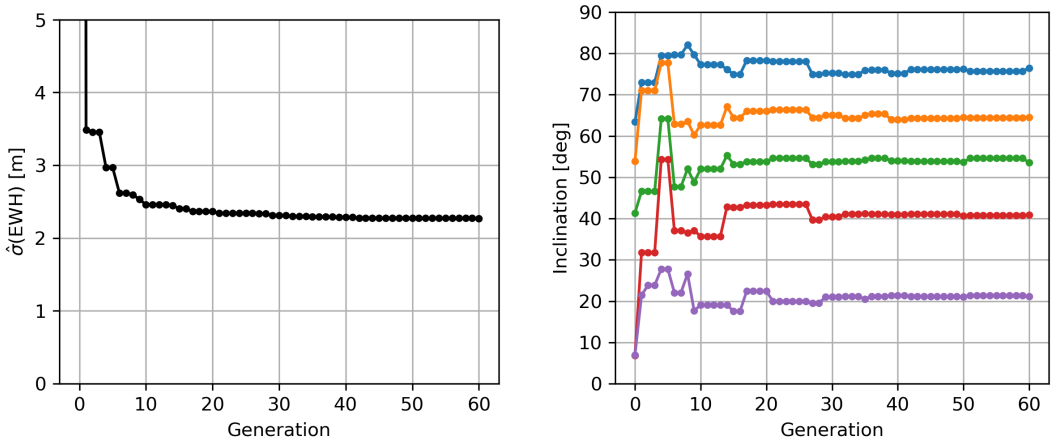

(a) Cost function **(b)** Design variables: constellation planes inclinations

Figure 5.16: Constellation with 6 planes in a N_r/N_d=15/1 repeating orbit: generation champion evolution.

The resulting optimal inclinations for up to 6 orbital planes are presented in Figure 5.17. As one could expect, the inclinations span over the whole domain for higher planes. Similarly, higher inclinations are preferred over lower inclinations, which are more spaced out.

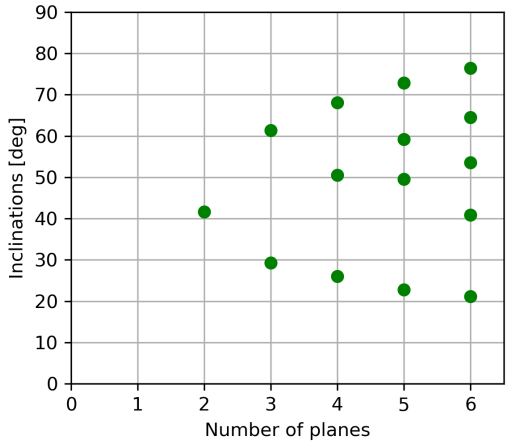

Figure 5.17: Optimal constellations in a N_r/N_d=15/1 repeating orbit

To conclude, the obtained spatial noise power is compared to the AOD1B signal to assess the recovery capabilities of the computed constellations. In light of the results shown in Figure 5.18,

the CubeSat constellation would be able to retrieve the daily atmospheric and ocean non-tidal signal almost up to degree 25, which would consist of spatial resolutions of slightly above 800 km. For this purpose, 3 planes with 1 satellite pair each would be sufficient. Furthermore, the power of sub-daily phenomena (e.g., 3h period) is lower than the variability associated with the mean daily field. As a result, the aliasing of these short-periodic events would not play a limiting role. Regarding solutions at 3-hour intervals, they would require placing 8 satellite pairs per plane. Three orbital planes would provide a solution without noise, approximately up to degree 15, that is roughly 1300 km spatial resolution. Employing a total of 48 satellite pairs would suffice to observe the AOD1B signal up to degree 20 or roughly a spatial resolution of 1000 km. The improvements associated with a higher number of planes are minimal, and such constellations are not advised for the instrument performance considered. Improvement of the accelerometers and ranging system performance is paramount to attain the observability of higher degrees at the temporal resolutions considered.

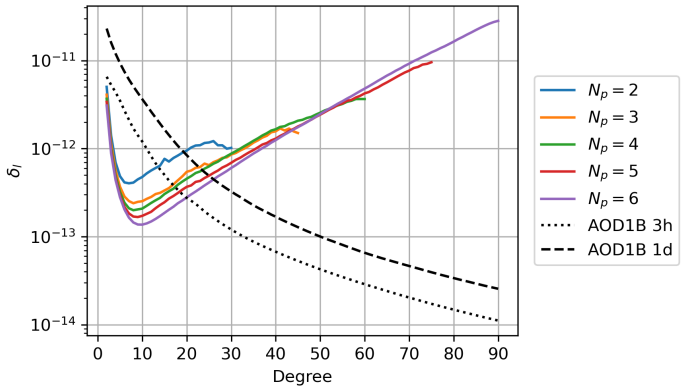

Figure 5.18: RMS per coefficient per degree: constellation noise vs. AOD1B signal comparison

6

Conclusion

In this thesis, orbital configurations for GRM with the aim of improving spatial and temporal resolution have been studied by means of an analytical spectral observation model.

In chapter 1, the current limitations of temporal gravity field data were introduced and put into perspective with science and societal demands. Section 1.3 formulated a main research question along with several sub-questions. Chapters 2 to 5 have addressed these questions. In this chapter, the answers to the research questions are presented along with additional insights gained in this work. To conclude, recommendations for future work are outlined.

6.1. Research questions

> How can the analytical approach be applied to multi-satellite constellations? What are the limitations of this methodology?

In chapter 2, the analytical observation model was formulated for GPS observations and intersatellite range for collinear formations. Subsequently, the linear system was introduced, and the least squares methodology was explained in chapter 3. Section 3.5 specifically delves deeper into this question by defining a framework to combine any set of observations. A constellation of satellites or satellite pairs would also imply the combination of multiple observations. The individual linear systems can be combined simply by stacking the design matrices vertically. Moreover, assuming no correlation between the observations, diagonally stacking the individual observation covariances results in the full observation covariance for the constellation.

Regarding the limitations of the methodology, the assumptions of the analytical observation model are stated in chapter 2. First, the line potential assumption consists of approximating the potential along the perturbed orbit as a potential along a reference orbit. Secondly, the linearized Hill equations do not account for higher-order terms. Lastly, the collinear formation intersatellite range observations rely on a first-order approximation that can be interpreted as projecting the range variations along the satellites' line of sight. This fact, for example, neglects the cross-track contribution. Subsequently, chapter 4 has verified the implementation of the analytical model by means of numerical simulation of the lumped coefficients' spectrum for the different observables. The line potential assumption introduces noticeable differences between the numerical and analytical potential observations. They propagate to GPS observations and

collinear observations, which show additional degradation because of the other assumptions. Overall, while there are significant deviations at a few frequencies, the behaviour of the spectra is well captured. The least squares error propagation does not require refined estimation of the partial derivatives with respect to the parameters. Further analysis of the validity of the model to gravity field error analysis would require end-to-end simulations and has been considered out of the scope of the project.

How can equatorial stripe errors be defined?

This question was almost completely addressed in chapter 1 itself, with the description of the striping pattern problem in GRACE data. Two types of striping patterns were identified.

First, striping patterns arise in the process of SHS into gravity anomalies and EWH. They are attributed to commission error dominating the gravity field solution at higher frequencies. Furthermore, it was shown how Gaussian smoothing is typically applied to mitigate this issue as a low-pass filter in the spatial domain.

Secondly, equatorial stripes can be observed in the commission error synthesis for resonant orbits. The lumped theory successfully explained this pattern by means of the repeating ground-track constraint that introduces correlation between SH coefficients of different orders.

The definition of the stripe errors has been limited to the commission errors themselves. The methodology does not explain the stripes for non-resonant cases since it implies longitude homogeneity of the commission errors (Visser et al., 2012). However, the commission errors can provide an estimation of the magnitude of the stripes. As long as this is smaller than the actual signal, the stripes will not appear. This comparison has been conducted in terms of RMS per coefficient per degree for Bender and multi-satellite constellation configurations, which can describe the amplitude spectrum of the signal and commission errors in the spatial domain.

What are the optimal parameters for a Bender configuration? How does it perform in terms of spatial aliasing errors?

The analytical model has been employed to simulate Bender configurations for sub-weekly solutions. Several factors that drive Bender configuration design have been discussed through a mission case scenario. A challenge posed by this question is the definition of optimality. Depending on the purpose of the mission, this might differ significantly. Moreover, trade-offs between different mission goals might be required. For simplicity in this work, the objective has been defined as the global determination of EWH. As a result, a unit sphere average of the EWH commission error has been chosen as the cost function for the optimization problems discussed.

An optimal inclination has been found at $I = 60°$ and the optimal nominal intersatellite distance has been calculated to be $\rho_0 = 290$ km. However, this only applies to the mission performance and requirements considered. A flat area near the global optimum has also been identified. This provides a range of both inclinations and nominal intersatellite distance with nearly-optimal performance, which could be beneficial when considering other mission trade-offs.

As a result, the feasibility of recovering the atmosphere and ocean non-tidal signals up to degree 100 was demonstrated, making use of the NGGM instrument performance for 5-day solutions, i.e., a spatial resolution of 200 km. While agreement with previously published results was achieved (Cesare et al., 2022; Daras et al., 2023; Li et al., 2016), the analytical model does not account for temporal aliasing effects, which can significantly degrade commission errors (Daras et al., 2023).

What are the optimal parameters of a multi-satellite constellation for a high temporal resolution GRM? How does it perform in terms of spatial aliasing errors?

Multi-satellite CubeSat constellations were studied as an alternative to improve time resolution while maintaining affordable mission costs.

The previous discussion about optimality also applies to this question. Similarly, EWH averaged commission error has been considered as the cost function for this problem. Optimal inclinations have been computed for up to 6 different repeating orbits. It has been identified that they spread out in the range of inclinations favouring higher inclinations over less advantageous lower inclinations.

In light of current technological progress in small satellites, realizability of daily and sub-daily gravity field monitoring has been proven up to roughly degree 20, i.e., a resolution of around 1000 km.

How do instrument errors impact the selected optimal configurations?

Chapter 3 assumed that the intersatellite range observation noise ASD consists of the combined contribution of the ranging instrument itself and the onboard accelerometers of the satellites. However, it has been discussed that this assumption neglects other error sources that can dominate the observation error spectrum, in particular, background error models.

Regarding only instrument errors, the accelerometers' error drives the range error spectrum at lower frequencies, while the ranging instrument is the main contributor at higher frequencies. In this way, for example, LRIs would significantly reduce noise at higher frequencies, while a DFAOCS, along with a refined accelerometer, benefits the lower frequencies.

Moreover, a scaling factor applied to the observation covariance, i.e., the observation PSD, scales the parameter covariance by the same factor. This holds as long as the solutions are unconstrained, and explains, for example, the significantly better performance of the Bender configuration analysed under NGGM performance.

The exact influence on the studied optimal configurations requires further consideration.

6.2. Future recommendations and final remarks

The science community and society would benefit from spatial and temporal resolution improvement in Earth gravity field measurements. However, high mission costs, engineering complexities, and limited commercial applications of gravity field data compromise future GRMs. Cutting-edge ranging systems based on lasers, along with high resolution accelerometers and an advanced DFAOCS, can pave the way towards mitigating noise at higher spatial frequencies while also achieving better temporal resolution. However, short-periodic events can still affect the recovered gravity signal. CubeSats constellations are a potential solution to avoid reliance on background models and enable accurate retrieval of fast variations in Earth's gravity field.

Although the findings of this study are promising for the future of Earth-based GRM, the limitations of this work must not be ignored. To begin with, end-to-end simulations must be undertaken to assess the validity of the analytical model implemented to estimate gravity field errors. Furthermore, the analytical model does not include the effects of background error models, which have shown a major impact on GRACE/GRACE-FO performance. This could be achieved by characterization of an acceleration power noise spectrum and subsequent

propagation into collinear range errors. In this way, analytical model power noise estimations might increase and, eventually, match operational results. Besides this, a limited range of orbital configurations and mission scenarios has been investigated. For example, the 31/2 repeating orbit is a promising selection for near real-time gravity field recovery, and it might outperform the 15/1 repeating orbit discussed here because of the impact of the attenuation factor. Moreover, this work has only considered collinear configurations. Li et al. (2016) formulated the analytical observation equations for the pendulum configuration, and the methodology could be extended to other formations such as cartwheel orbits. Although complex from the engineering perspective, the analytical model provides a unique tool to quickly estimate their gravity recovery capabilities. Combinations of the different formations could improve gravity field measurements to an extent that must be defined. Another important aspect lies in the instrument errors considered. The use of other instruments such as quantum accelerometers (e.g., Zahzam et al., 2022), characterized by lower noise at lower frequencies, or simplified gravity reference sensors (Dávila Álvarez et al., 2022) must be assessed. In addition, studying the commission error sensitivity to the different parts of the observation error spectrum is crucial to identifying technological needs for future missions. Lastly, studies have included alternative observations such as range-rate or range acceleration (e.g., Li et al., 2016; Sneeuw, 2000). Their applications to constellation-based GRM could also improve performance.

This work has shown the benefits of the analytical methodology for future GRMs that demand intense optimization. It has also been particularly efficient to model constellations, which represent a plausible scenario for the future of satellite gravimetry on Earth. This has allowed identifying potential solutions to solve spatial aliasing errors by means of the Bender configuration, but also to demonstrate that CubeSat constellations could be an affordable alternative to improve temporal resolution.

A

Associated Legendre polynomials

A.1. Recursive relationships

To evaluate the spherical harmonics expansion of the gravity potential it is necessary to compute the associated Legendre polynomials. The efficient computation of such polynomials is paramount for any software routine aiming at modelling a gravity field. For this purpose, recursive relationships are leveraged. Here, the Fixed-Order-Increasing-Degree (FOID) approach, or alternatively standard forward column method, is described (Holmes & Featherstone, 2002). Other algorithms exist, for instance, the standard forward row method, or Clenshaw approaches. The formulation here described can become numerically unstable for $m > 1900$ due to underflow in the sectorial terms (Gleason, 1985). This is sufficient for the purpose of this work.

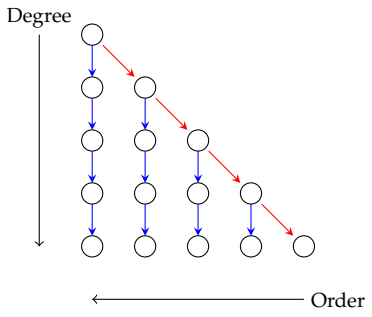

Figure A.1: Standard forward column method

First, the following auxiliary variables are defined:

$$a_{lm} = \sqrt{\frac{(2l-1)(2l+1)}{(l-m)(l+m)}}$$

$$b_{lm} = \sqrt{\frac{(2l+1)(l+m-1)(l-m-1)}{(l-m)(l+m)(2l-3)}}$$

Also, given the colatitude θ, sine and cosine values are stored:

$$t = \cos\theta \qquad u = \sin\theta$$

Two recursion formulas are then applied. First a recursion over the sectorial terms is carried out:

$$\bar{P}_{lm}(\theta) = u\sqrt{\frac{2m+1}{2m}}\bar{P}_{m-1,m-1}(\theta), \forall m > 1 \tag{A.1}$$

This recursion is initialized with $\bar{P}_{0,0}(\theta) = 1$ and $\bar{P}_{1,1}(\theta) = \sqrt{3}u$.

Subsequently, for every sectorial term, the order is fixed and a recursion over increasing degrees is applied.

$$\bar{P}_{lm}(\theta) = a_{lm}t\bar{P}_{l-1,m}(\theta) - b_{lm}\bar{P}_{l-2,m}(\theta), \forall l > m \tag{A.2}$$

A.2. Derivatives of Legendre polynomials

For certain applications in astrodynamics, it is of interest to compute derivatives of associated Legendre polynomials. Some examples are the derivatives of the inclination functions that are required in the GPS cross-track observations. Here, the derivative with respect to the colatitude is presented. It suffices to compute:

$$\frac{dP_{lm}(\theta)}{d\theta} = \frac{1}{u}\left(lt\bar{P}_{lm}(\theta) - f_{lm}\bar{P}_{l-1,m}(\theta)\right), \forall l \geq m \tag{A.3}$$

where

$$f_{lm} = \sqrt{\frac{(l^2-m^2)(2l+1)}{(2l-1)}} \tag{A.4}$$

For sectorial terms, $f_{mm} = 0$ and expression simplifies to

$$\frac{d\bar{P}_{lm}(\theta)}{d\theta} = m\frac{t}{u}\bar{P}_{m,m}(\theta), \forall m \geq 0 \tag{A.5}$$

A.3. 2nd order derivatives of Legendre polynomials

Similarly, the 2nd order derivatives are required for certain applications. They are of special interest to compute the gravity gradient tensor, which is required in gradiometry as well as to formulate variational equations.

Recursive formulations follow from the derivation of Eqs. (A.3) and (A.5).

$$\frac{d^2\bar{P}_{lm}(\theta)}{d\theta^2} = \frac{1}{u}\left((l-1)t\frac{d\bar{P}_{lm}(\theta)}{d\theta} - f_{lm}\frac{d\bar{P}_{l-1,m}(\theta)}{d\theta}\right) - l\bar{P}_{lm}(\theta) \tag{A.6}$$

Analogously to the sectorial first order derivatives, $f_{mm} = 0$ and expression takes a simpler form:

$$\frac{d^2\bar{P}_{mm}(\theta)}{d\theta^2} = (m-1)\frac{t}{u}\frac{d\bar{P}_{mm}(\theta)}{d\theta} - m\bar{P}_{mm}(\theta) \tag{A.7}$$

A.4. Normalization

The recursion relationships exist for normalized associated Legendre functions. The normalization arise from the orthogonal properties of spherical harmonics (Heiskanen & Moritz,

1967).

$$Y_{lma}(\theta,\lambda) = \begin{Bmatrix} \cos m\lambda \\ \sin m\lambda \end{Bmatrix}_{a=0}^{a=1} P_{lm}(\cos\theta) \tag{A.8}$$

$$\int_{\Omega} Y_{lma}(\theta,\lambda) Y_{l'm'a'}(\theta,\lambda)\, d\Omega = \frac{4\pi(l+m)!}{(2l+1)(2-\delta_{0m})(l-m)!} \tag{A.9}$$

This defines the normalization constant N_{lm}:

$$N_{lm} = \sqrt{\frac{(2-\delta_{0m})(2l+1)(l-m)!}{(l+m)!}} \tag{A.10}$$

that defines the fully-normalised versions of spherical harmonics, associated Legendre functions and Stokes coefficients as:

$$\bar{P}_{lm} = N_{lm} P_{lm} \tag{A.11}$$

$$\bar{Y}_{lma} = N_{lm} Y_{lma} \tag{A.12}$$

$$\bar{C}_{lma} = \frac{1}{N_{lm}} C_{lma} \tag{A.13}$$

In this way, the following holds:

$$\frac{1}{4\pi} \int_{\Omega} \bar{Y}_{lma} \bar{Y}_{l'm'a'}\, d\Omega = 1 \tag{A.14}$$

The normalization is leveraged in the recursive relationships to avoid overflow due to factorials computation.

B

Inclination functions

B.1. Inclination functions and the FFT

Alternative formulations of a potential term for an arbitrary order l and degree m have been presented in this work.

$$V_{lm} = \frac{\mu}{r}\left(\frac{a_e}{r}\right)^l \bar{P}_{lm}\left(\sin\phi\right)\left[\bar{C}_{lm}\cos m\lambda + \bar{S}_{lm}\sin m\lambda\right] \tag{B.1}$$

$$V_{lm} = \frac{\mu}{r}\left(\frac{a_e}{r}\right)^l \sum_{p=0}^{l} \bar{F}_{lmp}(I)\cdot\left\{\begin{bmatrix}\bar{C}_{lm}\\ -\bar{S}_{lm}\end{bmatrix}_{l-m=\text{odd}}^{l-m=\text{even}} \cos\left[(l-2p)u + m(\omega-\theta)\right] + \begin{bmatrix}\bar{S}_{lm}\\ \bar{C}_{lm}\end{bmatrix}_{l-m=\text{odd}}^{l-m=\text{even}} \sin\left[(l-2p)u + m(\omega-\theta)\right]\right\} \tag{B.2}$$

Wagner (1983) proposes to compute the inclination functions applying a FFT to a unit perturbing potential computed along an inclined great circle. For this purpose, setting $\mu = 1, a_e = 1, r = 1, \bar{C}_{lm} = 1, \bar{S}_{lm} = 1, \Omega - \theta = 0$ the following holds:

$$T = \bar{P}_{lm}(\sin\phi)\left[\cos m\lambda + \sin m\lambda\right] = \sum_{p=0}^{l} \bar{F}_{lmp}(I)\cdot\left\{\begin{bmatrix}1\\ -1\end{bmatrix}_{l-m=\text{odd}}^{l-m=\text{even}} \cos\left(l-2p\right)u + \sin\left(l-2p\right)u\right\} \tag{B.3}$$

where T is the unit disturbing potential. The right-hand side looks very similar to a Fourier series. Indeed, taking $i = l - 2p$ one could express:

$$T = C_0 + \sum_{i=1}^{l} C_i \cos iu + S_i \sin iu \tag{B.4}$$

Note that i might take negative values. However, those terms can be rewritten applying

$$\cos x = \cos\left(-x\right) \qquad \sin x = -\sin\left(-x\right)$$

Let's take an example for $l = 5$.

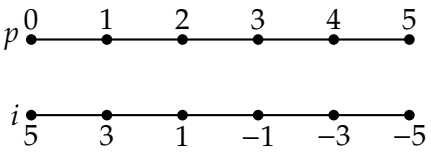

Terms $\cos 5u, \sin 5u$ are obtained from the unit perturbing potential for $p = 0, p = 5$, i.e. $p = \frac{l-i}{2}, \frac{l+i}{2}$ for $i = \pm 5$:

$$\bar{F}_{lm0}(I) \left\{ \begin{bmatrix} 1 \\ -1 \end{bmatrix} \cos 5u + \sin 5u \right\}$$

$$\bar{F}_{lm5}(I) \left\{ \begin{bmatrix} 1 \\ -1 \end{bmatrix} \cos 5u - \sin 5u \right\}$$

Solving for cosine and sine terms respectively yields:

$$\begin{aligned} (\bar{F}_{lm0} + \bar{F}_{lm5}) \cos 5u \cdot \begin{bmatrix} 1 \\ -1 \end{bmatrix} &= C_5 \cos 5u \\ (\bar{F}_{lm0} - \bar{F}_{lm5}) \sin 5u &= S_5 \sin 5u \end{aligned}$$

Then, it is possible to solve for F_{lm_0} and F_{lm_5} as follows:

$$\bar{F}_{lm0} = \frac{C_5 \begin{bmatrix} 1 \\ -1 \end{bmatrix} + S_5}{2} \qquad \bar{F}_{lm5} = \frac{C_5 \begin{bmatrix} 1 \\ -1 \end{bmatrix} - S_5}{2}$$

This solution can be extrapolated to any pair $p = \frac{l-i}{2}, \frac{l+i}{2}$.

$$\bar{F}_{lm,\frac{l-i}{2}} = \frac{C_i \begin{bmatrix} 1 \\ -1 \end{bmatrix} + S_i}{2} \qquad \bar{F}_{lm,\frac{l+i}{2}} = \frac{C_i \begin{bmatrix} 1 \\ -1 \end{bmatrix} - S_i}{2} \tag{B.5}$$

Also note that since l is odd, even terms C_i do not exist and are taken to zero. Let's now take an example where C_0 does exist, i.e. l even, for example $l = 4$

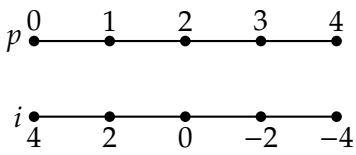

Then, it follows that

$$\bar{F}_{lm2} \begin{bmatrix} 1 \\ -1 \end{bmatrix} = C_0 \implies \bar{F}_{lm2} = C_0 \begin{bmatrix} 1 \\ -1 \end{bmatrix}$$

This can be generalized for the central p point whenever l is even.

$$\bar{F}_{lm,\frac{l}{2}} = C_0 \begin{bmatrix} 1 \\ -1 \end{bmatrix} \tag{B.6}$$

B.2. Derivatives of the inclination functions

For certain applications, it is useful to compute the derivative of the inclination functions. For this purpose, the principle based on the FFT of a unit perturbing potential computed along a great circle is applied. Instead, the Fourier transform is applied to the inclination derivative of the unit perturbing potential. Derivation of both sides of Eq. (B.3) leads to:

$$\frac{dT}{dI} = \frac{d\bar{P}_{lm}(\cos\theta)}{d\theta}\frac{d\theta}{dI}\left[\cos m\lambda + \sin m\lambda\right] + \bar{P}_{lm}(\cos\theta)m\left[-\sin m\lambda + \cos m\lambda\right]\frac{d\lambda}{dI} = \tag{B.7}$$

$$= \sum_{p=0}^{l}\frac{d\bar{F}_{lmp}(I)}{dI}\cdot\left\{\begin{bmatrix}1\\-1\end{bmatrix}_{l-m=\text{odd}}^{l-m=\text{even}}\cos(l-2p)u + \sin(l-2p)u\right\} \tag{B.8}$$

where

$$\cos\theta = \sin\phi = \sin I\sin u \qquad \tan\lambda = \tan u\cos I \tag{B.9}$$

and therefore the derivatives read as (Lian-Da & Hong-Bo, 2012):

$$\frac{d\theta}{dI} = \frac{-\sin u\cos I}{\sqrt{1-\sin^2 I\sin^2 u}} \qquad \frac{d\lambda}{dI} = \frac{-\tan u\sin I}{\sqrt{1-\cos^2 I\tan^2 u}} \tag{B.10}$$

Derivatives of the associated Legendre polynomials are calculated according to section A.2.

Similarly, it is concluded that the unit perturbing potential takes the form of a Fourier series:

$$\frac{dT}{dI} = C_0 + \sum_{i=1}^{l} C_i\cos iu + S_i\sin iu \tag{B.11}$$

Therefore the following expressions hold:

$$\frac{d\bar{F}_{lm,\frac{l-i}{2}}}{dI} = \frac{C_i\begin{bmatrix}1\\-1\end{bmatrix} + S_i}{2} \qquad \frac{d\bar{F}_{lm,\frac{l+i}{2}}}{dI} = \frac{C_i\begin{bmatrix}1\\-1\end{bmatrix} - S_i}{2} \tag{B.12}$$

Moreover, whenever l is even.

$$\frac{d\bar{F}_{lm,\frac{l}{2}}}{dI} = C_0\begin{bmatrix}1\\-1\end{bmatrix} \tag{B.13}$$

B.3. Cross-track derivatives and cross-track inclination functions

In section 2.3 the following expression for the potential cross-track derivative was presented.

$$\frac{\partial V}{\partial w} = \frac{1}{r}\left\{\sin\omega_o\frac{\partial V}{\partial I} + \frac{\cos\omega_o}{\sin I}\left(\frac{\partial V}{\partial\omega_o}\cos I - \frac{\partial V}{\partial\omega_e}\right)\right\} \tag{B.14}$$

Here, the reformulation of the cross-track derivative is described in detailed. In this way, this section deals with the derivation of the cross-track inclination functions that significantly simplify the notation of the cross-track potential derivative observation.

The partial derivatives with respect to the orbital elements ω_o, ω_e, I can be developed from Eq. (2.15).

$$\begin{aligned}\frac{\partial V}{\partial I} &= \sum_{k=-L}^{L}\sum_{m=0}^{L} A_{km}^{I}\cos\psi_{km} + B_{km}^{I}\sin\psi_{km}\\ \begin{bmatrix}A_{km}^{I}\\B_{km}^{I}\end{bmatrix} &= \sum_{l=l_{min},2}\frac{\mu}{r}\left(\frac{a_e}{r}\right)^{l}\frac{\partial\bar{F}_{lmk}(I)}{\partial I}\begin{bmatrix}\tilde{C}_{lm}\\\tilde{S}_{lm}\end{bmatrix}\end{aligned} \tag{B.15}$$

$$\begin{aligned}\frac{\partial V}{\partial \omega_o} &= \sum_{k=-L}^{L}\sum_{m=0}^{L} A_{km}^{\omega_o}\cos\psi_{km} + B_{km}^{\omega_o}\sin\psi_{km} \\ \begin{bmatrix}A_{km}^{\omega_o}\\ B_{km}^{\omega_o}\end{bmatrix} &= \sum_{l=l_{min},2}^{L}\frac{\mu}{r}\left(\frac{a_e}{r}\right)^l \cdot k \cdot \bar{F}_{lmk}(I)\begin{bmatrix}\tilde{S}_{lm}\\ -\tilde{C}_{lm}\end{bmatrix}\end{aligned} \tag{B.16}$$

$$\begin{aligned}\frac{\partial V}{\partial \omega_e} &= \sum_{k=-L}^{L}\sum_{m=0}^{L} A_{km}^{\omega_e}\cos\psi_{km} + B_{km}^{\omega_e}\sin\psi_{km} \\ \begin{bmatrix}A_{km}^{\omega_e}\\ B_{km}^{\omega_e}\end{bmatrix} &= \sum_{l=l_{min},2}^{L}\frac{\mu}{r}\left(\frac{a_e}{r}\right)^l \cdot m \cdot \bar{F}_{lmk}(I)\begin{bmatrix}\tilde{S}_{lm}\\ -\tilde{C}_{lm}\end{bmatrix}\end{aligned} \tag{B.17}$$

The cross-track potential derivative can then be written in the following form:

$$\frac{\partial V}{\partial w} = \sum_{k=-L}^{L}\sum_{m=0}^{L}(A_{km}^{c}\cos\psi_{km} + B_{km}^{c}\sin\psi_{km})\cos\omega_o + (A_{km}^{s}\cos\psi_{km} + B_{km}^{s}\sin\psi_{km})\sin\omega_o \tag{B.18}$$

with the following lumped coefficients

$$\begin{aligned}\begin{bmatrix}A_{km}^{c}\\ B_{km}^{c}\end{bmatrix} &= \sum_{l=l_{min},2}^{L}\frac{\mu}{r^2}\left(\frac{a_e}{r}\right)^l \bar{F}_{lmk}(I)\cdot\frac{k\cos I - m}{\sin I}\begin{bmatrix}\tilde{S}_{lm}\\ -\tilde{C}_{lm}\end{bmatrix} \\ \begin{bmatrix}A_{km}^{s}\\ B_{km}^{s}\end{bmatrix} &= \sum_{l=l_{min},2}\frac{\mu}{r^2}\left(\frac{a_e}{r}\right)^l \frac{\partial \bar{F}_{lmk}(I)}{\partial I}\begin{bmatrix}\tilde{C}_{lm}\\ \tilde{S}_{lm}\end{bmatrix}\end{aligned} \tag{B.19}$$

Next, the following trigonometric identities are applied, with $a = \psi_{km}$, $b = \omega_o$:

$$\begin{aligned}\cos a\cos b &= \frac{1}{2}(\cos(a+b) + \cos(a-b)) \\ \sin a\cos b &= \frac{1}{2}(\sin(a+b) + \sin(a-b)) \\ \cos a\sin b &= \frac{1}{2}(\sin(a+b) - \sin(a-b)) \\ \sin a\sin b &= \frac{1}{2}(\cos(a-b) - \cos(a+b))\end{aligned} \tag{B.20}$$

Introducing also that $\psi_{km} + \omega_o = \psi_{k+1,m}$ and $\psi_{km} - \omega_o = \psi_{k-1,m}$, the following expressions are obtained.

$$\begin{aligned}\frac{\partial V}{\partial w} = \frac{1}{2}\sum_{k=-L}^{L}\sum_{m=0}^{L} & A_{km}^{c}\left(\cos\psi_{k+1,m} + \cos\psi_{k-1,m}\right) + \\ & B_{km}^{c}\left(\sin\psi_{k+1,m} + \sin\psi_{k-1,m}\right) + \\ & A_{km}^{s}\left(\sin\psi_{k+1,m} - \sin\psi_{k-1,m}\right) + \\ & B_{km}^{s}\left(\cos\psi_{k-1,m} - \cos\psi_{k+1,m}\right)\end{aligned} \tag{B.21}$$

Grouping terms with same ψ_{km} results in (Schrama, 1989):

$$\begin{aligned}\frac{\partial V}{\partial w} &= \sum_{k=-L-1}^{L+1}\sum_{m=0}^{L} A_{km}^{w}\cos\psi_{km} + B_{km}^{w}\sin\psi_{km} \\ A_{km}^{w} &= \frac{1}{2}\left(A_{k-1,m}^{c} + A_{k+1,m}^{c} + B_{k+1,m}^{s} - B_{k-1,m}^{s}\right) \\ B_{km}^{w} &= \frac{1}{2}(B_{k-1,m}^{c} + B_{k+1,m}^{c} + A_{k-1,m}^{s} - A_{k+1,m}^{s})\end{aligned} \tag{B.22}$$

with $A_{km}^{c,s} = B_{km}^{c,s} = 0$ for $|k| > L$. The expression can be simplified employing the cross-track inclination functions.

$$\bar{F}^*_{lmk}(I) = \frac{1}{2}\left\{\frac{(k-1)\cos I - m}{\sin I}\bar{F}_{lm,k-1} + \frac{(k+1)\cos I - m}{\sin I}\bar{F}_{lm,k+1}(I) - \bar{F}'_{lm,k-1}(I) + \bar{F}'_{lm,k+1}(I)\right\} \tag{B.23}$$

$$\begin{bmatrix} A^w_{km} \\ B^w_{km} \end{bmatrix} = \sum_{l=l^*_{min},2}^{L} \frac{\mu}{r^2}\left(\frac{a_e}{r}\right)^l \bar{F}^*_{lmk}(I)\begin{bmatrix} \tilde{S}_{lm} \\ -\tilde{C}_{lm} \end{bmatrix} \tag{B.24}$$

Summation over l starts at $l^*_{min} = \min(l_{min,k-1}, l_{min,k+1})$ as defined at the start of chapter 2. Also, the cross-track inclination functions should handle forbidden inclination function indices. This can be achieved by $\bar{F}_{lmk}(I) = \bar{F}'_{lmk}(I) = 0$ for $|k| > l$.

C

Spherical harmonics synthesis

A function on a sphere $f(\theta, \lambda)$ can be formulated in terms of a spherical harmonics expansion. This is known as SHS.

$$f(\theta, \lambda) = \sum_{l=0}^{\infty} \sum_{m=0}^{l} \bar{P}_{lm}(\cos\theta) \left(\bar{C}_{lm} \cos m\lambda + \bar{S}_{lm} \sin m\lambda \right) \tag{C.1}$$

In physics, the SH coefficients of the potential are employed to compute different gravity fields functionals that allow to interpret the retrieved gravity field data.

C.1. Geoid height

The term geoid was first proposed by Gauss and defines an equipotential surface for the gravity field that is followed by mean sea level (Heiskanen & Moritz, 1967).

$$W(x, y, z) = W_0 \tag{C.2}$$

A reference ellipsoid can then be defined as the best fitting ellipsoid. Also, it follows from the equipotential surface definition from a normal gravity potential.

$$U(x, y, z) = W_0 \tag{C.3}$$

The difference between the geoid and the reference ellipsoid is defined in terms of geoid heights N. This deviation arises due to different mass distributions across the globe. Its definition is relevant to provide a consistent framework to determine elevation measurements.

Geoid heights can be derived from a perturbing potential T with the Bruns equation.

$$N = \frac{T}{\gamma} \tag{C.4}$$

with $\gamma = \gamma_P$ the normal gravity at the reference ellipsoid. Geoid heights can be computed through SH as follows.

$$N(\theta, \lambda) = a_e \sum_{l=2}^{\infty} \sum_{m=0}^{l} \bar{P}_{lm}(\cos\theta) \left(\bar{C}_{lm} \cos m\lambda + \bar{S}_{lm} \sin m\lambda \right) \tag{C.5}$$

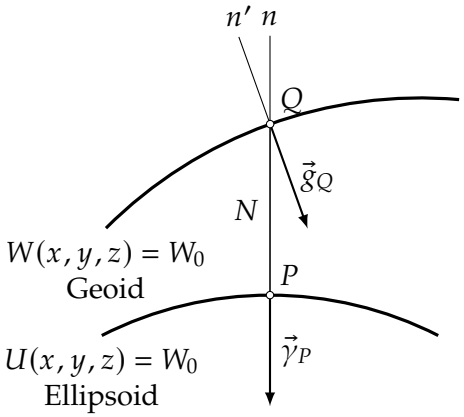

Figure C.1: Geoid and reference ellipsoid (Heiskanen & Moritz, 1967)

C.2. Gravity anomalies

The gravity anomaly vector is defined as the difference between the gravity vector at the geoid and the normal gravity vector at the reference ellipsoid.

$$\Delta\vec{g} = \vec{g}_P - \vec{\gamma}_Q \tag{C.6}$$

The difference in magnitude is the gravity anomaly.

$$\Delta g = g_P - \gamma_Q \tag{C.7}$$

It can also be computed from the perturbing potential.

$$\Delta g = -\frac{\partial T}{\partial r} - \frac{2}{r}T \tag{C.8}$$

Therefore, they can be expressed (in milligals) through SHS.

$$\Delta g(\theta,\lambda) = 10^5 \times \sum_{l=2}^{L}\sum_{m=0}^{l}\frac{\mu}{a_e^2}(l-1) \times \left(\bar{C}_{lm}\cos m\lambda + \bar{S}_{lm}\sin m\lambda\right) \tag{C.9}$$

C.3. Equivalent water height

Observed changes in gravity field can be assumed to be associated to mass redistribution in a thin layer on the Earth's surface. This allows the definition of surface mass density anomalies (e.g. Wahr et al. (1998)). In short timescales, mass redistribution can be mainly attributed to water redistribution. Therefore, it is more intuitive to define EWH dividing surface mass densities by water density ρ_w.

$$H(\theta,\lambda) = \frac{a_e\rho_e}{3\rho_w}\sum_{l=2}^{\infty}\sum_{m=0}^{l}\bar{P}_{lm}(\cos\theta)\frac{2l+1}{1+k'_l} \times \left(\Delta\bar{C}_{lm}\cos m\lambda + \Delta\bar{S}_{lm}\right) \tag{C.10}$$

where $\Delta\bar{C}_{lm}, \Delta\bar{S}_{lm}$ are the difference in the SH coefficients with respect to a static reference gravity field, $\rho_e = 5300\,\mathrm{kg/m^3}$ and $\rho_w = 1000\,\mathrm{kg/m^3}$ are average Earth and water densities, and k'_l are the elastic Love numbers (see Wahr et al., 1998, Table 1).

C.4. Gaussian spatial smoothing

GRACE monthly unconstrained solutions suffer from high noise at higher SH coefficients, as a result, a north-south striping pattern arises in the gravity anomalies or EWH maps. An approach to circumvent this issue consists of applying spatial smoothing through the isotropic Gaussian averaging filter described by the Green function (Jekeli, 1981; Wahr et al., 1998).

$$W(\psi) = \frac{2be^{-b(1-\cos\psi)}}{1-e^{-2b}} \tag{C.11}$$

where ψ is a spherical distance and b is a parameter that defines the extent of the spatial smoothing in terms of the smoothing radius r.

$$b = \frac{\ln 2}{1-\cos r/a_e} \tag{C.12}$$

By definition, $W(0) = 1$ and the smoothing radius is the distance at which the kernel value has dropped to $W(\psi) = 0.5$.

Smoothing can be applied directly in the SH domain through degree dependent terms $W_l(\psi)$, defined as follows:

$$W_l = \int_0^\pi W(\psi) P_l(\cos\psi)\sin\alpha\, d\alpha \tag{C.13}$$

Jekeli (1981) proposes a recursive computation of the coefficients W_l. However, it can become unstable at higher degrees. Piretzidis and Sideris (2019) discusses different stable methodologies. The continued fraction with backward recursion approach has been employed in this work (Piretzidis & Sideris, 2019). First, backward recursion is applied from the maximum degree L.

$$\rho_{l-1} = \frac{1}{\frac{1}{b}+\frac{2l}{b}+\rho_l}, \quad L \geq l \geq 1 \tag{C.14}$$

with the initial condition $\rho_L = 0$. Then, the second step consists of a forward recursion relation.

$$W_l = \rho_{l-1} W_{l-1}, \quad L \geq l \geq 1 \tag{C.15}$$

starting off with $W_0 = 1$.

C.5. Global spherical harmonic synthesis computation

There exist efficient computation techniques to evaluate the different gravity field functionals on a global spherical grid. Rizos (1979) observed that latitude and longitude dependent terms could be handled separately redefining the summation:

$$\sum_{l=0}^{\infty}\sum_{m=0}^{l} \rightarrow \sum_{m=0}^{\infty}\sum_{l=m}^{\infty} \tag{C.16}$$

In this way, one could redefine the synthesis in a two-step process (e.g. Sneeuw, 1994).

$$\left.\begin{matrix} A_m(\theta) \\ B_m(\theta) \end{matrix}\right\} = \sum_{l=m}^{\infty} \bar{P}_{lm}(\cos\theta) \left\{\begin{matrix} \bar{C}_{lm} \\ \bar{S}_{lm} \end{matrix}\right. \tag{C.17}$$

$$f(\theta,\lambda) = \sum_{m=0}^{\infty} A_m(\theta)\cos m\lambda + B_m(\theta)\sin m\lambda \tag{C.18}$$

Further acceleration can be obtained when computing Eq. (C.18) with the inverse FFT.

C.6. Covariance propagation

In this work, SHS is not too computationally expensive. However, since the work deals with an error analysis, error propagation from the parameter vector of SH coefficients to the gravity field functionals is of interest. This process can become very intense. The efficient global SHS computation described in the previous section can be applied to covariance propagation (Schrama, 1991a).

First, covariance propagation is conducted as follows.

$$\sigma_y^2(\theta, \lambda) = \bar{v}^T P_{xx} \bar{v} \tag{C.19}$$

where P_{xx} is the covariance matrix of the SH coefficients and $\bar{v}$ is a column vector that consists of the partials with respect to the SH coefficients.

This can be reformulated into:

$$\sigma_y^2(\theta, \lambda) = \bar{v}^T \bar{w} \tag{C.20}$$

The elements of $\bar{w}$ have the following form:

$$w_i = \sum_{l=0}^{\infty} \sum_{m=0}^{l} \bar{P}_{lm}(\cos\theta) \left(A_{lm} \cos m\lambda + B_{lm} \sin m\lambda\right) \tag{C.21}$$

where A_{lm}, B_{lm} follow from the specific functional along with the elements of the i-th row of P_{xx}. The two-step fold can be applied to every element w_i.

$$\left.\begin{matrix} C_m(\theta) \\ B_m(\theta) \end{matrix}\right\} = \sum_{l=m}^{\infty} \bar{P}_{lm}(\cos\theta) \left\{\begin{matrix} A_{lm} \\ B_{lm} \end{matrix}\right. \tag{C.22}$$

$$w_i = \sum_{m=0}^{\infty} C_m(\theta) \cos m\lambda + D_m(\theta) \sin m\lambda \tag{C.23}$$

While application of the inverse FFT to Eq. (C.23) significantly speeds up the propagation of a dense covariance, in this work, sparse parameter covariances appear. This can cause the direct evaluation of the summation to be more efficient.

Bibliography

4D Dynamic Earth Project [Accessed: 2025-05-22]. (2025). https://4ddynamicearth.tudelft.nl/

Abich, K., Abramovici, A., Amparan, B., Baatzsch, A., Okihiro, B. B., Barr, D. C., Bize, M. P., Bogan, C., Braxmaier, C., Burke, M. J., Clark, K. C., Dahl, C., Dahl, K., Danzmann, K., Davis, M. A., de Vine, G., Dickson, J. A., Dubovitsky, S., Eckardt, A., . . . Zimmermann, M. (2019). In-Orbit Performance of the GRACE Follow-on Laser Ranging Interferometer. *Physical Review Letters*, *123*(3), 031101. https://doi.org/10.1103/physrevlett.123.031101

Allan, D. (1966). Statistics of atomic frequency standards. *Proceedings of the IEEE*, *54*(2), 221–230. https://doi.org/10.1109/proc.1966.4634

Armano, M., Audley, H., Auger, G., Baird, J. T., Bassan, M., Binetruy, P., Born, M., Bortoluzzi, D., Brandt, N., Caleno, M., Carbone, L., Cavalleri, A., Cesarini, A., Ciani, G., Congedo, G., Cruise, A. M., Danzmann, K., de Deus Silva, M., De Rosa, R., . . . Zweifel, P. (2016). Sub-Femto-gFree Fall for Space-Based Gravitational Wave Observatories: LISA Pathfinder Results. *Physical Review Letters*, *116*(23), 231101. https://doi.org/10.1103/physrevlett.116.231101

Balmino, G., Schrama, E., & Sneeuw, N. (1996). Compatibility of first-order circular orbit perturbations theories; consequences for cross-track inclination functions. *Journal of Geodesy*, *70*(9), 554–561. https://doi.org/10.1007/bf00867863

Barnes, J. A., Chi, A. R., Cutler, L. S., Healey, D. J., Leeson, D. B., McGunigal, T. E., Mullen, J. A., Smith, W. L., Sydnor, R. L., Vessot, R. F. C., & Winkler, G. M. R. (1971). Characterization of Frequency Stability. *IEEE Transactions on Instrumentation and Measurement*, *IM–20*(2), 105–120. https://doi.org/10.1109/tim.1971.5570702

Battrick, B., Johannessen, J. A., & Aguirre-Martinez, M. (1999). *ESA SP-1233 (1) - The Four Candidate Earth Explorer Core Missions - Gravity Field and Steady-state Ocean Circulation* (tech. rep.). ESA.

Bender, P. L., Conklin, J. W., & Wiese, D. N. (2025). Short-Period Mass Variations and the Next Generation Gravity Mission. *Journal of Geophysical Research: Solid Earth*, *130*(1). https://doi.org/10.1029/2024jb030290

Bender, P. L., Wiese, D. N., & Nerem, R. S. (2008). A possible dual-GRACE mission with 90 degree and 63 degree inclination orbits. In Missions & Technologies (Eds.), *Proceedings of the Third International Symposium on Formation Flying* (pp. 1–6).

Bingham, R. J., & Hughes, C. W. (2008). Determining North Atlantic meridional transport variability from pressure on the western boundary: A model investigation. *Journal of Geophysical Research: Oceans*, *113*(C9). https://doi.org/10.1029/2007jc004679

Bingham, R. J., & Hughes, C. W. (2009). Signature of the Atlantic meridional overturning circulation in sea level along the east coast of North America. *Geophysical Research Letters*, *36*(2). https://doi.org/10.1029/2008gl036215

Biscani, F., & Izzo, D. (2020). A parallel global multiobjective framework for optimization: pagmo. *Journal of Open Source Software*, *5*(53), 2338. https://doi.org/10.21105/joss.02338

Boulanger, D., Christophe, B., Lebat, V., Liorzou, F., Maquaire, K., Portier, N., & Rodrigues, M. (2025, March). CubeSTAR: a tiny space accelerometer for Earth observation applications. In M. Petrozzi-Ilstad (Ed.), *Small Satellites Systems and Services Symposium (4S 2024)* (p. 87). SPIE. https://doi.org/10.1117/12.3062066

Brest, J., Greiner, S., Boskovic, B., Mernik, M., & Zumer, V. (2006). Self-adapting control parameters in differential evolution: A comparative study on numerical benchmark problems. *IEEE Transactions on Evolutionary Computation*, *10*(6), 646–657. https://doi.org/10.1109/tevc.2006.872133

Broquet, A., & Wieczorek, M. A. (2019). The Gravitational Signature of Martian Volcanoes. *Journal of Geophysical Research: Planets*, *124*(8), 2054–2086. https://doi.org/10.1029/2019je005959

Brouwer, D. (1959). Solution of the problem of artificial satellite theory without drag. *The Astronomical Journal*, *64*, 378. https://doi.org/10.1086/107958

Canuto, E. (2008). Drag-free and attitude control for the GOCE satellite. *Automatica*, *44*(7), 1766–1780. https://doi.org/10.1016/j.automatica.2007.11.023

Cesare, S., Dionisio, S., Saponara, M., Bravo-Berguño, D., Massotti, L., Teixeira da Encarnação, J., & Christophe, B. (2022). Drag and Attitude Control for the Next Generation Gravity Mission. *Remote Sensing*, *14*(12), 2916. https://doi.org/10.3390/rs14122916

Chambers, D. P., & Willis, J. K. (2010). A Global Evaluation of Ocean Bottom Pressure from GRACE, OMCT, and Steric-Corrected Altimetry. *Journal of Atmospheric and Oceanic Technology*, *27*(8), 1395–1402. https://doi.org/10.1175/2010jtecho738.1

Chen, J., Cazenave, A., Dahle, C., Llovel, W., Panet, I., Pfeffer, J., & Moreira, L. (2022). Applications and Challenges of GRACE and GRACE Follow-On Satellite Gravimetry. *Surveys in Geophysics*, *43*(1), 305–345. https://doi.org/10.1007/s10712-021-09685-x

Christophe, B., Boulanger, D., Foulon, B., Huynh, P.-A., Lebat, V., Liorzou, F., & Perrot, E. (2015). A new generation of ultra-sensitive electrostatic accelerometers for GRACE Follow-on and towards the next generation gravity missions. *Acta Astronautica*, *117*, 1–7. https://doi.org/10.1016/j.actaastro.2015.06.021

Christophe, B., Foulon, B., Liorzou, F., Lebat, V., Boulanger, D., Huynh, P.-A., Zahzam, N., Bidel, Y., & Bresson, A. (2018). Status of Development of the Future Accelerometers for Next Generation Gravity Missions. In *International Symposium on Advancing Geodesy in a Changing World* (pp. 85–89). Springer International Publishing. https://doi.org/10.1007/1345_2018_42

Colombo, O. L. (1986). Notes on the mapping of the gravity field using satellite data. In *Mathematical and Numerical Techniques in Physical Geodesy* (pp. 261–315). Springer-Verlag. https://doi.org/10.1007/bfb0010134

Colombo, O. L. (1984). *The global mapping of gravity with two satellites*. Rijkscommissie voor Geodesie.

Dalin, M., Lebat, V., Boulanger, D., Liorzou, F., Christophe, B., Rodrigues, M., & Huynh, P.-A. (2020). Onera accelerometers for future gravity mission [EGU2020-5721. Distributed under CC BY 4.0 (https://creativecommons.org/licenses/by/4.0/).]. *EGU General Assembly 2020, Online, 4–8 May 2020*. https://doi.org/10.5194/egusphere-egu2020-5721

Daras, I., Tsaoussi, L., March, G., Massotti, L., Carnicero Dominguez, B., & Carraz, O. (2023). ESA/NASA Mass change And Geosciences International Constellation (MAGIC) mission concept – science and application prospects. https://doi.org/10.5194/egusphere-egu23-13535

Darbeheshti, N., Lasser, M., Meyer, U., Arnold, D., & Jäggi, A. (2024). AIUB-GRACE gravity field solutions for G3P: processing strategies and instrument parameterization. *Earth System Science Data*, *16*(3), 1589–1599. https://doi.org/10.5194/essd-16-1589-2024

Dávila Álvarez, A., Knudtson, A., Patel, U., Gleason, J., Hollis, H., Sanjuan, J., Doughty, N., McDaniel, G., Lee, J., Leitch, J., Bennett, S., Bevilacqua, R., Mueller, G., Spero, R., Ware, B., Wass, P., Wiese, D., Ziemer, J., & Conklin, J. W. (2022). A simplified gravitational reference sensor for satellite geodesy. *Journal of Geodesy*, *96*(10). https://doi.org/10.1007/s00190-022-01659-0

Dickey, J. O., et al. (1997). *Satellite Gravity and the Geosphere: Contributions to the Study of the Solid Earth and Its Fluid Envelope* [National Research Council]. National Academy Press.

Dionisio, S., Anselmi, A., Bonino, L., Cesare, S., Massotti, L., & Silvestrin, P. (2018). The "Next Generation Gravity Mission": challenges and consolidation of the system concepts and technological innovations. *2018 SpaceOps Conference*. https://doi.org/10.2514/6.2018-2495

Doorn, B., Jasinski, M., Reager, J., Srinivasan, M., Bettadpur, S., Bolten, J., Boening, C., Brown, M., Flechtner, F., Ivins, E., Kumar, S., Landerer, F., Morton, P., Policelli, F., Rodell, M., Tsaoussi, L., & Webb, F. (2016). *Applications Plan for the Gravity Recovery And Climate Experiment (GRACE) Missions: GRACE, GRACE-FO, and Future Missions* (tech. rep.). NASA Earth Science Division, Applied Science Program, GRACE Missions.

Ellmer, M. (2011). Optimization of the orbit parameters of future gravity missions using genetic algorithms. https://doi.org/10.18419/OPUS-3873

Elsaka, B., Raimondo, J.-C., Brieden, P., Reubelt, T., Kusche, J., Flechtner, F., Iran Pour, S., Sneeuw, N., & Müller, J. (2013). Comparing seven candidate mission configurations for temporal gravity field retrieval through full-scale numerical simulation. *Journal of Geodesy*, *88*(1), 31–43. https://doi.org/10.1007/s00190-013-0665-9

Elsayed, S. M., Sarker, R. A., & Essam, D. L. (2011). Differential evolution with multiple strategies for solving cec2011 real-world numerical optimization problems. *2011 IEEE Congress of Evolutionary Computation (CEC)*, 1041–1048. https://doi.org/10.1109/cec.2011.5949732

Famiglietti, J. S., & Rodell, M. (2013). Water in the Balance. *Science*, *340*(6138), 1300–1301. https://doi.org/10.1126/science.1236460

Fullea, J., Rodríguez-González, J., Charco, M., Martinec, Z., Negredo, A., & Villaseñor, A. (2015). Perturbing effects of sub-lithospheric mass anomalies in GOCE gravity gradient and other gravity data modelling: Application to the Atlantic-Mediterranean transition zone. *International Journal of Applied Earth Observation and Geoinformation*, *35*, 54–69. https://doi.org/10.1016/j.jag.2014.02.003

Gaposchkin, E. M., & Lambeck, K. (1971). Earth's gravity field to the sixteenth degree and station coordinates from satellite and terrestrial data. *Journal of Geophysical Research*, *76*(20), 4855–4883. https://doi.org/10.1029/jb076i020p04855

Gleason, D. M. (1985). Partial sums of legendre series via clenshaw summation. *manuscripta geodaetica*, *10*(2), 115–130. https://doi.org/10.1007/bf03655078

Glover, F., & Sörensen, K. (2015). Metaheuristics. *Scholarpedia*, *10*(4), 6532. https://doi.org/10.4249/scholarpedia.6532

Gooding, R. H., & Wagner, C. A. (2008). On the inclination functions and a rapid stable procedure for their evaluation together with derivatives. *Celestial Mechanics and Dynamical Astronomy*, *101*(3). https://doi.org/10.1007/s10569-008-9145-6

Haagmans, R., & van Gelderen, M. (1991). Error variances-covariances of GEM-T1: Their characteristics and implications in geoid computation. *Journal of Geophysical Research: Solid Earth*, *96*(B12), 20011–20022. https://doi.org/10.1029/91jb01971

Haagmans, R., Tsaoussi, L., Masotti, L., March, G., & Daras, I. (2020). *Next Generation Gravity Mission as a Mass-change And Geosciences International Constellation (MAGIC) - A joint ESA/NASA double-pair mission based on NASA's MCDO and ESA's NGGM studies* (tech. rep.). ESA. https://esamultimedia.esa.int/docs/EarthObservation/MAGIC_NGGM_MCDO_MRD_v1_0-signed2.pdf

Hajela, D. P. (1978, September). Improved procedures for the recovery of 5 degrees mean gravity anomalies from ATS-6/GEOS-3 satellite to satellite range-rate observations using least square collocation. https://ui.adsabs.harvard.edu/abs/1978STIN...7922181H

Han, S.-C., Riva, R., Sauber, J., & Okal, E. (2013). Source parameter inversion for recent great earthquakes from a decade-long observation of global gravity fields. *Journal of Geophysical Research: Solid Earth*, *118*(3), 1240–1267. https://doi.org/10.1002/jgrb.50116

Han, S.-C., Shum, C. K., Bevis, M., Ji, C., & Kuo, C.-Y. (2006). Crustal Dilatation Observed by GRACE After the 2004 Sumatra-Andaman Earthquake. *Science*, *313*(5787), 658–662. https://doi.org/10.1126/science.1128661

Heiskanen, W., & Moritz, H. (1967). *Physical Geodesy*. W. H. Freeman.

Hellwig, H. (1975). Atomic frequency standards: A survey. *Proceedings of the IEEE*, *63*(2), 212–229. https://doi.org/10.1109/proc.1975.9732

Hill, G. W. (1878). Researches in the Lunar Theory. *American Journal of Mathematics*, *1*(1), 5. https://doi.org/10.2307/2369430

Holmes, S. A., & Featherstone, W. E. (2002). A unified approach to the Clenshaw summation and the recursive computation of very high degree and order normalised associated Legendre functions. *Journal of Geodesy*, *76*(5), 279–299. https://doi.org/10.1007/s00190-002-0216-2

Houborg, R., Rodell, M., Li, B., Reichle, R., & Zaitchik, B. F. (2012). Drought indicators based on model-assimilated Gravity Recovery and Climate Experiment (GRACE) terrestrial water storage observations. *Water Resources Research*, *48*(7). https://doi.org/10.1029/2011wr011291

Ince, E. S., Barthelmes, F., Reißland, S., Elger, K., Förste, C., Flechtner, F., & Schuh, H. (2019). ICGEM – 15 years of successful collection and distribution of global gravitational models, associated services and future plans [See also the ICGEM Frequently Asked Questions: https://icgem.gfz-potsdam.de/docs/icgem_faq.pdf]. *Earth System Science Data*, *11*, 647–674. https://doi.org/10.5194/essd-11-647-2019

Iran Pour, S., Sneeuw, N., Weigelt, M., & Amiri-Simkooei, A. (2019). Orbit Optimization for Future Satellite Gravity Field Missions: Influence of the Time Variable Gravity Field Models in a Genetic Algorithm Approach. In *IX Hotine-Marussi Symposium on Mathematical Geodesy* (pp. 3–9). Springer International Publishing. https://doi.org/10.1007/1345_2019_79

Ivins, E. R., James, T. S., Wahr, J., Schrama, E. J. O., Landerer, F. W., & Simon, K. M. (2013). Antarctic contribution to sea level rise observed by GRACE with improved GIA correction. *Journal of Geophysical Research: Solid Earth*, *118*(6), 3126–3141. https://doi.org/10.1002/jgrb.50208

Jekeli, C. (1979). *Global accuracy estimates of point and mean undulation differences obtained from gravity disturbances, gravity anomalies and potential coefficients* (tech. rep. No. NASA-CR-158836). NASA.

Jekeli, C. (1981). *Alternative Methods to Smooth the Earth's Gravity Field* (tech. rep. No. Report 327). Department of Geodetic Science and Surveying, The Ohio State University. Columbus, Ohio.

Jiao, B., Liu, Q., Dang, Z., Yue, X., Zhang, Y., Xia, Y., Duan, L., Hu, Q., Yue, C., Wang, P., Guo, M., Duan, Z., Cui, B., Zhang, C., & Shao, X. (2024). A review on DFACS (I): System design and dynamics modeling. *Chinese Journal of Aeronautics*, *37*(5), 92–119. https://doi.org/10.1016/j.cja.2024.01.031

Jungclaus, J. H., Fischer, N., Haak, H., Lohmann, K., Marotzke, J., Matei, D., Mikolajewicz, U., Notz, D., & von Storch, J. S. (2013). Characteristics of the ocean simulations in the Max Planck Institute Ocean Model (MPIOM) the ocean component of the MPI-Earth system model. *Journal of Advances in Modeling Earth Systems*, *5*(2), 422–446. https://doi.org/10.1002/jame.20023

Kaula, W. M. (1959). Statistical and harmonic analysis of gravity. *Journal of Geophysical Research*, *64*(12), 2401–2421. https://doi.org/10.1029/jz064i012p02401

Kaula, W. M. (1963). Determination of the Earth's gravitational field. *Reviews of Geophysics*, *1*(4), 507–551. https://doi.org/10.1029/rg001i004p00507

Kaula, W. M. (1966). *Theory of Satellite Geodesy: Applications of Satellites to Geodesy*. Blaisdell Publishing Company.

Keating, T., Taylor, P., Kahn, W., & Lerch, F. (1986). *Geopotential Research Mission, Science, Engineering, and Program Summary* (tech. rep.). NASA.

Killett, E., Wahr, J., Desai, S., Yuan, D., & Watkins, M. (2011). Arctic Ocean tides from GRACE satellite accelerations. *Journal of Geophysical Research: Oceans*, *116*(C11). https://doi.org/10.1029/2011jc007111

Kim, J. (2000). *Simulation Study of A Low-Low Satellite-to-Satellite Tracking Mission* [Ph.D. dissertation]. University of Texas at Austin.

Kim, J., & Tapley, B. D. (2002). Error Analysis of a Low-Low Satellite-to-Satellite Tracking Mission. *Journal of Guidance, Control, and Dynamics*, *25*(6), 1100–1106. https://doi.org/10.2514/2.4989

Klees, R., Revtova, E. A., Gunter, B. C., Ditmar, P., Oudman, E., Winsemius, H. C., & Savenije, H. H. G. (2008). The design of an optimal filter for monthly GRACE gravity models. *Geophysical Journal International*, *175*(2), 417–432. https://doi.org/10.1111/j.1365-246x.2008.03922.x

Knudsen, P., & Andersen, O. (2002). Correcting GRACE gravity fields for ocean tide effects. *Geophysical Research Letters*, *29*(8). https://doi.org/10.1029/2001gl014005

Koop, R. (1993). *Global gravity field modelling using satellite gravity gradiometry*. Rijkscommissie voor Geodesie.

Kornfeld, R. P., Arnold, B. W., Gross, M. A., Dahya, N. T., Klipstein, W. M., Gath, P. F., & Bettadpur, S. (2019). GRACE-FO: The Gravity Recovery and Climate Experiment Follow-On Mission. *Journal of Spacecraft and Rockets*, *56*(3), 931–951. https://doi.org/10.2514/1.a34326

Kostelecký, J., Klokočník, J., & Kalina, Z. (1986). Computation of normalized inclination function to high degree for satellites in resonances. *manuscripta geodaetica*, *11*(4), 293–304. https://doi.org/10.1007/bf03655101

Kusche, J., Schmidt, R., Petrovic, S., & Rietbroek, R. (2009). Decorrelated GRACE time-variable gravity solutions by GFZ, and their validation using a hydrological model. *Journal of Geodesy*, *83*(10), 903–913. https://doi.org/10.1007/s00190-009-0308-3

Kusche, J. (2007). Approximate decorrelation and non-isotropic smoothing of time-variable GRACE-type gravity field models. *Journal of Geodesy*, *81*(11), 733–749. https://doi.org/10.1007/s00190-007-0143-3

Kvas, A., Behzadpour, S., Ellmer, M., Klinger, B., Strasser, S., Zehentner, N., & Mayer-Gürr, T. (2019). ITSG-Grace2018: Overview and Evaluation of a New GRACE-Only Gravity Field Time Series. *Journal of Geophysical Research: Solid Earth*, *124*(8), 9332–9344. https://doi.org/10.1029/2019jb017415

Lambeck, K., & Coleman, R. (1983). The Earth's shape and gravity field: a report of progress from 1958 to 1982. *Geophysical Journal International*, *74*(1), 25–54. https://doi.org/10.1111/j.1365-246x.1983.tb01869.x

Landerer, F. W., Flechtner, F. M., Save, H., Webb, F. H., Bandikova, T., Bertiger, W. I., Bettadpur, S. V., Byun, S. H., Dahle, C., Dobslaw, H., Fahnestock, E., Harvey, N., Kang, Z., Kruizinga, G. L. H., Loomis, B. D., McCullough, C., Murböck, M., Nagel, P., Paik, M., ... Yuan, D.-N. (2020). Extending the Global Mass Change Data Record: GRACE Follow-On Instrument and Science Data Performance. *Geophysical Research Letters*, *47*(12). https://doi.org/10.1029/2020gl088306

Lara, M. (2003). Repeat Ground Track Orbits of the Earth Tesseral Problem as Bifurcations of the Equatorial Family of Periodic Orbits. *Celestial Mechanics and Dynamical Astronomy*, *86*(2), 143–162. https://doi.org/10.1023/a:1024195900757

Li, H., Reubelt, T., Antoni, M., & Sneeuw, N. (2016). Gravity field error analysis for pendulum formations by a semi-analytical approach. *Journal of Geodesy*, *91*(3), 233–251. https://doi.org/10.1007/s00190-016-0958-x

Lian-Da, W., & Hong-Bo, W. (2012). A Definite Integration Method for Calculating Inclination Function and Its Derivative. *Chinese Astronomy and Astrophysics*, *36*(3), 307–317. https://doi.org/10.1016/j.chinastron.2012.07.007

Lian-da, W., & Ming-jiang, Z. (2022). Direct Calculation Methods of Hansen Coefficients and Their Derivatives. *Chinese Astronomy and Astrophysics*, *46*(1), 137–151. https://doi.org/10.1016/j.chinastron.2022.02.008

Liu, Y., Li, J., Xu, X., Wei, H., Li, Z., & Zhao, Y. (2024). Simulation analysis of recovering time-varying gravity fields based on Starlink-like constellation. *Geophysical Journal International*, *239*(1), 402–418. https://doi.org/10.1093/gji/ggae273

Lorenz, C., Kunstmann, H., Devaraju, B., Tourian, M. J., Sneeuw, N., & Riegger, J. (2014). Large-Scale Runoff from Landmasses: A Global Assessment of the Closure of the Hydrological and Atmospheric Water Balances*. *Journal of Hydrometeorology*, *15*(6), 2111–2139. https://doi.org/10.1175/jhm-d-13-0157.1

Lorenz, E. N. (1956). *Empirical Orthogonal Functions and Statistical Weather Prediction* [Doctoral dissertation, Massachusetts Institute of Technology, Department of Meteorology].

Luthcke, S. B., Sabaka, T., Loomis, B., Arendt, A., McCarthy, J., & Camp, J. (2013). Antarctica, Greenland and Gulf of Alaska land-ice evolution from an iterated GRACE global mascon solution. *Journal of Glaciology*, *59*(216), 613–631. https://doi.org/10.3189/2013jog12j147

Maquaire, K., Ait-Mehdi, A., Boulanger, D., Chhun, R., Christophe, B., Dalin, M., Hervieux, T., Lebat, V., Liorzou, F., Portier, N., Rodrigues, M., & Rodriguez-Beignet, M. (2025). ONERA accelerometers for NGGM and for future gravity missions. https://doi.org/10.5194/egusphere-egu25-11963

March, G., Doornbos, E., & Visser, P. (2019). High-fidelity geometry models for improving the consistency of CHAMP, GRACE, GOCE and Swarm thermospheric density data sets. *Advances in Space Research*, *63*(1), 213–238. https://doi.org/10.1016/j.asr.2018.07.009

Marchetti, P., Blandino, J. J., & Demetriou, M. A. (2008). Electric Propulsion and Controller Design for Drag-Free Spacecraft Operation. *Journal of Spacecraft and Rockets*, *45*(6), 1303–1315. https://doi.org/10.2514/1.36307

Massotti, L., Amata, G. B., Anselmi, A., Cesare, S., Martimort, P., & Silvestrin, P. (2020, September). Next generation gravity mission: status of the design and discussion on alternative drag compensation scenarios. In S. P. Neeck, T. Kimura, & A. Hélière (Eds.), *Sensors, Systems, and Next-Generation Satellites XXIV*. SPIE. https://doi.org/10.1117/12.2573924

Massotti, L., Bulit, A., Daras, I., Carnicero Dominguez, B., Carraz, O., Hall, K., Heliere, A., March, G., Marchese, V., Martimort, P., Palmer, K., Rodrigues, G., Silvestrin, P., & Wallace, N. (2023). Next Generation Gravity Mission design activities within the MAGIC - MAss Change and Geoscience International - Constellation. https://doi.org/10.5194/egusphere-egu23-14482

Massotti, L., Siemes, C., March, G., Haagmans, R., & Silvestrin, P. (2021). Next Generation Gravity Mission Elements of the Mass Change and Geoscience International Constellation: From Orbit Selection to Instrument and Mission Design. *Remote Sensing*, *13*(19), 3935. https://doi.org/10.3390/rs13193935

Mayer-Gürr, T., Behzadpour, S., Ellmer, M., Kvas, A., Klinger, B., & Zehentner, N. (2016). ITSG-Grace2016 - Monthly and Daily Gravity Field Solutions from GRACE. https://doi.org/10.5880/ICGEM.2016.007

Mayer-Gürr, T., Behzadpur, S., Ellmer, M., Kvas, A., Klinger, B., Strasser, S., & Zehentner, N. (2018). ITSG-Grace2018 - Monthly, Daily and Static Gravity Field Solutions from GRACE. https://doi.org/10.5880/ICGEM.2018.003

Nguyen, A. N., & Conklin, J. W. (2015). Three-Axis Drag-Free Control and Drag Force Recovery of a Single-Thruster Small Satellite. *Journal of Spacecraft and Rockets*, *52*(6), 1640–1650. https://doi.org/10.2514/1.a33190

Nicklaus, K., Cesare, S., Massotti, L., Bonino, L., Mottini, S., Pisani, M., & Silvestrin, P. (2020). Laser metrology concept consolidation for NGGM. *CEAS Space Journal*, *12*(3), 313–330. https://doi.org/10.1007/s12567-020-00324-6

Pail, R., Bingham, R., Braitenberg, C., Dobslaw, H., Eicker, A., Güntner, A., Horwath, M., Ivins, E., Longuevergne, L., Panet, I., Wouters, B., & Team, t. (2015, November). *Observing Mass Transport to Understand Global Change and to Benefit Society: Science and User Needs: An international multi-disciplinary initiative for IUGG* (WorkingPaper No. 320). Verlag der Bayerischen Akademie der Wissenschaften in Kommission beim Verlag C.H. Beck. Verlag der Bayerischen Akademie der Wissenschaften in Kommission beim Verlag C.H. Beck.

Pail, R., Gruber, T., Fecher, T., & GOCO Project Team. (2016). The Combined Gravity Model GOCO05c. https://doi.org/10.5880/ICGEM.2016.003

Panet, I., Flury, J., Biancale, R., Gruber, T., Johannessen, J., van den Broeke, M. R., van Dam, T., Gegout, P., Hughes, C. W., Ramillien, G., Sasgen, I., Seoane, L., & Thomas, M. (2012). Earth System Mass Transport Mission (e.motion): A Concept for Future Earth Gravity Field Measurements from Space. *Surveys in Geophysics*, *34*(2), 141–163. https://doi.org/10.1007/s10712-012-9209-8

Pearson, K. (1901). LIII. On lines and planes of closest fit to systems of points in space. *The London, Edinburgh, and Dublin Philosophical Magazine and Journal of Science*, *2*(11), 559–572. https://doi.org/10.1080/14786440109462720

Pfaffenzeller, N., & Pail, R. (2023). Small satellite formations and constellations for observing sub-daily mass changes in the Earth system. *Geophysical Journal International*, *234*(3), 1550–1567. https://doi.org/10.1093/gji/ggad132

Piretzidis, D., & Sideris, M. G. (2019). Stable recurrent calculation of isotropic Gaussian filter coefficients. *Computers & Geosciences*, *133*, 104303. https://doi.org/10.1016/j.cageo.2019.07.007

Press, W. H., Teukolsky, S. A., Vetterling, W. T., & Flannery, B. P. (2007). *Numerical recipes the art of scientific computing: the art of scientific computing*. Cambridge University Press.

Purkhauser, A. F., & Pail, R. (2020). Triple-Pair Constellation Configurations for Temporal Gravity Field Retrieval. *Remote Sensing*, *12*(5), 831. https://doi.org/10.3390/rs12050831

Reager, J. T., & Famiglietti, J. S. (2009). Global terrestrial water storage capacity and flood potential using GRACE. *Geophysical Research Letters*, *36*(23). https://doi.org/10.1029/2009gl040826

Reigber, C., Balmino, G., Schwintzer, P., Biancale, R., Bode, A., Lemoine, J.-M., König, R., Loyer, S., Neumayer, H., Marty, J.-C., Barthelmes, F., Perosanz, F., & Zhu, S. Y. (2002). A high-quality global gravity field model from CHAMP GPS tracking data and accelerometry (EIGEN-1S). *Geophysical Research Letters*, *29*(14). https://doi.org/10.1029/2002gl015064

Rizos, C. (1979). An efficient computer technique for the evaluation of geopotential from spherical harmonic models. *Australian Journal of Geodesy, Photogrammetry and Surveying*, *31*, 161–169.

Rock, B. S., Blandino, J. J., & Demetriou, M. (2006). Propulsion Requirements for Drag-Free Operation of Spacecraft in Low Earth Orbit. *Journal of Spacecraft and Rockets*, *43*(3), 594–606. https://doi.org/10.2514/1.15819

Rummel, R., & Colombo, O. L. (1985). Gravity field determination from satellite gradiometry. *Bulletin Géodésique*, *59*(3), 233–246. https://doi.org/10.1007/bf02520329

Runge, H., Bamler, R., Mittermayer, J., Jochim, F., Massonnet, D., & Thouvenot, E. (2001). The Interferometric Cartwheel for ENVISAT [3rd IAA Symposium on Small Satellites for Earth Observation, April 2–6, 2001, Berlin, Germany]. *3rd International Symposium of the International Academy of Astronautics (IAA)*, 187–190.

Russell, R. P., & Lara, M. (2007). Long-Lifetime Lunar Repeat Ground Track Orbits. *Journal of Guidance, Control, and Dynamics*, *30*(4), 982–993. https://doi.org/10.2514/1.27104

Saynisch, J., Bergmann-Wolf, I., & Thomas, M. (2014). Assimilation of GRACE-derived oceanic mass distributions with a global ocean circulation model. *Journal of Geodesy*, *89*(2), 121–139. https://doi.org/10.1007/s00190-014-0766-0

Schrama, E. J. O. (1989). *The role of orbit errors in processing of satellite altimeter data*. Rijkscommissie voor Geodesie.

Schrama, E. J. O. (1990). *Gravity field error analysis: Applications of GPS receivers and gradiometers on low orbiting platforms* (tech. rep.). NASA.

Schrama, E. J. O. (1991a). Error Propagation and Correlation Analysis of Covariance Matrices [Personal communication].

Schrama, E. J. O. (1991b). Gravity field error analysis: Applications of global positioning system receivers and gradiometers on low orbiting platforms. *Journal of Geophysical Research: Solid Earth*, *96*(B12), 20041–20051. https://doi.org/10.1029/91jb01972

Schrama, E. J. O., & Visser, P. N. A. M. (2006). Accuracy assessment of the monthly GRACE geoids based upon a simulation. *Journal of Geodesy*, *81*(1), 67–80. https://doi.org/10.1007/s00190-006-0085-1

Schrama, E. J. O., Wouters, B., & Lavallée, D. A. (2007). Signal and noise in Gravity Recovery and Climate Experiment (GRACE) observed surface mass variations. *Journal of Geophysical Research: Solid Earth*, *112*(B8). https://doi.org/10.1029/2006jb004882

Schrama, E. J. O., Wouters, B., & Rietbroek, R. (2014). A mascon approach to assess ice sheet and glacier mass balances and their uncertainties from GRACE data. *Journal of Geophysical Research: Solid Earth*, *119*(7), 6048–6066. https://doi.org/10.1002/2013jb010923

Seneviratne, S. I., Lüthi, D., Litschi, M., & Schär, C. (2006). Land–atmosphere coupling and climate change in Europe. *Nature*, *443*(7108), 205–209. https://doi.org/10.1038/nature05095

Sharifi, M., Sneeuw, N., & Keller, W. (2007). Gravity recovery capability of four generic satellite formations. *Proceedings of the Symposium "Gravity Field of the Earth"*, 211–216.

Sheffield, J., Ferguson, C. R., Troy, T. J., Wood, E. F., & McCabe, M. F. (2009). Closing the terrestrial water budget from satellite remote sensing. *Geophysical Research Letters*, *36*(7). https://doi.org/10.1029/2009gl037338

Shihora, L., Balidakis, K., Dill, R., Dahle, C., Ghobadi-Far, K., Bonin, J., & Dobslaw, H. (2022). Non-Tidal Background Modeling for Satellite Gravimetry Based on Operational ECWMF and ERA5 Reanalysis Data: AOD1B RL07. *Journal of Geophysical Research: Solid Earth*, *127*(8). https://doi.org/10.1029/2022jb024360

Smirnova, M., Mingo, A., Schein, J., Smirnov, P., Bosch, E., & Massotti, L. (2019). Test Campaign on the novel Variable Isp Radio Frequency Mini Ion Engine [IEPC-2019-A-574]. *36th International Electric Propulsion Conference (IEPC)*.

Smith, D. E., Lerch, F. J., Colombo, O. L., & Everitt, C. W. F. (1989). Gravity field information from Gravity Probe-B [NASA Technical Reports Server Document ID: 19900011238]. *Progress in the Determination of the Earth's Gravity Field*.

Sneeuw, N., Sharifi, M., & Keller, W. (2008). Gravity Recovery from Formation Flight Missions. In P. Xu, J. Liu, & A. Dermanis (Eds.), *VI Hotine-Marussi Symposium on Theoretical and Computational Geodesy* (pp. 29–34). Springer Berlin Heidelberg.

Sneeuw, N. (1994). Global spherical harmonic analysis by least-squares and numerical quadrature methods in historical perspective. *Geophysical Journal International*, *118*(3), 707–716. https://doi.org/10.1111/j.1365-246x.1994.tb03995.x

Sneeuw, N., Flury, J., & Rummel, R. (2004). Science Requirements on Future Missions and Simulated Mission Scenarios. *Earth, Moon, and Planets*, *94*(1–2), 113–142. https://doi.org/10.1007/s11038-004-7605-x

Sneeuw, N., & Schaub, H. (2005). Satellite clusters for future gravity field missions. In *Gravity, Geoid and Space Missions* (pp. 12–17). Springer Berlin Heidelberg. https://doi.org/10.1007/3-540-26932-0_3

Sneeuw, N. (2000). *A Semi-Analytical Approach to Gravity Field Analysis from Satellite Observations* [Doctoral dissertation, Institut für Astronomische und Physikalische Geodäsie, TU München].

Song, Y. T., & Zlotnicki, V. (2008). Subpolar ocean bottom pressure oscillation and its links to the tropical ENSO. *International Journal of Remote Sensing*, *29*(21), 6091–6107. https://doi.org/10.1080/01431160802175538

Spiridonova, S., Kirschner, M., & Hugentobler, U. Precise mean orbital elements determination for LEO monitoring and maintenance. In: In *International Symposium on Space Flight Dynamics*. 2014.

Stammer, D., Ray, R. D., Andersen, O. B., Arbic, B. K., Bosch, W., Carrère, L., Cheng, Y., Chinn, D. S., Dushaw, B. D., Egbert, G. D., Erofeeva, S. Y., Fok, H. S., Green, J. A. M., Griffiths, S., King, M. A., Lapin, V., Lemoine, F. G., Luthcke, S. B., Lyard, F., . . . Yi, Y. (2014). Accuracy assessment of global barotropic ocean tide models. *Reviews of Geophysics*, *52*(3), 243–282. https://doi.org/10.1002/2014rg000450

Sulzbach, R., Balidakis, K., Dobslaw, H., & Thomas, M. (2022). TiME22: Periodic Disturbances of the Terrestrial Gravity Potential Induced by Oceanic and Atmospheric Tides. https://doi.org/10.5880/NEROGRAV.2022.006

Sun, Y., Riva, R., & Ditmar, P. (2016). Optimizing estimates of annual variations and trends in geocenter motion and J2 from a combination of GRACE data and geophysical models. *Journal of Geophysical Research: Solid Earth*, *121*(11), 8352–8370. https://doi.org/10.1002/2016jb013073

Swenson, S., Chambers, D., & Wahr, J. (2008). Estimating geocenter variations from a combination of GRACE and ocean model output. *Journal of Geophysical Research: Solid Earth*, *113*(B8). https://doi.org/10.1029/2007jb005338

Tamisiea, M. E., Mitrovica, J. X., & Davis, J. L. (2007). GRACE Gravity Data Constrain Ancient Ice Geometries and Continental Dynamics over Laurentia. *Science*, *316*(5826), 881–883. https://doi.org/10.1126/science.1137157

Tapley, B. D., Bettadpur, S., Watkins, M., & Reigber, C. (2004). The gravity recovery and climate experiment: Mission overview and early results. *Geophysical Research Letters*, *31*(9). https://doi.org/10.1029/2004gl019920

Tapley, B. D., Watkins, M. M., Flechtner, F., Reigber, C., Bettadpur, S., Rodell, M., Sasgen, I., Famiglietti, J. S., Landerer, F. W., Chambers, D. P., Reager, J. T., Gardner, A. S., Save, H., Ivins, E. R., Swenson, S. C., Boening, C., Dahle, C., Wiese, D. N., Dobslaw, H., . . .

Velicogna, I. (2019). Contributions of GRACE to understanding climate change. *Nature Climate Change*, *9*(5), 358–369. https://doi.org/10.1038/s41558-019-0456-2

Teixeira da Encarnação, J., Save, H., Tapley, B., & Rim, H.-J. (2020). Accelerometer Parameterization and the Quality of Gravity Recovery and Climate Experiment Solutions. *Journal of Spacecraft and Rockets*, *57*(4), 740–752. https://doi.org/10.2514/1.a34639

Touboul, P., Willemenot, E., Foulon, B., & Josselin, V. (1999). Accelerometers for CHAMP, GRACE and GOCE space missions: synergy and evolution. *Bollettino di Geofisica Teorica ed Applicata*, *40*(3-4), 321–327.

Tregoning, P., Lambeck, K., & Ramillien, G. (2008). GRACE estimates of sea surface height anomalies in the Gulf of Carpentaria, Australia. *Earth and Planetary Science Letters*, *271*(1–4), 241–244. https://doi.org/10.1016/j.epsl.2008.04.018

Verhulst, F. (1996). *Nonlinear Differential Equations and Dynamical Systems*. Springer Berlin Heidelberg. https://doi.org/10.1007/978-3-642-61453-8

Vishwakarma, B. D. (2020). Monitoring Droughts From GRACE. *Frontiers in Environmental Science*, *8*. https://doi.org/10.3389/fenvs.2020.584690

Visser, P. N. A. M., Schrama, E. J. O., Sneeuw, N., & Weigelt, M. (2012). Dependency of Resolvable Gravitational Spatial Resolution on Space-Borne Observation Techniques. In S. Kenyon, M. C. Pacino, & U. Marti (Eds.), *Geodesy for Planet Earth* (pp. 373–379). Springer Berlin Heidelberg.

Visser, P. N. A. M., Sneeuw, N., Reubelt, T., Losch, M., & van Dam, T. (2010). Space-borne gravimetric satellite constellations and ocean tides: aliasing effects. *Geophysical Journal International*. https://doi.org/10.1111/j.1365-246x.2010.04557.x

Visser, P. (2005). Low-low satellite-to-satellite tracking: a comparison between analytical linear orbit perturbation theory and numerical integration. *Journal of Geodesy*, *79*(1–3), 160–166. https://doi.org/10.1007/s00190-005-0455-0

Vonbun, F. O., Kahn, W. D., Wells, W. T., & Conrad, T. D. (1980). Determination of 5ºx5º gravity anomalies using satellite-to-satellite tracking between ATS-6 and Apollo. *Geophysical Journal International*, *61*(3), 645–657. https://doi.org/10.1111/j.1365-246x.1980.tb04836.x

Wagner, C. A. (1983). Direct determination of gravitational harmonics from low-low GRAVSAT data. *Journal of Geophysical Research: Solid Earth*, *88*(B12), 10309–10321. https://doi.org/10.1029/jb088ib12p10309

Wahr, J., Molenaar, M., & Bryan, F. (1998). Time variability of the Earth's gravity field: Hydrological and oceanic effects and their possible detection using GRACE. *Journal of Geophysical Research: Solid Earth*, *103*(B12), 30205–30229. https://doi.org/10.1029/98jb02844

Wahr, J., Swenson, S., & Velicogna, I. (2006). Accuracy of GRACE mass estimates. *Geophysical Research Letters*, *33*(6). https://doi.org/10.1029/2005gl025305

WCRP Global Sea Level Budget Group. (2018). Global sea-level budget 1993–present. *Earth System Science Data*, *10*, 1551–1590. https://doi.org/10.5194/essd-10-1551-2018

Wei, Z., Hou-Tse, H., Min, Z., & Mei-Juan, Y. (2015). A Study on the Improvement in Spatial Resolution of the Earth's Gravitational Field by the Next-Generation ACR-Cartwheel-A/B Twin-Satellite Formation. *Chinese Journal of Geophysics*, *58*(2), 135–148. https://doi.org/10.1002/cjg2.20161

Whipple, F. L., & Lundquist, C. A. (1967). A discussion on orbital analysis - Tracking by the Smithsonian Astrophysical Observatory. *Philosophical Transactions of the Royal Society of London. Series A, Mathematical and Physical Sciences*, *262*(1124), 14–25. https://doi.org/10.1098/rsta.1967.0025

Wiese, D. N., Folkner, W. M., & Nerem, R. S. (2008). Alternative mission architectures for a gravity recovery satellite mission. *Journal of Geodesy*, *83*(6), 569–581. https://doi.org/10.1007/s00190-008-0274-1

Wiese, D. N., Nerem, R. S., & Lemoine, F. G. (2011). Design considerations for a dedicated gravity recovery satellite mission consisting of two pairs of satellites. *Journal of Geodesy*, *86*(2), 81–98. https://doi.org/10.1007/s00190-011-0493-8

Wiese, D. N., Visser, P., & Nerem, R. S. (2011). Estimating low resolution gravity fields at short time intervals to reduce temporal aliasing errors. *Advances in Space Research*, *48*(6), 1094–1107. https://doi.org/10.1016/j.asr.2011.05.027

Wnuk, E. (1997). Highly eccentric satellite orbits. *Advances in Space Research*, *19*(11), 1735–1740. https://doi.org/10.1016/s0273-1177(97)00336-0

Wolff, M. (1969). Direct measurements of the Earth's gravitational potential using a satellite pair. *Journal of Geophysical Research*, *74*(22), 5295–5300. https://doi.org/10.1029/jb074i022p05295

Wouters, B., & Chambers, D. (2010). Analysis of seasonal ocean bottom pressure variability in the Gulf of Thailand from GRACE. *Global and Planetary Change*, *74*(2), 76–81. https://doi.org/10.1016/j.gloplacha.2010.08.002

Wouters, B., & Schrama, E. J. O. (2007). Improved accuracy of GRACE gravity solutions through empirical orthogonal function filtering of spherical harmonics. *Geophysical Research Letters*, *34*(23). https://doi.org/10.1029/2007gl032098

Zahzam, N., Christophe, B., Lebat, V., Hardy, E., Huynh, P.-A., Marquet, N., Blanchard, C., Bidel, Y., Bresson, A., Abrykosov, P., Gruber, T., Pail, R., Daras, I., & Carraz, O. (2022). Hybrid electrostatic-atomic accelerometer for future space gravity missions. https://doi.org/10.48550/ARXIV.2206.00634